Spring 5-15-2016

Seismic Studies of the Tonga Subduction Zone and the Lau Back-arc Basin

Songqiao Wei
Washington University in St. Louis

WASHINGON UNIVERSITY IN ST. LOUIS

Department of Earth and Planetary Sciences

Dissertation Examination Committee:
Douglas A. Wiens, Chair
Philip Skemer
V. Slava Solomatov
Linda M. Warren
Michael E. Wysession

Seismic Studies of the Tonga Subduction Zone and the Lau Back-arc Basin

by

Songqiao Wei

A dissertation presented to the
Graduate School of Arts and Sciences
of Washington University in
partial fulfillment of the
requirements for the degree
of Doctor of Philosophy

May 2016
St. Louis, Missouri

Table of Contents

List of Figures

List of Tables

Acknowledgements

I would like to thank all of those who have supported and helped me during my PhD studies. My advisor Doug Wiens has provided me with great opportunities to participate in exciting scientific projects. His serious attitude, honesty, and enthusiasm for science have significantly influenced my research. Furthermore, Doug is a great mentor who has helped me to embrace an enjoyable life in St. Louis, a city I had not heard of six years ago. I am grateful to all faculty members on my dissertation committee, Slava Solomatov, Michael Wysession, Phil Skemer, and Linda Warren who gave me advice on various perspectives of earth science. In particular, Phil Skemer has introduced rock physics to me, an interesting field that I was not aware of.

I want to thank Patrick Shore, a great mentor and also an excellent friend, who has helped me on almost everything, from research to life troubles. Chatting with him becomes a very important and helpful part of my student life. I am grateful to all of the members of the Washington University seismology group and the Department of Earth and Planetary Sciences. I appreciate the friendship and help from Martin Pratt, Andrew Lloyd, Garrett Euler, David Heeszel, Xinlei Sun, Chen Cai, Aubreya Adams, Heather Fisher, Weisen Shen, Abby Fraeman, Brandon Mahan, Kelsi Singer, Zhen Li, and many others.

I could not have completed this dissertation without the support of many collaborators out of Washington University. I want to thank all of the principle investigators of the Ridge2000 Lau Spreading Center Imaging project, including Spahr Webb, Donna Blackman, Robert Dunn, and James Conder. In this NSF-funded project, the crew and science teams of the R/Vs *Roger Revelle* and *Kilo Moana* collected a tremendous seismic dataset that enabled me to investigate the Tonga-Lau region. IRIS PASSCAL and OBSIP provided land-based seismic instrumentation

and OBSs, respectively. Yang Zha, Terry Plank, Peter van Keken, Don Forsyth, Yingjie Yang, Nick Harmon, Kate Rychert, Ge Jin, and Brad Hacker all helped me on one or multiple problems. I particularly want to thank my former advisor Y. John Chen at Peking University, for encouraging me and introducing me to Washington University.

McDonnell International Scholars Academy, initiated by Mr John McDonnell, has financially supported me for five years. I would like to thank Director James Wertsch and his wife Mary for providing warm advice and hosting dinners for Thanksgiving and Christmas every year. Dean Barbara Schaal, the McDonnell Ambassador to Peking University, also has given me important advice on developing a long-term career.

Finally and most importantly, I would like to thank my parents and grandparents who have been continuously supportive of my education and career throughout my whole life. I feel very lucky to meet Xiaofei Yue during the last year of my PhD study. I owe her more than thanks for everything she has done to support me to finish my dissertation.

ABSTRACT OF THE DISSERTATION

Seismic Studies of the Tonga Subduction Zone and the Lau Back-arc Basin

by

Songqiao Wei

Doctor of Philosophy in Earth and Planetary Sciences

Washington University in St. Louis, 2016

Professor Douglas A. Wiens, Chair

This dissertation utilizes multiple techniques of seismic tomography and earthquake location to investigate the upper mantle structure and intermediate-depth seismicity of the Tonga subduction zone, the Lau back-arc basin, and adjacent regions. Data for these studies consist of broadband records from 49 ocean bottom seismographs and 17 island-based seismic stations deployed for one year in 2009-2010, as well as more limited earlier datasets. I conducted tomographic studies of Rayleigh wave velocity and body wave attenuation to examine the thermal variations and the distribution of partial melt in the mantle wedge. The shear-wave velocity structure is first determined using only teleseismic data with the two-plane-wave method, and then jointly inverted from the phase velocities of teleseismic and ambient-noise Rayleigh waves obtained from noise cross-correlation. Additionally, I determine the 3-D *P* and *S* wave attenuation structure from t^* measurements using local and regional earthquakes. Tomographic results show extremely low velocity and high attenuation within the upper 80-km of the mantle beneath the Lau back-arc basin, suggesting perhaps the lowest shear-wave velocity (V_{SV} = 3.6 km/s) and highest seismic attenuation (Q_P < 35 and Q_S < 25) known in the mantle. These

anomalies require not only abnormally high temperature but also the existence of partial melt. The inferred melting regions align with the spreading centers at shallow depths of 20-70 km, but shift westwards away from the slab, indicating a passive decompression melting process governed by the mantle wedge flow rising from the west. Assuming that velocity anomalies reflect variations in mantle porosity filled with melt, the mantle porosity is reduced in areas of high mantle water content, implying that the melt segregation and extraction are significantly enhanced by the water released from the subducting slab. The low velocities and high attenuation beneath the northeastern Fiji Plateau and northern Lau Ridge suggest the missing lithospheric root in this region, where the active Taveuni Volcano exists. This, along with the low-velocity anomalies beneath the northwestern Lau Basin, are consistent with a second origin from the deep mantle in addition to the Samoan mantle plume.

In order to investigate water-related slab processes, I precisely locate intermediate-depth earthquakes and associate them with the Global Centroid Moment Tensor solutions. These events form a double seismic zone with a separation of about 30 km in the northern part of the Tonga slab, with a downdip compressional upper plane and a downdip tensional lower plane. The lower termination of the double seismic zone correlates with the convergence rate, extending to 300 km in places, and is consistently deeper than in Japan and other slabs worldwide. Similar trends have been found for a tripe of seismicity at depths of 200-300 km. These observations indicate that the depth of intermediate-depth seismicity is primarily influenced by temperature, implying the importance of the thermally controlled processes, such as serpentine dehydration and fluid-related embrittlement. However, the disappearance of the double seismic zone towards to the south coincides with the change in slab curvature, suggesting that the stress states rather than dehydration reactions control the activity of the lower plane.

Chapter 1

Introduction

The Tonga subduction zone and the adjacent Lau back-arc basin are exemplary locations for understanding fundamental processes of plate tectonics, such as subduction, back-arc spreading, and their interactions. While the Pacific Plate has subducted westward beneath the Australian Plate along the Tonga Trench for considerable time, back-arc extension began at about 6 Ma, and then turned to seafloor spreading at about 4 Ma [*Taylor et al.*, 1996]. This process split the ancient Lau-Colville volcanic arc into the Lau Ridge and Tonga Ridge, and formed the Lau Basin in between. Currently the maximum total back-arc spreading rate of 160 mm/yr occurs in the northern part of the Lau basin, and the convergence rate between the Tonga plate and the Pacific plate also reaches a maximum of 240 mm/yr in the north [*Bevis et al.*, 1995]. Both rates decrease monotonously towards to the south, resulting in a larger distance from the spreading centers to the trench in the north than in the south. These variations in subduction rate and distance between the slab, arc, and backarc spreading center provide ideal opportunities to study various effects on slab and mantle wedge processes.

Previous studies of geology, petrology, geochemistry, and geomorphology revealed systematic along-strike variations of the Lau back-arc spreading center, and attributed them to the varying interactions between the subduction and the back-arc [e.g. *Zellmer and Taylor*, 2001; *Martinez and Taylor*, 2002; *Kelley et al.*, 2006; *Martinez et al.*, 2006; *Bézos et al.*, 2009; *Escrig*

et al., 2009]. However, most of previous seismic studies in the region were mainly confined to a linear seismic array nearly perpendicular to the Tonga Trench [e.g. *Zhao et al.*, 1997; *Roth et al.*, 1999; *Smith et al.*, 2001; *Conder and Wiens*, 2006; *Wiens et al.*, 2008], and large scale tomographic studies failed to provide details due to low resolution [e.g. *van der Hilst*, 1995; *Deal et al.*, 1999]. Thanks to the 2-D seismic array of the Ridge2000 Lau Spreading Center Imaging project, which consisted of 49 ocean bottom seismographs and 17 island-based stations in Tonga, Fiji, and the Lau Basin, the high quality data greatly improve our capability to further investigate the along-strike variations.

In Chapter 2 we use the two-plane-wave method of Rayleigh wave tomography [*Forsyth and Li*, 2005; *Yang and Forsyth*, 2006] to analyze these data as well as data collected from 1990s deployments, mainly focusing on the N-S variations of partial melt beneath the back-arc spreading centers. In Chapter 3 we combine the ambient-noise tomography with the two-plane-wave tomography for *SV*- velocity inversions with a Bayesian Monte-Carlo algorithm [*Shen et al.*, 2012]. These strategies significantly improve the tomographic resolution at shallow depths, so that we are able to construct a comprehensive model of the uppermost mantle. This model, along with previous petrological studies, helps us better understand the thermal variations and melt distribution in this region.

In Chapter 4 we analyze the waveforms of local earthquakes in order to investigate seismic attenuation in the mantle wedge. The *P*- and *S*-wave amplitude spectra from local events are first inverted for path-average attenuation operator (t*), and then for the 3-D tomographic models of Q_P, Q_S, and Q_P/Q_S. The results of attenuation generally correlate well with the *SV*-velocity structures in Chapters 2 and 3, though some discrepancies may reveal more complexities.

In Chapter 5 we relocate the intermediate-depth earthquakes in Chapter 4 using the hypocentroidal decomposition algorithm [*Jordan and Sverdrup*, 1981; *Bergman and Solomon*, 1990], and associate half of these events with the Global Centroid Moment Tensor solutions [*Dziewoński et al.*, 1981; *Ekström et al.*, 2012]. Based on the slab geometry defined by the relocated hypocenters, we build 2-D thermal structures of the Tonga slab along 6 cross-sections and calculate the pressure-temperature condition of each event. The comparisons between the Tonga seismicity and the major dehydration reactions provide new evidence for the mechanisms of intermediate-depth earthquakes and for the depth distribution of water release in the mantle wedge.

References

Bergman, E. A., and S. C. Solomon (1990), Earthquake swarms on the Mid-Atlantic Ridge: Products of magmatism or extensional tectonics?, *J. Geophys. Res.*, *95*(B4), 4943-4965, doi: 10.1029/JB095iB04p04943.

Bevis, M., F. W. Taylor, B. E. Schutz, J. Recy, B. L. Isacks, S. Helu, R. Singh, E. Kendrick, J. Stowell, B. Taylor, and S. Calmantli (1995), Geodetic observations of very rapid convergence and back-arc extension at the Tonga arc, *Nature*, *374*(6519), 249-251.

Bézos, A., S. Escrig, C. H. Langmuir, P. J. Michael, and P. D. Asimow (2009), Origins of chemical diversity of back-arc basin basalts: A segment-scale study of the Eastern Lau Spreading Center, *J. Geophys. Res.*, *114*(B6), doi: 10.1029/2008jb005924.

Conder, J. A., and D. A. Wiens (2006), Seismic structure beneath the Tonga arc and Lau back-arc basin determined from joint Vp, Vp/Vs tomography, *Geochem. Geophys. Geosyst.*, *7*(3), Q03018, doi: 10.1029/2005gc001113.

Deal, M. M., G. Nolet, and R. D. van der Hilst (1999), Slab temperature and thickness from seismic tomography: 1. Method and application to Tonga, *J. Geophys. Res.*, *104*(B12), 28789-28802, doi: 10.1029/1999JB900255.

Dziewoński, A. M., T. A. Chou, and J. H. Woodhouse (1981), Determination of earthquake source parameters from waveform data for studies of global and regional seismicity, *J. Geophys. Res.*, *86*(B4), 2825-2852, doi: 10.1029/JB086iB04p02825.

Ekström, G., M. Nettles, and A. M. Dziewoński (2012), The global CMT project 2004–2010: Centroid-moment tensors for 13,017 earthquakes, *Phys. Earth Planet. In.*, *200–201*, 1-9, doi: 10.1016/j.pepi.2012.04.002.

Escrig, S., A. Bézos, S. L. Goldstein, C. H. Langmuir, and P. J. Michael (2009), Mantle source variations beneath the Eastern Lau Spreading Center and the nature of subduction components in the Lau basin–Tonga arc system, *Geochem. Geophys. Geosyst.*, *10*(4), doi: 10.1029/2008gc002281.

Forsyth, D. W., and A. Li (2005), Array Analysis of Two-Dimensional Variations in Surface Wave Phase Velocity and Azimuthal Anisotropy in the Presence of Multipathing Interference, in *Seismic Earth: Array Analysis of Broadband Seismograms*, edited by A. Levander and G. Nolet, pp. 81-97, American Geophysical Union, Washington, D. C.

Jordan, T. H., and K. A. Sverdrup (1981), Teleseismic location techniques and their application to earthquake clusters in the South-Central Pacific, *Bull. Seism. Soc. Amer.*, *71*(4), 1105-1130.

Kelley, K. A., T. Plank, T. L. Grove, E. M. Stolper, S. Newman, and E. Hauri (2006), Mantle melting as a function of water content beneath back-arc basins, *J. Geophys. Res.*, *111*(B9), B09208, doi: 10.1029/2005jb003732.

Martinez, F., and B. Taylor (2002), Mantle wedge control on back-arc crustal accretion, *Nature*, *416*(6879), 417-420, doi: 10.1038/416417a.

Martinez, F., B. Taylor, E. T. Baker, J. A. Resing, and S. L. Walker (2006), Opposing trends in crustal thickness and spreading rate along the back-arc Eastern Lau Spreading Center: Implications for controls on ridge morphology, faulting, and hydrothermal activity, *Earth Planet. Sci. Lett.*, *245*(3-4), 655-672, doi: 10.1016/j.epsl.2006.03.049.

Roth, E. G., D. A. Wiens, L. M. Dorman, J. Hildebrand, and S. C. Webb (1999), Seismic attenuation tomography of the Tonga-Fiji region using phase pair methods, *J. Geophys. Res.*, *104*(B3), 4795-4809, doi: 10.1029/1998jb900052.

Shen, W., M. H. Ritzwoller, V. Schulte-Pelkum, and F.-C. Lin (2012), Joint inversion of surface wave dispersion and receiver functions: a Bayesian Monte-Carlo approach, *Geophys. J. Int.*, doi: 10.1093/gji/ggs050.

Smith, G. P., D. A. Wiens, K. M. Fischer, L. M. Dorman, S. C. Webb, and J. A. Hildebrand (2001), A Complex Pattern of Mantle Flow in the Lau Backarc, *Science*, *292*(5517), 713-716, doi: 10.1126/science.1058763.

Taylor, B., K. Zellmer, F. Martinez, and A. Goodliffe (1996), Sea-floor spreading in the Lau back-arc basin, *Earth Planet. Sci. Lett.*, *144*(1-2), 35-40, doi: 10.1016/0012-821x(96)00148-3.

van der Hilst, R. (1995), Complex morphology of subducted lithosphere in the mantle beneath the Tonga trench, *Nature*, *374*(6518), 154-157.

Wiens, D. A., J. A. Conder, and U. H. Faul (2008), The Seismic Structure and Dynamics of the Mantle Wedge, *Annu. Rev. Earth Planet. Sci.*, *36*(1), 421-455, doi: 10.1146/annurev.earth.33.092203.122633.

Yang, Y., and D. W. Forsyth (2006), Regional tomographic inversion of the amplitude and phase of Rayleigh waves with 2-D sensitivity kernels, *Geophys. J. Int.*, *166*(3), 1148-1160, doi: 10.1111/j.1365-246X.2006.02972.x.

Zellmer, K. E., and B. Taylor (2001), A three-plate kinematic model for Lau Basin opening, *Geochem. Geophys. Geosyst.*, *2*(5), doi: 10.1029/2000gc000106.

Zhao, D., Y. Xu, D. A. Wiens, L. Dorman, J. Hildebrand, and S. Webb (1997), Depth Extent of the Lau Back-Arc Spreading Center and Its Relation to Subduction Processes, *Science*, *278*(5336), 254-257, doi: 10.1126/science.278.5336.254.

Chapter 2

Seismic Evidence of Effects of Water on Melt Transport in the Lau Back-arc Mantle

Wei, S. S., D. A. Wiens, Y. Zha, T. Plank, S. C. Webb, D. K. Blackman, R. A. Dunn, and J. A. Conder (2015), Seismic evidence of effects of water on melt transport in the Lau back-arc mantle, *Nature*, *518*(7539), 395-398, doi: 10.1038/nature14113.

Abstract

Processes of melt generation and transport beneath back-arc spreading centers are controlled by two end-member mechanisms: decompression melting similar to that at mid-ocean ridges (MORs) and hydration (flux) melting resembling that beneath arcs [e.g. *Kelley et al.*, 2006]. The Lau Basin, with an abundance of spreading ridges at varying distances from the subduction zone, provides an opportunity to distinguish the effects of these two different melting processes on magma production and crust formation. Here we present constraints on the three-dimensional distribution of partial melt inferred from seismic velocities obtained from Rayleigh wave tomography using land and ocean bottom seismographs. Slow seismic velocities beneath the Central Lau Spreading Center (CLSC) and northern Eastern Lau Spreading Center (ELSC)

extend deeper and westward into the back-arc, suggesting that these spreading centers are fed by melting along upwelling zones from the west, helping to explain geochemical differences with the Valu Fa Ridge (VFR) to the south [*Escrig et al.*, 2009], which has no distinct deep slow seismic velocity anomalies. A slow shear velocity region, interpreted as resulting from high melt content, is imaged in the mantle wedge beneath the CLSC and northeastern Lau Basin (NELB), even where no active spreading center currently exists. This low seismic velocity anomaly becomes weaker with distance south along the ELSC and VFR, in contrast to the inferred increase of magmatic productivity [e.g. *Kelley et al.*, 2006]. We propose that the anomaly variations result from changes in the efficiency of melt extraction, with reduced presence of melt in the south correlating with increased fractional melting and higher water content in the magma. Water released from the slab may greatly reduce the melt viscosity [e.g. *Giordano et al.*, 2008], enhance grain wetting and/or increase grain size [*Karato*, 1989], thereby facilitating melt transport.

2.1. Introduction

Sea floor spreading in the Lau back-arc system began about 4 Ma in the north [*Taylor et al.*, 1996], propagated southward and split the ancient arc into the Lau Ridge and Tonga Ridge. This process formed the *V*-shape Lau Basin, with its larger distance between the spreading center and active Tofua volcanic arc in the north as compared to the south (Fig. 2.1a). This variation of distance from the arc correlates with systematic changes in the geological features of the spreading centers, with mid-ocean ridge basalt (MORB)-like geochemical signatures in the north, and arc-like signatures and much higher inferred water content in the south [e.g. *Pearce et al.*, 1994; *Martinez and Taylor*, 2002; *Kelley et al.*, 2006]. However, two questions remain unresolved: (1) Why is there an abrupt change in the geochemical signatures of subduction [*Escrig et al.*, 2009] and the structure of young ocean crust [*Dunn and Martinez*, 2011; *Arai and Dunn*, 2014] at about 20˚35'S along the ELSC, though the distance from the ridge to the arc changes gradually? (2) Although the ELSC has an intermediate distance from the arc as compared to the CLSC and VFR, why do its axial crustal properties imply the lowest magmatic activity [*Martinez and Taylor*, 2002]? These questions suggest complexities beyond the subduction-controlled melting process [*Martinez and Taylor*, 2002]. The previous studies rely on petrological and geochemical measurements of erupted basalts [e.g. *Pearce et al.*, 1994; *Kelley et al.*, 2006], seafloor morphology [e.g. *Taylor et al.*, 1996], or the structure of the crust [e.g. *Dunn and Martinez*, 2011; *Arai and Dunn*, 2014] to infer characteristics of the melt production region in the mantle. In this study, we present new high resolution three-dimensional seismic tomography results of the mantle, placing constraints on mantle melting variations in a region characterized by large gradients in mantle water content.

2.2. Results

We used the two-plane-wave method of Rayleigh wave tomography [*Forsyth and Li*, 2005; *Yang and Forsyth*, 2006] and data from two networks of land and ocean bottom seismographs (OBSs) (Fig. 2.1b and 2.5) to image phase velocity at periods ranging 19 - 88 s, and then determined the 3-D shear wave velocity of the uppermost mantle. The derived azimuthally averaged *SV* velocity structure shows a wide low-velocity zone (LVZ) with a *V*-shape in the shallow part of asthenosphere (Fig. 2.1b-c and Fig. 2.4), dipping to the west away from the arc (Fig. 2.2). At shallow depth, e.g. 30 km, the LVZ occurs along the spreading centers and connects the CLSC to the Fonualei Rift and Spreading Center (FRSC) and Mangatolu Triple Junction (MTJ) to the north (Fig. 2.1c). At depths of 50 km, the anomaly becomes stronger beneath the NELB, but weaker beneath the southern ELSC and VFR (Fig. 2.1d). The Lau Ridge and Fiji Plateau are characterized by a high-velocity anomaly in the uppermost mantle, implying that these relict island arcs are underlain by cold lithosphere to a depth of about 70 km. The high velocity anomaly beneath the Tonga Ridge delineates the subducting Pacific slab [*Zhao et al.*, 1997] (Fig. 2.2).

The lowest mantle velocities are found at a depth of about 50 km along a band extending from the MTJ southward to the northern tip of the ELSC, with a minimum *SV* velocity of 3.5 ± 0.15 km/s (Fig. 2.1d), significantly lower than other well-studied upper mantle LVZs [e.g. *Nishimura and Forsyth*, 1989; *Harmon et al.*, 2009] (Section 2.4 and Fig. 2.10). The velocity anomaly is considerably weaker and shallower to the south along the VFR (Fig 3a). Since the southward decrease in anomaly magnitude correlates with a narrowing of the basin, the possibility that the decrease results from a lack of resolution for long period Rayleigh waves

must be considered. However, the anomaly trend is apparent even in mid-period phase velocity maps (e.g. 37 s, see Fig. 2.6), with good resolution to the southern tip of the VFR (Fig. 2.7). In addition, preliminary results from independent analyses of shorter period Rayleigh and Love waves using ambient-noise tomography [*Zha et al.*, 2014] (Fig. 2.8) and body wave attenuation (Chapter 4) both provide evidence supporting a weaker slow velocity anomaly in the south (Section 2.4).

2.3. Discussions

Many factors, including temperature, composition, and melt, influence seismic velocity [e.g. *Hammond and Humphreys*, 2000; *Takei*, 2002; *Karato*, 2003; *Faul et al.*, 2004; *Jackson and Faul*, 2010; *McCarthy and Takei*, 2011]. To investigate these effects, we estimated the shear velocity structures of a "wet" but melt-free mantle wedge beneath the Lau Basin based on numerical models [*Harmon and Blackman*, 2010], using experimental results fitted with an extended Burgers model [*Jackson and Faul*, 2010] and corrections for the effect of water [*Karato*, 2012] and radial anisotropy [*Nishimura and Forsyth*, 1989] (Section 2.4.4 and Fig. 2.11). Although the predicted velocity structures (Fig. 2.11) are similar to our observations (Fig. 2.2), the modeling is unable to explain the very low *SV* velocities ($\leq$ 3.8 km/s) observed. The low velocities occur beneath the spreading centers at the depths expected for melt generation in the mantle (Fig. 2.3) and not in regions showing high water content, indicating that partial melt is the dominant factor. However, quantitative interpretation in terms of melt content is hampered by incomplete knowledge of the effects of melt on seismic velocity [*Faul et al.*, 2004; *McCarthy and Takei*, 2011].

We suggest that the extent and intensity of the low velocity anomaly provide constraints on the distribution and characteristics of the mantle melting process. The inclined LVZ (Fig. 2.2) shows a broad, asymmetric melting region originating at about 80 km depth, with the deepest part offset away from the slab, implying a passive decompression melting process governed by the mantle wedge flow pattern [*Conder et al.*, 2002; *Harmon and Blackman*, 2010]. Although it is difficult to quantitatively relate the low shear velocity observed beneath the CLSC to mantle porosity filled with melt (hereinafter referred as melt porosity), given the lowest shear velocity of about 3.9 km/s imaged beneath the East Pacific Rise [*Harmon et al.*, 2009], the porosity here is higher than beneath a fast-spreading MOR. This implies that the process of melt segregation at the CLSC is less efficient, consistent with the abnormally shallow depth of last melting equilibrium recorded in the lavas (about 35 km), as perfect segregation favors retention of high pressure chemical signatures (Section 2.4.5). The rapid spreading rate (about 90 mm/yr, i.e. high mantle matrix ascending rate), and high melt production due to high temperature both favor melt retention and high mantle porosities. Additionally, the higher spreading rate at the CLSC weakens the magmatic focusing at the ridge, hindering melt from being extracted [*Kohlstedt and Holtzman*, 2009].

The tomography results indicate that the MORB-like lavas erupting along the CLSC are derived from an upwelling zone (Fig. 2.2, A-A') originating from the ambient mantle to the west of the Lau back-arc, well away from sources of water and fluid-mobile elements in the subducting slab. Although the northern ELSC is much closer to the slab than CLSC, there is still a connection of the LVZ to the west (Fig. 2.2, B-B'), suggesting that the source of melt may be dominated by ambient mantle near and west of the ELSC rather than the subduction-influenced mantle. However, the VFR, characterized by high water content [*Kelley et al.*, 2006], shallow

axial depths [*Martinez and Taylor*, 2002], and anomalous major element compositions [*Escrig et al.*, 2009], lacks a sub-lithospheric melt zone to the west of the spreading axis (Fig. 2.2, C-C'). The horizontal component of corner flow in the mantle wedge beneath the VFR is likely slower than that beneath the CLSC [*Harmon and Blackman*, 2010], which may also lead to inefficient mantle supply from the west along the VFR. Therefore, although map-view results in Fig. 2.1 cannot resolve the details of this transition due to the low lateral resolution, the contrast between cross-sections B-B' and C-C' in Fig. 2.2 suggests that the sudden change in magma chemistry beginning at about 20˚35'S along the ELSC [*Escrig et al.*, 2009] represents the transition between spreading centers fed by decompression melting west of the axis, and those dominated by flux melting near the Tonga slab (Fig. 2.2).

Interpreting the along-strike variation of seismic anomalies is complicated, as both temperature and water content change from north to south [e.g. *Kelley et al.*, 2006]. The seismic anomaly variations are strongest at the depth of about 50 km, well beneath the lithosphere-asthenosphere boundary (LAB) according to the half-space cooling model (dotted curves in Fig. 2.2), excluding lithospheric cooling as a potential cause of this N-S variation. Furthermore, the trend in seismic velocity anomaly is opposite to the trend of the inferred source water content among the CLSC, ELSC and VFR, with areas of higher water content showing smaller and shallower seismic velocity anomalies (inset of Fig. 2.3). This contrast is surprising, given that the presence of water reduces the shear velocity in sub-solidus olivine by enhancing attenuation [*Karato*, 2003]. We constrain possible thermal variations along-strike by using lava composition and the thermobarometer of *Lee et al.* [2009] to estimate the *P-T* conditions of melting (Fig. 2.3, Fig. 2.12, and Section 2.4.5). Calculated melting paths reveal that the mantle is hotter beneath the CLSC than beneath VFR (Fig. 2.3), possibly due to less cooling by the slab. At 50 km depth,

the temperatures beneath the CLSC and VFR are about 1400˚C and 1350˚C, respectively. This difference would cause a reduction in shear wave velocity by only < 0.1 km/s (Section 2.4.5), much less than our observation of > 0.3 km/s.

Therefore, we interpret the along-strike variations of seismic anomalies in terms of changes in melt porosity. Our results suggest the highest melt porosity occurs beneath the NELB and CLSC, and decreases southward to the VFR. In contrast, higher melt production is not expected for the NELB in numerical models [*Harmon and Blackman*, 2010], and as sub-axial water content increases southward, the onset of partial melt would be expected to deepen [*Kelley et al.*, 2006] and the extent of melting would increase toward the VFR, opposite to our inferences (Fig. 2.3). However, melt porosity and extraction are not expected to follow a simple relationship with melt productivity, but rather may be governed by other factors such as permeability and melt viscosity.

We propose that the variations in seismic velocities along the Lau back-arc spreading centers reflect differences in melt porosity due to changes in the efficiency of melt extraction, determining the relation between melt content in the mantle and magmatic expression near the surface. The pattern of seismic anomalies suggests two major factors controlling the efficiency of melt transport. One factor is the existence of a nearby spreading center as a focus for upward melt transport. The lowest seismic velocities occur beneath the NELB at substantial distance from active spreading centers, suggesting the low permeability of the overlying lithosphere and the lack of effective magma channel prohibit melt extraction. This implies that melt generated in the mantle wedge beneath this region is not efficiently extracted, either slowly solidifying or migrating laterally large distances to one of the spreading centers.

The second major factor affecting melt porosity is the water content of the melt. Despite the

high degrees of melting of the mantle at VFR, the seismic velocities are faster throughout the melting region than beneath the CLSC, indicating greater melt extraction efficiency beneath the VFR where melts are wetter. Compared to the CLSC, the water-rich VFR melts apparently segregate from the mantle more efficiently, similar to the profile beneath the Tofua volcanic arc. Both the seismic images and the *P-T* calculations suggest that melt rises efficiently, ponds and re-equilibrates at the base of the thermal boundary layer (20-25 km depth) (Fig. 2.3). Although the presence of water enhances melting [*Kelley et al.*, 2006], it also reduces the melt viscosity [*Giordano et al.*, 2008] and facilitates grain growth [*Karato*, 1989]. If we assume the melt transport to be an equilibrium porous flow, it follows Darcy's law with $q \propto d^2\phi^n/\mu$, where q is the melt flux, d is the grain size, ϕ is the porosity, μ is the melt viscosity, and n is about 2.6 [*Miller et al.*, 2014]. Thus a decrease in melt viscosity and/or increase in grain size caused by higher water content would decrease melt porosity for a constant melt flux. In sum, our results and analysis indirectly imply that water greatly enhances melt mobility.

Ideally one could quantitatively relate the melt porosity inferred from seismology to melt extraction models of spreading centers. Unfortunately, there is no well-established relation linking seismic velocity and melt porosity. Many factors such as the grain size [*Jackson and Faul*, 2010] and the topology of the partial melt within the matrix [*Takei*, 2002] also affect seismic velocity; and other factors such as the behavior of "wet" melt under high pressure are poorly understood. Further experimental studies may provide the necessary constraints to relate seismic images directly to factors controlling melt production and transport.

2.4. Supplementary Materials

2.4.1. Data processing and inversion

Most of the data used in this study were collected from 49 broadband ocean-bottom seismographs (OBSs) deployed from November 2009 to November 2010 and 17 island-based seismic stations operated from October 2009 to December 2010. We additionally used data from 14 OBSs of the Lau Basin Ocean Bottom Seismograph Survey (LABATTS) and 9 island-based stations of the Southwest Pacific Seismic Experiment (SPASE) collected during September to December 1994 [*Zhao et al.*, 1997] (Fig. 2.1b and 2.5).

Based on the Preliminary Determination of Epicenters (PDE) catalogue, we selected seismograms of 357 earthquakes, with surface-wave magnitudes (M_s) larger than 4.5 and epicentral distances between 30º and 150º (inset of Fig. 2.5). The good azimuthal distribution of earthquakes guarantees a large number of ray-crossings north and south of the station array, improving resolution in the northern and southern Lau Basin (Fig. 2.7). The raw seismogram of each event was cut from the origin time of the earthquake to 12,000 seconds after. Prior to the tomographic inversion, data were down-sampled to 1 sps and instrument responses were removed. For each period of interest, we used a narrow bandpass filter (4th order Butterworth, zero-phase shift) centered at the frequency of interest to filter the seismograms. The filtered data were then windowed manually to isolate the fundamental mode of the Rayleigh wave at each period ranging from 19 to 118 s. Noise in seismograms at long periods (> 50 s) due to ocean swell and associated water pressure variations as well as tilt caused by local currents was removed by correcting vertical channel with horizontal and pressure channels [*Webb and Crawford*, 1999; *Crawford and Webb*, 2000; *Bell et al.*, 2015].

We then used the two-plane-wave method [*Forsyth and Li*, 2005] with 2-D Fréchet kernels

[*Yang and Forsyth*, 2006] to invert phase velocity with isotropic and anisotropic components at periods from 19 to 88 s. Periods longer than 88 s were not used since the wavelengths are too long compared to the size of our array to provide good resolutions. Unlike the traditional Rayleigh wave tomography based on ray theory, this method considers scattering effects of Rayleigh waves outside the study region by simplifying the scattered incoming wave as the sum of two interfering plane waves [*Forsyth and Li*, 2005]. Additionally, by using 2-D Fréchet kernels based on the starting model, scattering and multipathing effects within the study region can be also approximately addressed [*Yang and Forsyth*, 2006]. Both calculating the 2-D Fréchet kernels and the nonlinear tomographic inversion require a good starting velocity model. In the first step that determines the average phase velocity at each period for the entire study region, we chose the anisotropic model of the Pacific [*Nishimura and Forsyth*, 1989] (NF89 model hereinafter) with the age ranging 0 – 4 Myr as the starting model. In the second step, we divided the study region into four sub-regions according to tectonic settings: Lau Basin, Fiji Plateau/Lau Ridge, Tonga Ridge, and background. Then we used the average phase velocity as the starting model to invert the 2-D phase velocity map, with nodes spaced at 186.5 km, at each period. In the third step, we refined the grid of nodes to spacing of 124.3 and 58.7 km progressively, and used the previously inverted phase velocity as the *a priori* model.

Our results show strong azimuthal anisotropy in this region, consistent with previous studies [*Smith et al.*, 2001]. For instance, at the depth of 50 km, the fast direction is trench-parallel beneath the Lau Basin but convergence-parallel beneath the Lau Ridge and Fiji Plateau. Although the amplitude of anisotropy at each period varies by up to 5 % depending on the degree of regularization, the isotropic components of phase velocity show only very small changes (< 0.03 km/s) due to the good azimuthal coverage of the ray paths. Since the main purpose of this

work is to image the 3-D structure of seismic velocity and the inferred partial melt, only the isotropic phase velocities were analyzed in the next steps.

Subsequently, we inverted the azimuthally isotropic phase velocity at each node to determine the azimuthally averaged *SV* velocity using *Computer Programs in Seismology* [*Herrmann*, 2004]. We initially tried to invert the *SV* velocity with different uniform starting models based on NF89 models [*Nishimura and Forsyth*, 1989] or previous waveform inversions [*Wiens et al.*, 2006]. Since this linearized inversion may depend upon the starting model, we later divided the study region into six sub-regions: Lau Basin, Fiji Plateau/Lau Ridge, Tonga Ridge, North Fiji Basin, South Fiji Basin, and Pacific plate. The starting model for each sub-region was adopted from previous studies of seismic refraction [*Crawford et al.*, 2003], body wave tomography [*Conder and Wiens*, 2006], and NF89 models [*Nishimura and Forsyth*, 1989]. Each individual node was then sorted into one of these sub-regions, and the corresponding starting model was used in the inversion for the shear velocity structure at that node. Compared to the inversion results from a uniform starting model, the results inverted from starting models of 6 sub-regions are almost identical for mantle structure deeper than 30 km but improve a little for shallower structure that agrees with geological settings better. We therefore chose the later technique to obtain the final results of *SV* velocity. Furthermore, in order to test the robustness of the extremely slow velocity east of the CLSC, we applied the Monte-Carlo algorithm to invert the node that has the lowest velocity. Tests show that the extremely slow velocity east of the CLSC is robust, and shear velocity inverted by the linearized method [*Herrmann*, 2004] is reasonable (next section and Fig. 2.10).

2.4.2. Resolution of phase-velocity inversion

Inversion of phase velocity has an inevitable trade-off between spatial resolution and model resolution. Although shorter smoothing length with a finer grid of nodes could lead to more small-scale information (higher spatial resolution), the over-parameterized problem will be poorly solved in the inversion, resulting in lower model resolution and failing to provide useful details [*Forsyth and Li*, 2005]. We thus chose the inversion parameters mainly based on the model covariance and checkerboard tests (Fig. 2.7). For the largest node spacing of 186.5 km, we used a smaller *a priori* standard deviation (0.05 km/s) and larger smoothing length (200 km), giving results more damped to the starting model. As we reduced the spacing of nodes with subsequent iterations, inversion parameters for shorter periods were changed accordingly [*Rau and Forsyth*, 2011] so that phase velocity had more variability (*a priori* standard deviation as 0.15 km/s and smoothing length as 80 km for the finest grid of nodes spacing 58.7 km). The lack of spatial resolution at long periods is an intrinsic problem for surface wave tomography due to the large wavelength of waves and the consequent great width of the Fréchet kernel. For instance, the inferred subducting Pacific slab with dip angle gentler than shown by Slab 1.0 model [*Hayes et al.*, 2012] (Fig. 2.2) is an artifact due to the low resolution as the longer wavelength Rayleigh waves smear the horizontal structure more at larger depth. Since we were able to obtain useful resolution up to 88 s, only phase velocities at periods shorter than 90 s were used for the next step of shear-velocity inversion.

Ambient-noise tomography (ANT) uses “seismic noise” to invert phase velocity at shorter periods and to constrain shallower structures than are resolved by the two-plane-wave tomography (TPWT). ANT results [*Zha et al.*, 2014] of phase velocity at the period of 18 s (Fig. 2.8a) are consistent with phase velocity at 21 s obtained from TPWT, both showing weaker

signal of LVZ in the south. Furthermore, ANT results of shear velocity at the depth of 30 km (Fig. 2.8b) show great agreement with TPWT (Fig. 2.1c) not only in pattern but also absolute values. The smooth transition from shorter periods in ANT to longer periods in TPWT suggests our phase-velocity inversion is robust. Additionally, high attenuation anomalies revealed by independent body waves analysis (Chapter 4) have similar pattern to the LVZ in this study, supporting our results of weaker slow anomaly to the south.

Phase velocities at the CLSC are consistently slower than are observed at Marianas back-arc [*Pyle et al.*, 2010] and about 200 km west of the East Pacific Rise 12-18˚S [*Harmon et al.*, 2009], whereas only short-period phase velocities at the VFR are slower (Fig. 2.6). In addition, there are significant along-strike changes in the magnitude of this anomaly. In order to test our results of phase velocity, we applied the traditional two-station method for two sets of earthquake-station pairs (Fig. 2.9). The first set contains one earthquake at the Chile trench recorded by two stations north of the ELSC, and the second set has one earthquake at the Mariana trench recorded by two stations near the VFR. Fig. 2.9b and 6c show the seismograms of fundamental mode of Rayleigh wave filtered (4th order Butterworth, zero-phase shift) to 37 s. Given the differences of epicentral distance and phase delay times shown in Fig. 2.9, the average phase velocity between N01W and N03W is about 3.59 km/s, and that between A12W and S01W is about 3.67 km/s, consistent with phase velocity inverted by the TPWT (Fig. 2.6). These estimations of phase velocity are certainly approximate but lend evidence supporting our results of phase velocity.

2.4.3. Robustness of shear-velocity inversion

Linearized inversion [*Herrmann*, 2004] provides a fast way to invert shear velocity from phase velocity. However, the fixed thicknesses of model layers used in this method may lead to

bias in the inverted results. Therefore we additionally applied a Monte-Carlo algorithm to test the robustness of the extremely low velocity east of the CLSC (Fig. 2.10). This method generates an ensemble of models using random perturbations to both velocity and layer thickness of the linearized inverted model (starting model). It then calculates the dispersion curve for each model, and compares them with the original dispersion curve from the phase-velocity inversion. A "good" model is defined by two factors: (1) it should be as smooth as the linearized inverted model, and (2) its corresponding dispersion curve should have similar misfit compared to the starting model's dispersion curve. The "best" model is defined as the "good" model that has smallest misfit. Numerical experiments with the inversion for node 364 (Fig. 2.10) show that although the "best" model varies from inversion to inversion, the average of 500 "good" models is robust and almost identical to the linearly inverted model. The largest standard deviation of shear velocity over all depths is 0.13 km/s, much smaller than the range of perturbation set as 15 %, a.k.a., about 0.6 km/s. We thus conservatively estimate the uncertainty of the lowest velocity as 0.15 km/s. It is worthwhile to notice that the LVZ of our results is shallower than that from a previous waveform inversion study [*Wiens et al.*, 2006] (green curve in Fig. 2.10), agreeing with the geological setting better as melting commences 60-70 km deep beneath the passive MOR [*Shen and Forsyth*, 1995]. That is because the waveform inversion [*Wiens et al.*, 2006] averages over the whole back-arc and parts of the arc and Fiji Plateau. Therefore, we conclude that shear velocity inverted by the linearized method [*Herrmann*, 2004] is reasonable.

After trying various starting models and inversion parameters, an unexpected high-velocity zone (HVZ) deeper than about 100 km consistently appears in the result model, mainly due to the abnormally steep gradient of dispersion curve beyond 30 s. Beneath the node 364, the subducting slab is presumably about 200 km deep, leading to a difficulty to explain the HVZ

geologically. However, given the fact that a segment of the slab 100 km deep is only 100 km east of the node, and the wavelength for a 70 s Rayleigh wave, which is most sensitive to the depth of 100 km, is about 300 km, the HVZ can be explained as a smearing effect between the "fast" slab and the "slow" back-arc basin. As discussed in the last section, the intrinsic problem of low resolution at long periods is serious in the back-arc basin, since the lateral variations are too dramatic to be accurately resolved by the long wavelength surface waves. We thus limit our interpretation to the velocity structure shallower than 100 km, but have plotted structures between 100 and 120 km in the cross-sections for reference (Fig. 2.2).

For the same reason, the artificially high phase velocity at long periods, and the abnormally steep gradient of dispersion curve, may also result in a slight bias in the shear velocity at shallow depths in favor of slow velocities. Nevertheless, the fact that phase velocities at periods of 20 – 40 s are slower than those along the East Pacific Rise (Fig. 2.6) guarantees that the shear velocities at depths of 30 – 60 km are consistently lower than the East Pacific Rise.

It is worthwhile to examine whether the observed structures above 100 km deep are also artifacts due to this lateral "smearing", especially the LVZ extending westwards that are parallel to the dominant direction of the wave paths (cross-sections A-A' and B-B' in Fig. 2.2). Fig. 2.7 shows that even at the period of 50 s, most sensitive to the depth about 70 km, the lateral resolution is still good enough to resolve structures with a length scale of 200 km. In contrast, the results at 66 s show that even a larger length scale of 300 km cannot be resolved at periods of 66 s and longer, which are most sensitive to depths of 100 km and deeper. Additionally, preliminary results from independent analyses of body wave attenuation (Chapter 4) also reveal a connection between the CLSC and the asthenosphere beneath the Fiji Plateau, which is expected by the numerical models [*Harmon and Blackman*, 2010].

2.4.4. Predicting shear wave velocity

The extended Burgers model constrained by experimental data [*Jackson and Faul*, 2010] provides a link relating temperature to seismic velocity, incorporating the important effects of anelasticity. We first used recent 2-D numerical mantle wedge flow models [*Harmon and Blackman*, 2010] to predict shear velocity structures beneath the CLSC, ELSC, and VFR solely due to thermal variations. We corrected the predicted isotropic velocities to compare with our observed V_{SV} velocities by assuming that the isotropic shear velocity is the average of V_{SV} and V_{SH}, and using the radial anisotropic parameters of NF89 0-4 Myr model (V_{SH}/V_{SV} varies from 1.010 to 1.016) [*Nishimura and Forsyth*, 1989]. Water content affects seismic velocity via anelastic behavior, i.e., changing characteristic frequency of anelastic relaxation. We adopted an assumption by *Karato* [2012] that $\eta_{gbs} \propto Cw^r$, where η_{gbs} is grain-boundary viscosity, Cw is water content, and $r = 2$, and applied it into *Jackson and Faul*'s parameterizations to estimate water effects. Since the potential temperature used in the numerical models is 1450 ˚C [*Harmon and Blackman*, 2010], consistent with the value revealed at the CLSC but slightly higher than that at the ELSC and VFR [*Wiens et al.*, 2006], and the exponent constant r lies at the upper limit of *Karato* [2012] assumption ($r = 1 – 2$), the predicted *SV* velocity should be underestimated. We neglected the effects of other compositional variations on seismic velocity in this study, since previous geochemical studies suggest that Mg# of the mantle matrix varies less than ± 1 due to melt depletion [*Wasylenki et al.*, 2003] (Tables 2.1 and 2.2). These variations potentially lead to a change of ± 0.015 km/s in shear velocity [*Lee*, 2003], much smaller than the observed along-strike velocity change of > 0.3 km/s (inset of Fig. 2.3).

Fig. 2.11 shows calculated *SV* velocity under the considerations of temperature, water, and

radial anisotropy. We acknowledge that several parameters for the numerical models [*Harmon and Blackman*, 2010], the extended Burgers model [*Jackson and Faul*, 2010], and water effects [*Karato*, 2012] are poorly constrained. It is thus difficult to evaluate the uncertainty of Fig. 2.11. But these estimations at least provide a quantitative and visualized way to assess the importance of each physical property. On the other hand, previous studies of geology, petrology, and geochemistry all expected large amount of melt beneath the Lau basin [e.g. *Kelley et al.*, 2006; *Dunn and Martinez*, 2011], where the slow velocities are imaged. Therefore, we believe that it is reasonable to interpret the extremely low shear wave velocities as partial melting.

2.4.5. Melting paths and along-strike thermal variations

In order to estimate the temperature of the melting region beneath the Lau spreading centers, we applied a thermobarometer based on the Si and Mg contents of primary liquids in equilibrium with olivine+orthopyroxene [*Lee et al.*, 2009]. We downloaded data from PetDB (http://www.earthchem.org/petdb) [*Kamenetsky et al.*, 1997; *Lehnert et al.*, 2000; *Kent et al.*, 2002; *Tian et al.*, 2008; *Hahm et al.*, 2012; *Lytle et al.*, 2012], selecting only submarine glasses that have been analyzed for H_2O, and that are primitive enough to be related to primary mantle melts by olivine crystallization only. The latter condition was met by selecting only those samples with MgO greater than that calculated for the point of plagioclase appearance on the cotectic (parameterized from the relationships in Fig. 10 of *Langmuir et al.* [2006], as a function of H_2O, where MgO(plagioclase-in) = 8.18 - 0.93*H_2O). This resulted in only 4 samples from the CLSC, only 1 from the ELSC, and 6 from the VFR (Tables 2.1 and 2.2).

Even after selecting the most primitive basalts (listed in Tables 2.1 and 2.2), chemical compositions still need to be corrected for olivine crystallization before being input into the

mantle melt thermobarometer. In order to accomplish this, equilibrium olivine was added stepwise to the most primitive erupted compositions. We first calculated the composition of olivine in equilibrium with the erupted basaltic liquid using an Fe-Mg exchange coefficient between olivine and liquid of K_D(Fe/Mg)ol/liq = 0.3, next added 1% of that olivine to the melt compositions, and then calculated a new equilibrium olivine for the next 1% adding, and so on. This procedure iteratively continues until the latest calculated melt compositions are in equilibrium with mantle olivine, here assumed to have the composition of Fo90 (90 mol% Mg/[Mg+Fe]). Because only Fe^{2+} participates in this exchange relationship, the Fe^{3+}/Fe^{2+} of the melt must be known. We estimated $Fe^{3+}/\sum Fe$ from the concentration of H_2O in each sample, using the relationship in Fig. 3 of *Kelley and Cottrell* [2009] for MORB and back-arc magmas; this yielded values between 14 and 18% $Fe^{3+}/\sum Fe$. The corrected primary (Fo90) melt compositions were then input into the *Lee et al.* [2009] thermobarometer, and the resulting *P-T* values are interpreted here to represent the last pressure (*P*) and temperature (*T*) of equilibration of melts in the mantle. Since the assumption of the Mg/[Mg+Fe] of the mantle directly affects the *T* calculated, we consider Fo90 to be a minimum given the significant melt fractions (extents of melting) involved in this region, and so the calculated temperatures are minima for each sample.

Results in Fig. 2.12 show that the CLSC-ELSC melts record about 50 – 75°C higher temperature than those beneath the VFR, and reflect slightly higher pressures of equilibration (1.1 vs. 0.75 GPa, about 35 vs. 22 km). All pressures, however, are very shallow, and consistent with the top of the melting region in both cases. Such a condition could exist either because melts remained in equilibrium with the solid matrix during decompression, or because melts were extracted efficiently but pooled at the base of the thermal boundary layer and re-

equilibrated there. We prefer the former interpretation for the CLSC, due to the very low seismic velocities observed in the melting region (30-100 km) there, and the latter for the VFR, due to the higher observed seismic velocities and very shallow melt equilibration (comparable to the thermal boundary layer or the arc Moho, likely a rheological boundary where melts stall).

In order to backtrack the shallow equilibration conditions to those of the full melting region, we calculate melting paths for average CLSC and VFR primary melts. First, the extent of melting (*F*) is calculated for the final melt, from its *P*, *T* and H_2O, using the cryoscopic approach of *Langmuir et al.* [2006] and values for *dF/dT* from *Hirschmann* [2010] (3.7°/% melting, appropriate to 2 GPa, see his Fig. 1), depression of basalt liquidus temperature as a function of water from *Tenner et al.* [2012] (their 3-oxygen mole curve at 1 GPa), and peridotite/melt partition coefficient for H_2O (0.007) from Fig. 8 of *Hirschmann et al.* [2009]. The potential temperature of the mantle is then calculated by adding the heat of fusion (6°C/%) for that melt fraction, and projecting to 0 GPa along a solid adiabat with slope of 10°C/GPa. The H_2O concentration in the initial mantle is calculated from the H_2O concentration in the primary melt, the partition coefficient, and the degree of melting. The melting path was then calculated from the potential temperature and initial water content, using the same cryoscopic approach as above, taking into account the heat of fusion and solid adiabat.

The potential temperature (*Tp*) calculated in this way is about 1500°C for CLSC and about 1475°C for VFR. These *Tp* are at the high end of those estimated for MORs globally, and this has been a long-standing observation for Lau Basin [*Kelley et al.*, 2006; *Langmuir et al.*, 2006; *Wiens et al.*, 2006]. The *Tp* calculated using the method here for northern Lau glasses (1449°C for average MTJ and 1463°C for the FRSC) are nearly identical to those calculated in *Wiens et al.* [2006] using an independent method based on $Na_{(Fo90)}$ and $Fe_{(Fo90)}$ (*Tp* = 1449 ± 23 °C). The full

melting paths are shown in Fig. 2.12, with the CLSC mantle melting path maintaining about 50 – 75°C hotter than VRF mantle path throughout. The somewhat steeper trajectory for the VFR melting path reflects its higher water contents, which leads to greater overall extents of melting despite the lower initial temperature. The overall degrees of melting are very high (>30% for the VRF glasses), but this is consistent with the eruption of boninite liquids at the VFR (e.g., SiO_2 > 53%, TiO_2 < 0.5%, MgO > 8%), generally taken to reflect equilibration with refractory mantle that has melting past cpx-out [*Cooper et al.*, 2010].

At the depth of 50 km, the temperatures beneath the CLSC and VFR are about 1400 ˚C and 1350 ˚C, respectively. It is important to examine the implication of this thermal difference of 50 ˚C to our seismic observations. According to the extended Burgers model [*Jackson and Faul*, 2010], an increase of 50˚C at the depth of 50 km will lead to a decrease in shear wave velocity by < 0.1 km/s, much less than our observation of > 0.3 km/s. Additionally, experimental data for melt bearing samples [*Faul et al.*, 2004] show that attenuation becomes more dependent on temperature when melt is present, thus an increase in temperature may cause larger decrease in shear wave velocity than the melt-free model predicts [*Jackson and Faul*, 2010]. Following *Karato* [1993], we estimated shear wave velocity as a function of temperature T:

$$V(T) = V_0(T)\left[1 - \frac{1}{2Q(T)}\cot\left(\frac{\pi\alpha}{2}\right)\right] \tag{2.1}$$

where V_0 is the velocity at infinite frequency and α is the frequency-dependent exponent. Assuming attenuation doubles (Q^{-1} increases from 0.04 to 0.08) when temperature increases by 100˚C ($d(Q^{-1})/dT = 0.0004\ \mathrm{K}^{-1}$) [*Faul et al.*, 2004], reference V_0 = 4.0 km/s, and dV_0/dT = 0.000378 [*Stixrude and Lithgow-Bertelloni*, 2005], we have

$$\frac{dV}{dT} = \left\{\frac{dV_0}{dT}\left[1 - \frac{Q^{-1}}{2}\cot\left(\frac{\pi\alpha}{2}\right)\right] - \frac{d\left(Q^{-1}\right)}{dT}\frac{V_0}{2}\cot\left(\frac{\pi\alpha}{2}\right)\right\} \approx 0.002 \text{ km/s/K} \tag{2.2}$$

So the thermal difference of 50 ˚C between the CLSC and VFR may result in only 0.1 km/s change in shear wave velocity. Therefore, we suggest that the along-strike thermal variation is not sufficient to cause the observed change of seismic velocity, which requires a significant decrease of melt porosity toward the VFR.

References

Arai, R., and R. A. Dunn (2014), Seismological study of Lau back arc crust: Mantle water, magmatic differentiation, and a compositionally zoned basin, *Earth Planet. Sci. Lett.*, *390*, 304-317, doi: 10.1016/j.epsl.2014.01.014.

Bell, S. W., D. W. Forsyth, and Y. Ruan (2015), Removing Noise from the Vertical Component Records of Ocean‐Bottom Seismometers: Results from Year One of the Cascadia Initiative, *Bull. Seism. Soc. Amer.*, *105*(1), doi: 10.1785/0120140054.

Conder, J. A., D. A. Wiens, and J. Morris (2002), On the decompression melting structure at volcanic arcs and back-arc spreading centers, *Geophys. Res. Lett.*, *29*(15), 1727, doi: 10.1029/2002gl015390.

Conder, J. A., and D. A. Wiens (2006), Seismic structure beneath the Tonga arc and Lau back-arc basin determined from joint Vp, Vp/Vs tomography, *Geochem. Geophys. Geosyst.*, *7*(3), Q03018, doi: 10.1029/2005gc001113.

Cooper, L. B., T. Plank, R. J. Arculus, E. H. Hauri, P. S. Hall, and S. W. Parman (2010), High-Ca boninites from the active Tonga Arc, *J. Geophys. Res.*, *115*(B10), B10206, doi: 10.1029/2009jb006367.

Crawford, W. C., and S. C. Webb (2000), Identifying and Removing Tilt Noise from Low-Frequency (<0.1 Hz) Seafloor Vertical Seismic Data, *Bull. Seism. Soc. Amer.*, *90*(4), 952-963, doi: 10.1785/0119990121.

Crawford, W. C., J. A. Hildebrand, L. M. Dorman, S. C. Webb, and D. A. Wiens (2003), Tonga Ridge and Lau Basin crustal structure from seismic refraction data, *J. Geophys. Res.*, *108*(B4), 2195, doi: 10.1029/2001jb001435.

Dunn, R. A., and F. Martinez (2011), Contrasting crustal production and rapid mantle transitions beneath back-arc ridges, *Nature*, *469*(7329), 198-202, doi: 10.1038/nature09690.

Escrig, S., A. Bézos, S. L. Goldstein, C. H. Langmuir, and P. J. Michael (2009), Mantle source variations beneath the Eastern Lau Spreading Center and the nature of subduction components in the Lau basin–Tonga arc system, *Geochem. Geophys. Geosyst.*, *10*(4), doi: 10.1029/2008gc002281.

Faul, U. H., J. D. Fitz Gerald, and I. Jackson (2004), Shear wave attenuation and dispersion in melt-bearing olivine polycrystals: 2. Microstructural interpretation and seismological implications, *J. Geophys. Res.*, *109*(B6), B06202, doi: 10.1029/2003jb002407.

Forsyth, D. W., and A. Li (2005), Array Analysis of Two-Dimensional Variations in Surface Wave Phase Velocity and Azimuthal Anisotropy in the Presence of Multipathing Interference, in *Seismic Earth: Array Analysis of Broadband Seismograms*, edited by A. Levander and G. Nolet, pp. 81-97, American Geophysical Union, Washington, D. C.

Giordano, D., J. K. Russell, and D. B. Dingwell (2008), Viscosity of magmatic liquids: A model, *Earth Planet. Sci. Lett.*, *271*(1-4), 123-134, doi: 10.1016/j.epsl.2008.03.038.

Hahm, D., D. R. Hilton, P. R. Castillo, J. W. Hawkins, B. B. Hanan, and E. H. Hauri (2012), An overview of the volatile systematics of the Lau Basin – Resolving the effects of source variation, magmatic degassing and crustal contamination, *Geochimica et Cosmochimica Acta*, *85*(0), 88-113, doi: 10.1016/j.gca.2012.02.007.

Hammond, W. C., and E. D. Humphreys (2000), Upper mantle seismic wave velocity: Effects of realistic partial melt geometries, *J. Geophys. Res.*, *105*(B5), 10975-10986, doi: 10.1029/2000jb900041.

Harmon, N., D. W. Forsyth, and D. S. Weeraratne (2009), Thickening of young Pacific lithosphere from high-resolution Rayleigh wave tomography: A test of the conductive cooling model, *Earth Planet. Sci. Lett.*, *278*(1-2), 96-106, doi: 10.1016/j.epsl.2008.11.025.

Harmon, N., and D. K. Blackman (2010), Effects of plate boundary geometry and kinematics on mantle melting beneath the back-arc spreading centers along the Lau Basin, *Earth Planet. Sci. Lett.*, *298*(3-4), 334-346, doi: 10.1016/j.epsl.2010.08.004.

Hayes, G. P., D. J. Wald, and R. L. Johnson (2012), Slab1.0: A three-dimensional model of global subduction zone geometries, *J. Geophys. Res.*, *117*(B1), B01302, doi: 10.1029/2011jb008524.

Herrmann, R. B. (2004), Computer Programs in Seismology, edited, Earthquake Center, Saint Louis Unversity, St. Louis.

Hirschmann, M. M. (2000), Mantle solidus: Experimental constraints and the effects of peridotite composition, *Geochem. Geophys. Geosyst.*, *1*(10), 1042, doi: 10.1029/2000GC000070.

Hirschmann, M. M., T. Tenner, C. Aubaud, and A. C. Withers (2009), Dehydration melting of nominally anhydrous mantle: The primacy of partitioning, *Phys. Earth Planet. In.*, *176*(1–2), 54-68, doi: 10.1016/j.pepi.2009.04.001.

Hirschmann, M. M. (2010), Partial melt in the oceanic low velocity zone, *Phys. Earth Planet. In.*, *179*(1-2), 60-71, doi: 10.1016/j.pepi.2009.12.003.

Jackson, I., and U. H. Faul (2010), Grainsize-sensitive viscoelastic relaxation in olivine: Towards a robust laboratory-based model for seismological application, *Phys. Earth Planet. In.*, *183*(1-2), 151-163.

Kamenetsky, V. S., A. J. Crawford, S. Eggins, and R. Mühe (1997), Phenocryst and melt inclusion chemistry of near-axis seamounts, Valu Fa Ridge, Lau Basin: insight into mantle wedge melting and the addition of subduction components, *Earth Planet. Sci. Lett.*, *151*(3–4), 205-223, doi: 10.1016/S0012-821X(97)81849-3.

Karato, S. (1989), Grain growth kinetics in olivine aggregates, *Tectonophysics*, *168*(4), 255-273, doi: 10.1016/0040-1951(89)90221-7.

Karato, S.-I. (1993), Importance of anelasticity in the interpretation of seismic tomography, *Geophys. Res. Lett.*, *20*(15), 1623-1626, doi: 10.1029/93gl01767.

Karato, S.-I. (2003), Mapping water content in the upper mantle, in *Inside the Subduction Factory*, edited by J. M. Eiler, pp. 135-152, American Geophysical Union, Washington, DC.

Karato, S.-i. (2012), On the origin of the asthenosphere, *Earth Planet. Sci. Lett.*, *321-322*, 95-103, doi: 10.1016/j.epsl.2012.01.001.

Kelley, K. A., T. Plank, T. L. Grove, E. M. Stolper, S. Newman, and E. Hauri (2006), Mantle melting as a function of water content beneath back-arc basins, *J. Geophys. Res.*, *111*(B9), B09208, doi: 10.1029/2005jb003732.

Kelley, K. A., and E. Cottrell (2009), Water and the Oxidation State of Subduction Zone Magmas, *Science*, *325*(5940), 605-607, doi: 10.1126/science.1174156.

Kent, A. J. R., D. W. Peate, S. Newman, E. M. Stolper, and J. A. Pearce (2002), Chlorine in submarine glasses from the Lau Basin: seawater contamination and constraints on the composition of slab-derived fluids, *Earth Planet. Sci. Lett.*, *202*(2), 361-377, doi: 10.1016/S0012-821X(02)00786-0.

Kohlstedt, D. L., and B. K. Holtzman (2009), Shearing Melt Out of the Earth: An Experimentalist's Perspective on the Influence of Deformation on Melt Extraction, *Annu. Rev. Earth Planet. Sci.*, *37*(1), 561-593, doi: doi:10.1146/annurev.earth.031208.100104.

Langmuir, C. H., A. Bézos, S. Escrig, and S. W. Parman (2006), Chemical Systematics and Hydrous Melting of the Mantle in Back-Arc Basins, in *Back-Arc Spreading Systems: Geological, Biological, Chemical, and Physical Interactions*, edited by D. M. Christie, et al., pp. 87-146, American Geophysical Union.

Lee, C.-T. A. (2003), Compositional variation of density and seismic velocities in natural peridotites at STP conditions: Implications for seismic imaging of compositional heterogeneities in the upper mantle, *J. Geophys. Res.*, *108*(B9), 2441, doi: 10.1029/2003jb002413.

Lee, C.-T. A., P. Luffi, T. Plank, H. Dalton, and W. P. Leeman (2009), Constraints on the depths and temperatures of basaltic magma generation on Earth and other terrestrial planets using new thermobarometers for mafic magmas, *Earth Planet. Sci. Lett.*, *279*(1–2), 20-33, doi: 10.1016/j.epsl.2008.12.020.

Lehnert, K., Y. Su, C. H. Langmuir, B. Sarbas, and U. Nohl (2000), A global geochemical database structure for rocks, *Geochem. Geophys. Geosyst.*, *1*(5), 1012, doi: 10.1029/1999GC000026.

Lytle, M. L., K. A. Kelley, E. H. Hauri, J. B. Gill, D. Papia, and R. J. Arculus (2012), Tracing mantle sources and Samoan influence in the northwestern Lau back-arc basin, *Geochem. Geophys. Geosyst.*, *13*(10), Q10019, doi: 10.1029/2012GC004233.

Martinez, F., and B. Taylor (2002), Mantle wedge control on back-arc crustal accretion, *Nature*, *416*(6879), 417-420, doi: 10.1038/416417a.

McCarthy, C., and Y. Takei (2011), Anelasticity and viscosity of partially molten rock analogue: Toward seismic detection of small quantities of melt, *Geophys. Res. Lett.*, *38*(18), L18306, doi: 10.1029/2011GL048776.

Miller, K. J., W.-l. Zhu, L. G. J. Montési, and G. A. Gaetani (2014), Experimental quantification of permeability of partially molten mantle rock, *Earth Planet. Sci. Lett.*, *388*, 273-282, doi: 10.1016/j.epsl.2013.12.003.

Nishimura, C. E., and D. W. Forsyth (1989), The anisotropic structure of the upper mantle in the Pacific, *Geophys. J. Int.*, *96*(2), 203-229, doi: 10.1111/j.1365-246X.1989.tb04446.x.

Pearce, J. A., M. Ernewein, S. H. Bloomer, L. M. Parson, B. J. Murton, and L. E. Johnson (1994), Geochemistry of Lau Basin volcanic rocks: influence of ridge segmentation and arc proximity, *Geological Society, London, Special Publications*, *81*(1), 53-75, doi: 10.1144/gsl.sp.1994.081.01.04.

Pyle, M. L., D. A. Wiens, D. S. Weeraratne, P. J. Shore, H. Shiobara, and H. Sugioka (2010), Shear velocity structure of the Mariana mantle wedge from Rayleigh wave phase velocities, *J. Geophys. Res.*, *115*(B11), B11304, doi: 10.1029/2009jb006976.

Rau, C. J., and D. W. Forsyth (2011), Melt in the mantle beneath the amagmatic zone, southern Nevada, *Geology*, *39*(10), 975-978, doi: 10.1130/g32179.1.

Shen, Y., and D. W. Forsyth (1995), Geochemical constraints on initial and final depths of melting beneath mid-ocean ridges, *J. Geophys. Res.*, *100*(B2), 2211-2237, doi: 10.1029/94jb02768.

Smith, G. P., D. A. Wiens, K. M. Fischer, L. M. Dorman, S. C. Webb, and J. A. Hildebrand (2001), A Complex Pattern of Mantle Flow in the Lau Backarc, *Science*, *292*(5517), 713-716, doi: 10.1126/science.1058763.

Stixrude, L., and C. Lithgow-Bertelloni (2005), Mineralogy and elasticity of the oceanic upper mantle: Origin of the low-velocity zone, *J. Geophys. Res.*, *110*(B3), B03204, doi: 10.1029/2004jb002965.

Takei, Y. (2002), Effect of pore geometry on V_P/V_S: From equilibrium geometry to crack, *J. Geophys. Res.*, *107*(B2), 2043, doi: 10.1029/2001jb000522.

Taylor, B., K. Zellmer, F. Martinez, and A. Goodliffe (1996), Sea-floor spreading in the Lau back-arc basin, *Earth Planet. Sci. Lett.*, *144*(1-2), 35-40, doi: 10.1016/0012-821x(96)00148-3.

Tenner, T. J., M. M. Hirschmann, and M. Humayun (2012), The effect of H_2O on partial melting of garnet peridotite at 3.5 GPa, *Geochem. Geophys. Geosyst.*, *13*(3), Q03016, doi: 10.1029/2011GC003942.

Tian, L., P. R. Castillo, J. W. Hawkins, D. R. Hilton, B. B. Hanan, and A. J. Pietruszka (2008), Major and trace element and Sr–Nd isotope signatures of lavas from the Central Lau Basin: Implications for the nature and influence of subduction components in the back-arc mantle, *Journal of Volcanology and Geothermal Research*, *178*(4), 657-670, doi: 10.1016/j.jvolgeores.2008.06.039.

Wasylenki, L. E., M. B. Baker, A. J. R. Kent, and E. M. Stolper (2003), Near-solidus Melting of the Shallow Upper Mantle: Partial Melting Experiments on Depleted Peridotite, *J. Petrology*, *44*(7), 1163-1191, doi: 10.1093/petrology/44.7.1163.

Webb, S. C., and W. C. Crawford (1999), Long-period seafloor seismology and deformation under ocean waves, *Bull. Seism. Soc. Amer.*, *89*(6), 1535-1542.

Wiens, D. A., K. A. Kelley, and T. Plank (2006), Mantle temperature variations beneath back-arc spreading centers inferred from seismology, petrology, and bathymetry, *Earth Planet. Sci. Lett.*, *248*(1-2), 30-42.

Yang, Y., and D. W. Forsyth (2006), Regional tomographic inversion of the amplitude and phase of Rayleigh waves with 2-D sensitivity kernels, *Geophys. J. Int.*, *166*(3), 1148-1160, doi: 10.1111/j.1365-246X.2006.02972.x.

Zha, Y., S. C. Webb, S. S. Wei, D. A. Wiens, D. K. Blackman, W. Menke, R. A. Dunn, and J. A. Conder (2014), Seismological imaging of ridge–arc interaction beneath the Eastern Lau Spreading Center from OBS ambient noise tomography, *Earth Planet. Sci. Lett.*, *408*, 194-206, doi: 10.1016/j.epsl.2014.10.019.

Zhao, D., Y. Xu, D. A. Wiens, L. Dorman, J. Hildebrand, and S. Webb (1997), Depth Extent of the Lau Back-Arc Spreading Center and Its Relation to Subduction Processes, *Science*, *278*(5336), 254-257, doi: 10.1126/science.278.5336.254.

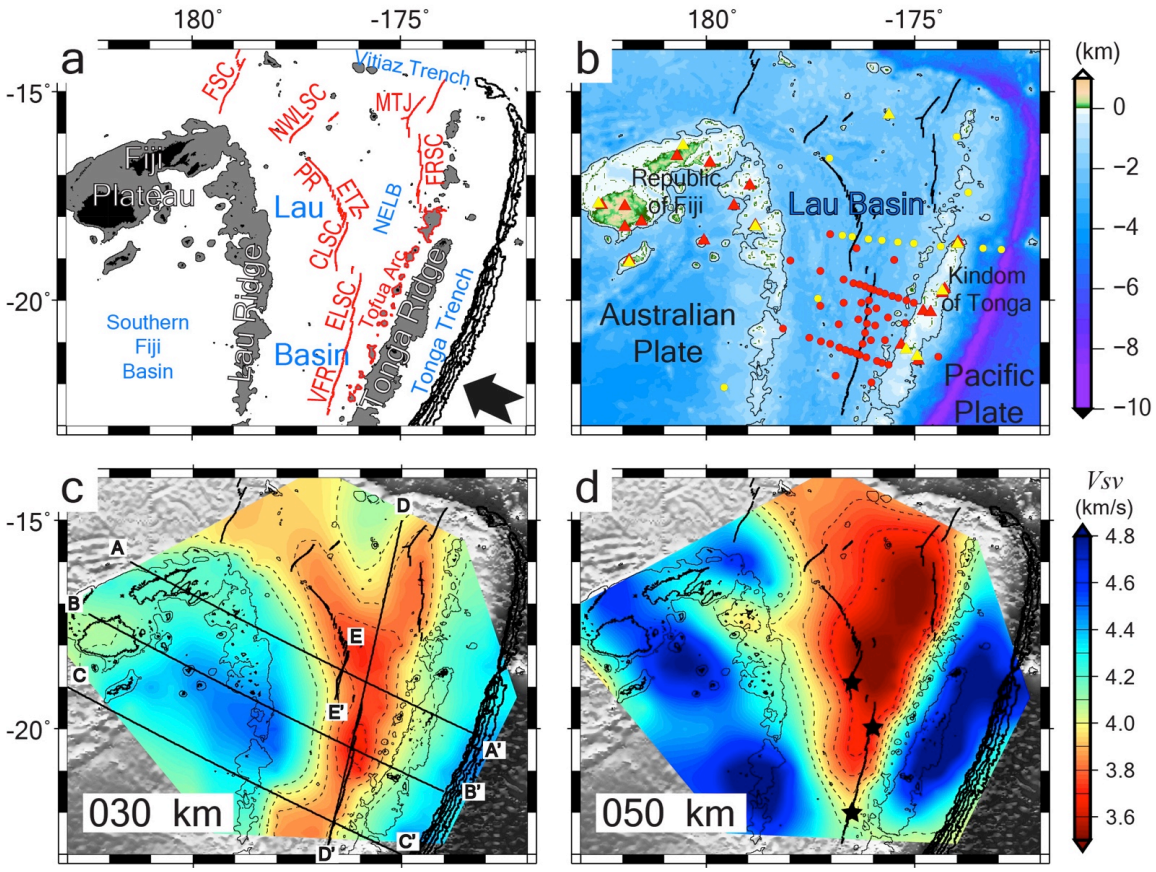

Figure 2.1. Maps of the study region and mantle velocities.

(a) Tectonic map of the Lau Basin and adjacent areas with back-arc spreading centers (red lines). The Pacific plate subducts beneath the Tonga trench (delineated by bathymetry contours of 7, 8, 9, and 10 km) from the southeast (bold arrow). Areas with bathymetry shallower than 1 and 0 km are shaded in grey and black, respectively. Features with active magmatism have red labels. Volcanoes of the Tofua arc are contoured in red. CLSC, Central Lau Spreading Center; ELSC, East Lau Spreading Center; ETZ, Extensional Transform Zone; FRSC, Fonualei Rift and Spreading Center; FSC, Futuna Spreading Center; MTJ, Mangatolu Triple Junction; NWLSC, Northwest Lau Spreading Center; NELB, North-eastern Lau Basin; VFR, Valu Fa Ridge. (b) Seismic stations used in this study. Bathymetry of 1000 m is contoured. Red triangles represent island-based stations operated from Oct. 2009 to Dec. 2010. Red dots are OBSs deployed from

Nov. 2009 to Nov. 2010. Yellow dots and triangles indicate OBSs and island-based stations operated during Sep. to Dec. 1994, respectively (see Fig. 2.5 for details). (c) Azimuthally averaged *SV* velocity at the depth of 30 km. Straight lines show the cross-sections in Fig. 2.2 and 3. (d) Azimuthally averaged *SV* velocity at the depth of 50 km. Black stars are the nodes representing the CLSC, ELSC, and VFR in the inset of Fig. 2.3 and Fig. 2.6. In (c) and (b), shear velocity of 3.7, 3.8, 3.9, 4.0, and 4.1 km/s are contoured by dashed lines. Bathymetry contours are the same in (b).

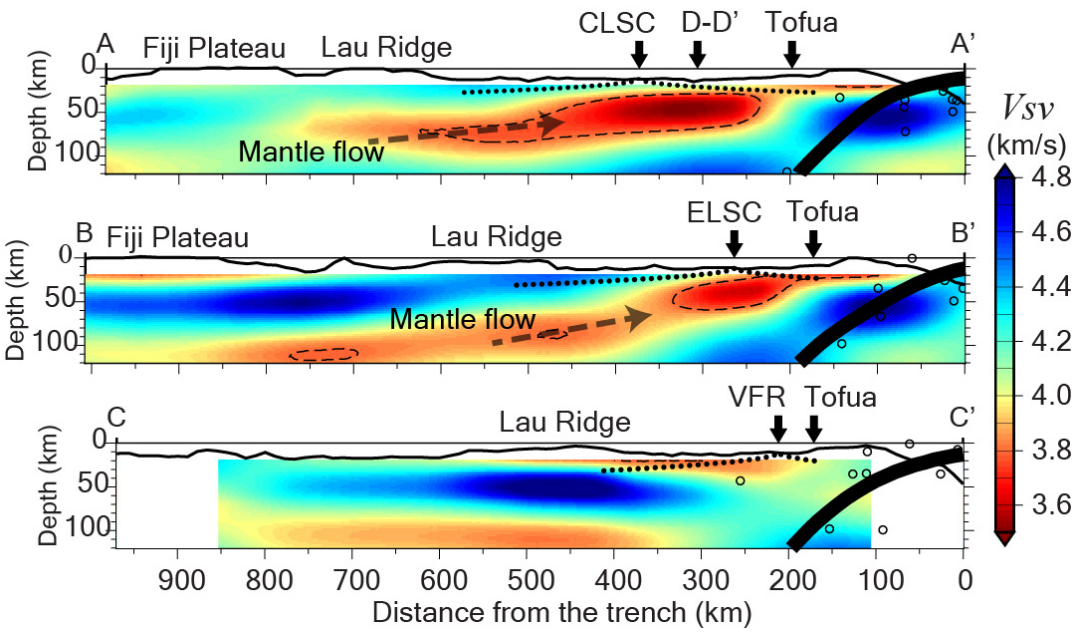

Figure 2.2. Cross-sections A-A', B-B', and C-C' showing azimuthally averaged *SV* velocity. Due to the low lateral resolution of surface waves at long periods, only structures above 100 km are well resolved and thus interpreted. Local earthquakes (black circles, within ±100 km away) located using the same dataset delineate the surface of the subducting slab (bold curves, Slab 1.0 model [*Hayes et al.*, 2012]). Dotted curves represent the bottom of the thermal lithosphere according to the half-space cooling model, demonstrating that most of the imaged velocity anomalies do not result from variations in conductive cooling. The bathymetry (curve along the top) is exaggerated vertically by a factor of 5. Shear velocity of 3.8 km/s is contoured by dashed lines. Beneath the CLSC and ELSC, the decompression melting occurs in slow velocity regions interpreted as upwelling mantle from the west. In contrast, beneath the VFR in the south (C-C'), any connection between the ridge and the asthenosphere to the west is impeded by the lithosphere of the relict arc (wide blue anomaly beneath the Lau Ridge at 30-70 km depth), implying the material supply of back-arc mantle from the west is much weaker and the spreading center samples only mantle in close proximity to the slab.

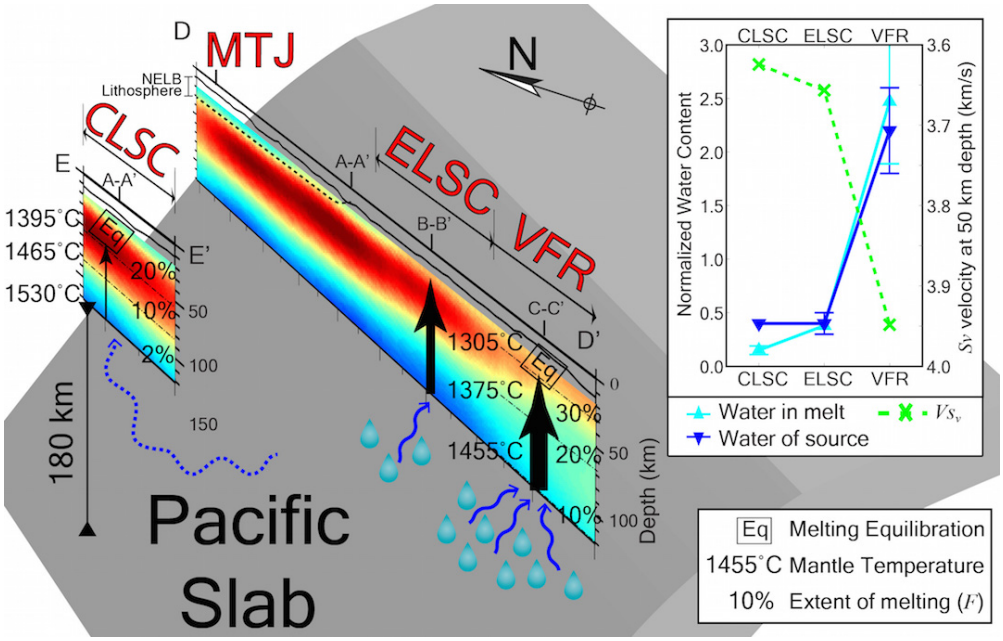

Figure 2.3. Cross-sections D-D' and E-E' of azimuthally averaged *SV* velocity with a schematic model showing the along-strike variations.

The *SV* velocity color scale is the same in Fig. 2.2. The dashed contour represents a thin lithosphere with low permeability overlying the NELB. Mantle temperatures, extent of melting, and depth of melt equilibration ("Eq" in a box) beneath the CLSC and VFR are estimated from the thermobarometer of *Lee et al.* [2009], based on the Si and Mg concentration of primary melts in equilibrium with mantle olivine+orthopyroxene (Section 2.4.5). The melting path beneath the ELSC is not available due to the limited data for H_2O in primitive melts. Black arrows in the cross-sections represent upward melt transport, and blue wavy lines indicate water migration. In the north where the CLSC is far from the slab, melts equilibrate at the depth of about 35 km with the maximum extent of melting of about 25%. In contrast, relatively colder mantle with greater water content beneath the VFR generates melts that equilibrate about 10 km shallower than CLSC and with about 10 % higher total extent of melting. As the distance between the spreading center and the Tofua arc decreases, more water enters the melting region, leading to an

enhancement in melt extraction (wider arrow represents more efficient melt transport). Inset diagram shows trends of water concentration in the melt (Section 2.4.5 and Tables 2.1 and 2.2) and the mantle source [*Kelley et al.*, 2006] in contrast to our results of shear wave velocity at the depth of 50 km. Error bars indicate the standard deviation among all samples (absence of error bars indicates there is only one measurement). *SV* velocity of each spreading center is chosen as velocity of the corresponding node shown in Fig. 2.1d.

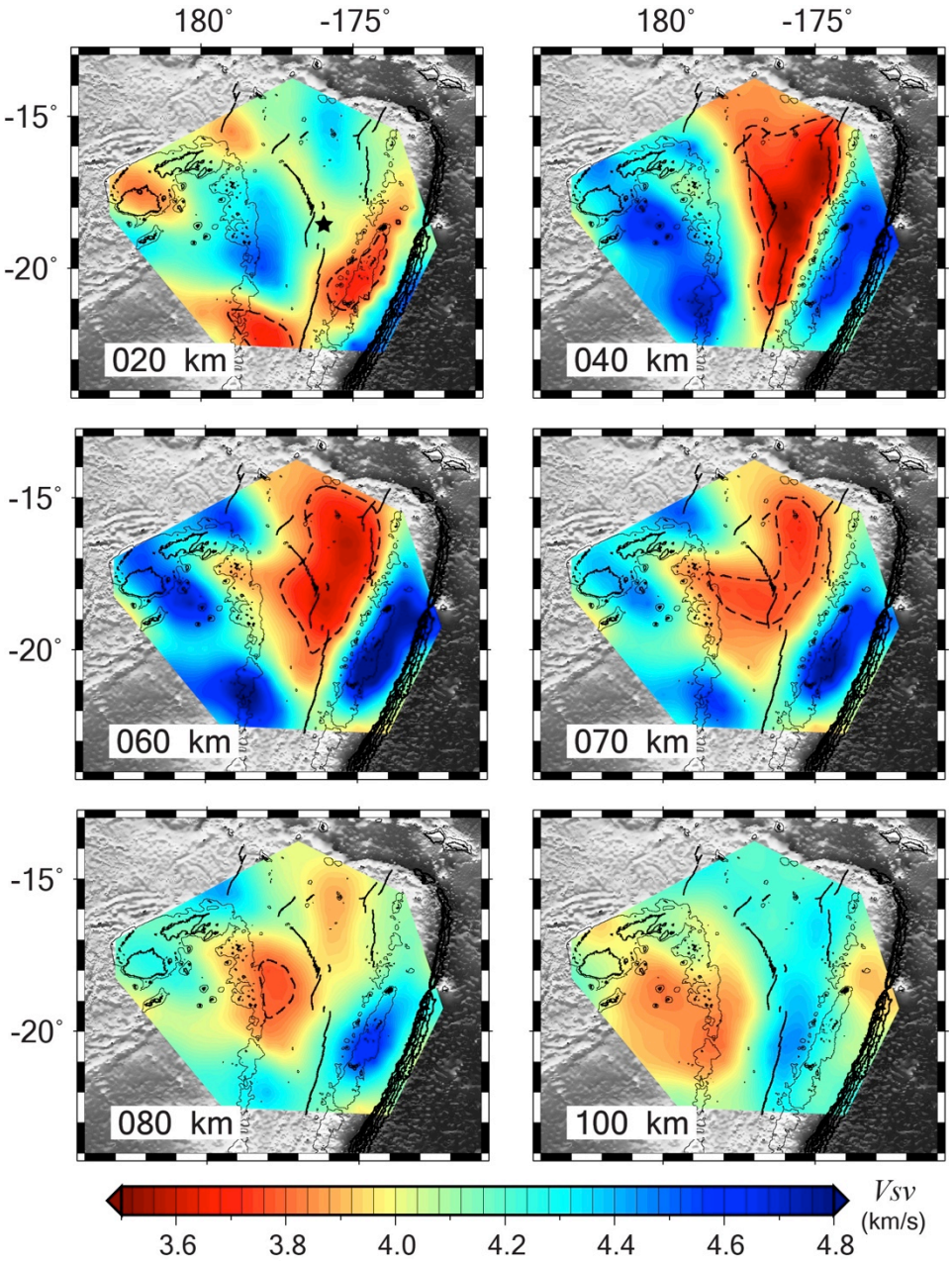

Figure 2.4. Maps of azimuthally averaged *SV* velocity at depths of 20, 40, 60, 70, 80, and 100 km.

Shear velocity of 3.8 km/s is contoured. Star illustrates the node 364 used in the Monte-Carlo inversion (Fig. 2.10). Spreading centers and bathymetry contours are labeled the same as Fig. 2.1c.

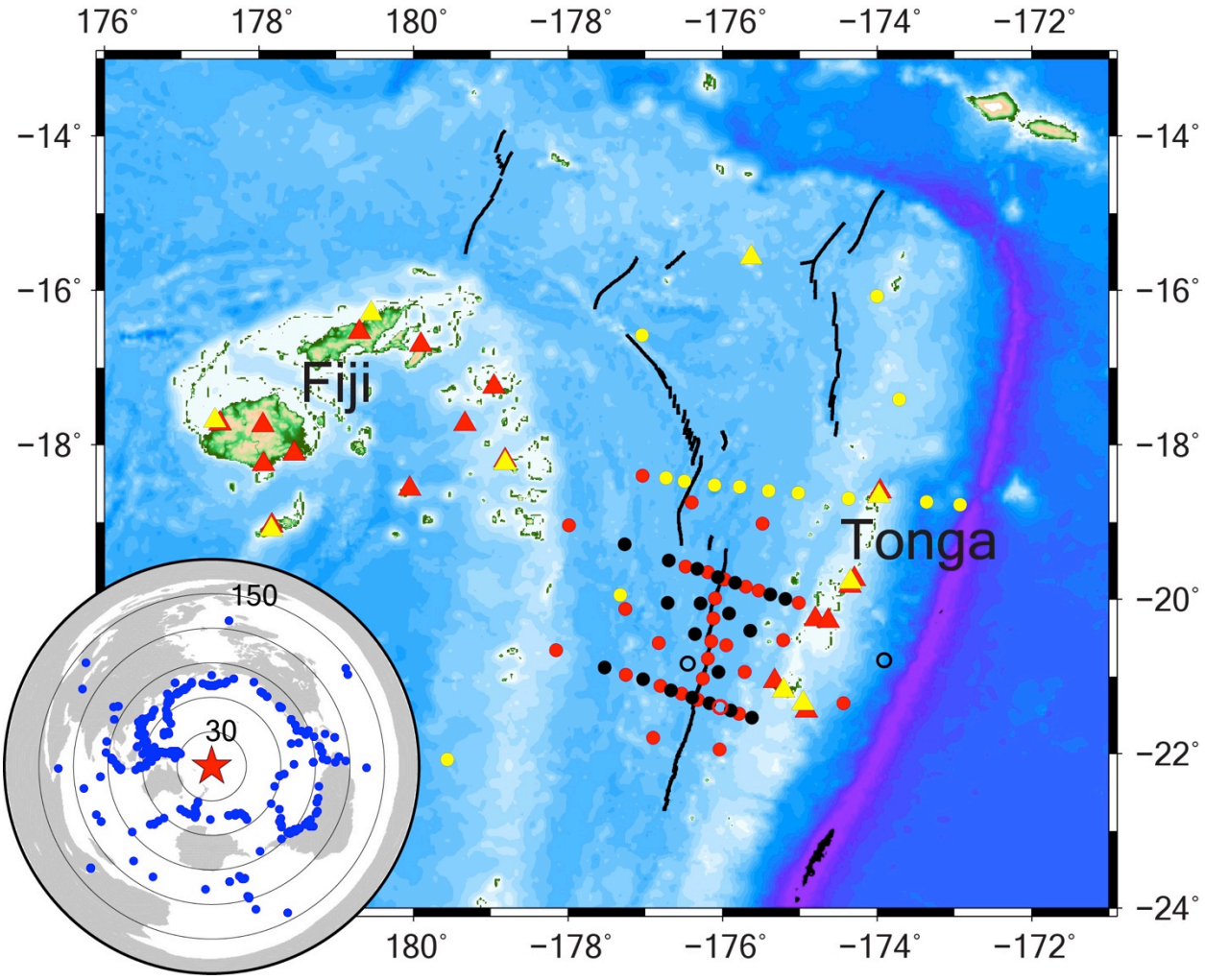

Figure 2.5. Seismic stations and earthquakes used in this study.

Red triangles represent island-based stations operated from Oct. 2009 to Dec. 2010. Red and black dots are WHOI (Woods Hole Oceanographic Institution) and LDEO (Lamont-Doherty Earth Observatory) OBSs deployed from Nov. 2009 to Nov. 2010. Open circles mean unrecovered OBSs. Yellow dots and triangles indicate OBSs and island-based stations deployed during Sep. to Dec. 1994, respectively. Spreading centers and bathymetry are labeled the same as Fig. 2.1b. The inset shows the earthquakes (blue dots) used in this study centered at the Lau Basin (red star).

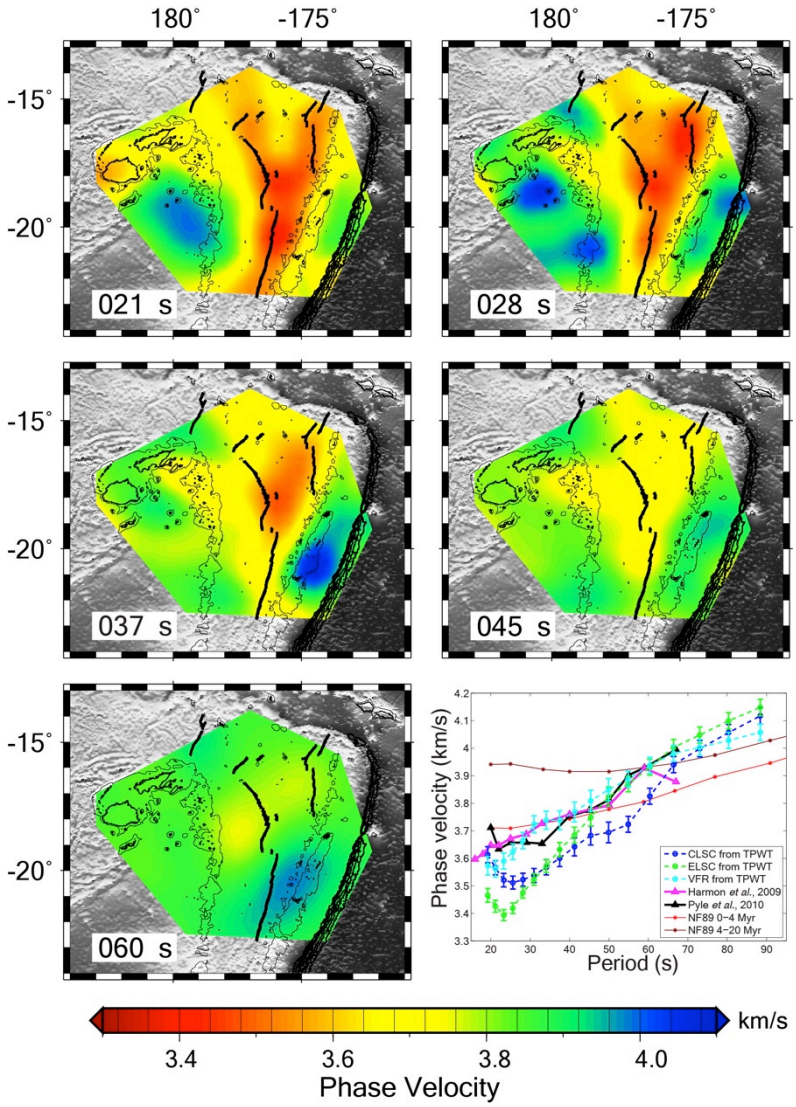

Figure 2.6. Maps of azimuthally isotropic phase velocity at periods of 21, 28, 37, 45, and 60 s inverted with the finest inverting grid.

Spreading centers and bathymetry contours are labeled the same as Fig. 2.1c. Dispersion curves at the CLSC (blue), ELSC (green), VFR (cyan), East Pacific Ridge [*Harmon et al.*, 2009] (magenta), Marians [*Pyle et al.*, 2010] (black), and NF89 models [*Nishimura and Forsyth*, 1989] (red and dark red). The CLSC, ELSC, and VFR are represented by nodes shown in Fig. 2.1d. Error bars indicate the standard deviations of phase velocity.

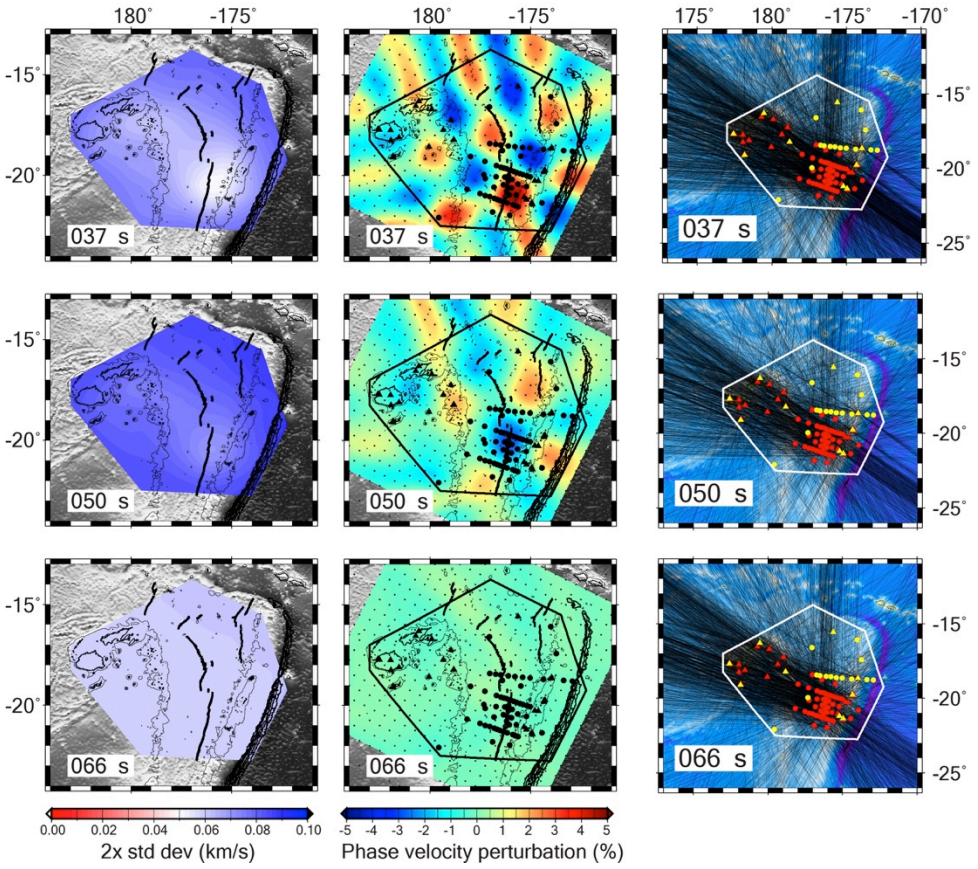

Figure 2.7. Robustness of the phase-velocity inversion at periods of 37, 50 and 66 s. Rayleigh waves at these periods are most sensitive to the depths of about 50 km (where the lowest velocity is), 70 km (where the inclined LVZ extends away from the trench), and 100 km (the maximum depth to be interpreted), respectively. Left panels: maps of double standard deviation inverted with the finest grid. Middle panels: resolution test of phase-velocity inversion with the finest inverting grid (regularly spacing black points). Black dots and triangles represent 63 OBSs and 26 land-based seismic stations used in this study, respectively. Area within the black polygon is chosen as the result-displaying region according to the reasonable resolutions of phase-velocity inversion at all periods. Spreading centers and bathymetry contours are labeled the same as Fig. 2.1c. Right panels: Rayleigh wave ray-paths (black lines) used in phase-velocity inversion. Seismic stations are labeled the same as Fig. 2.1b.

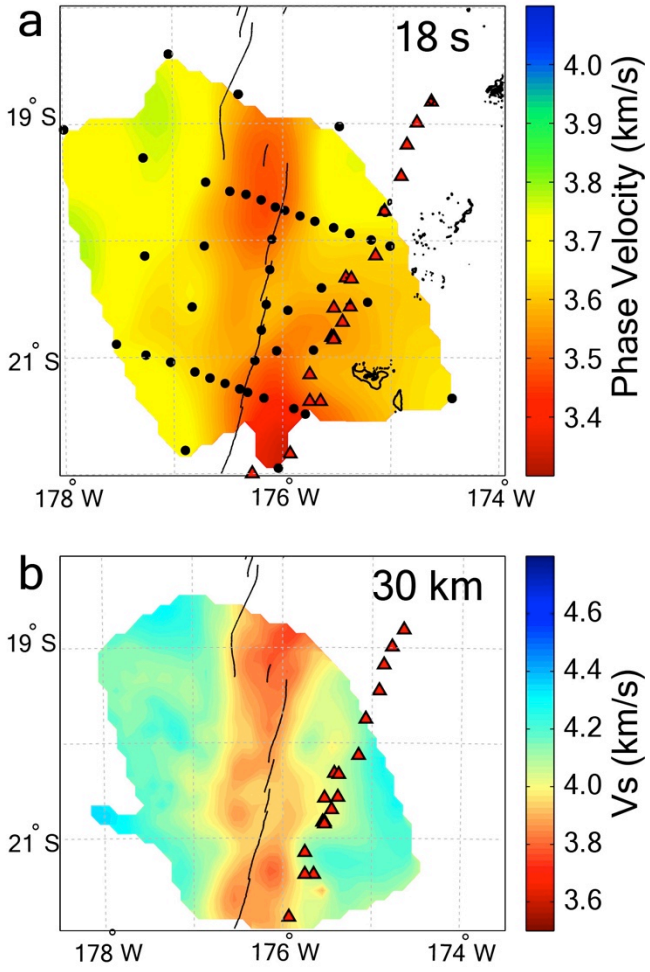

Figure 2.8. Results of ambient-noise tomography from *Zha et al.* [2014].

(a) Isotropic phase velocity of Rayleigh wave at the period of 18 s. Black dots indicate the OBSs used in this study, red triangles represent active volcanoes, and black lines mean the spreading centers. (b) Azimuthally averaged *SV* velocity at the depth of 30 km.

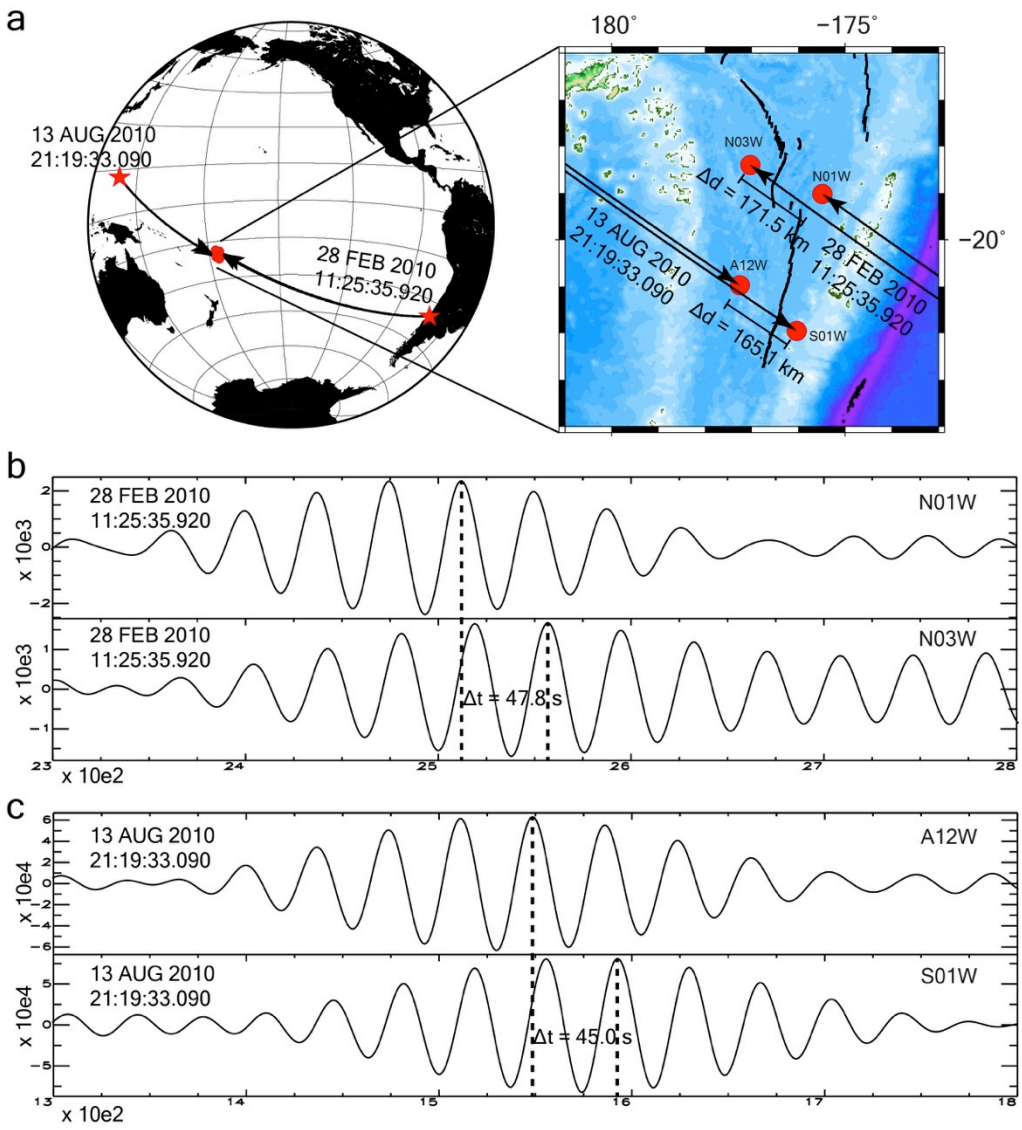

Figure 2.9. Two examples of phase velocity measured by two-station method.

(a) Surface wave (black curves) of two earthquakes (red stars) propagated to four OBSs (red dots). (b) The earthquake at the Chile trench was recorded by station N01W and N03W. Difference of epicentral distances is about 171.5 km. Rayleigh wave at the period of 37 s has a delay time of 47.8 s, suggesting a phase velocity of 3.59 km/s. (c) The earthquake at the Mariana trench was recorded by station A12W and S01W. Difference of epicentral distances is about 165.1 km. Rayleigh wave at period of 37 s has a delay time of 45.0 s, suggesting a phase velocity of 3.67 km/s.

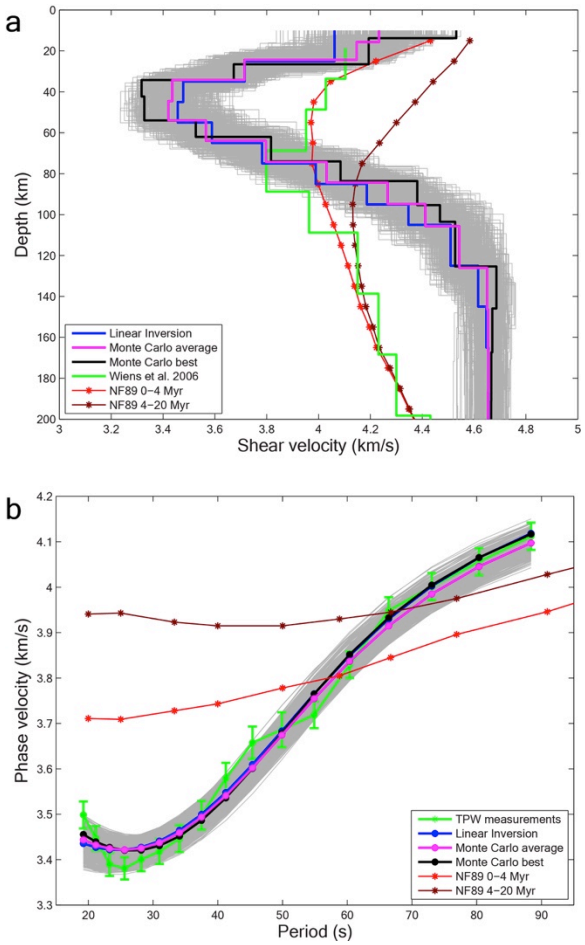

Figure 2.10. Shear-velocity inversion of Monte-Carlo algorithm for the node 364.

(a) Models of shear velocity. (b) Forwardly calculated dispersion curves. Each grey curve indicates one "good" model whose smoothness and misfit are smaller than the criteria. Blue, magenta, black, red, and dark red curves represent the model from linearly inversion, average model, best model of Monte-Carlo inversion, and NF89 models of two age categories [*Nishimura and Forsyth*, 1989], respectively. In (a), *Wiens et al.* [2006] model of *SV* velocity (green) is shown as the green curve for reference. In (b), green curve indicates phase velocities inverted by TPWT, with error bars showing the standard deviations.

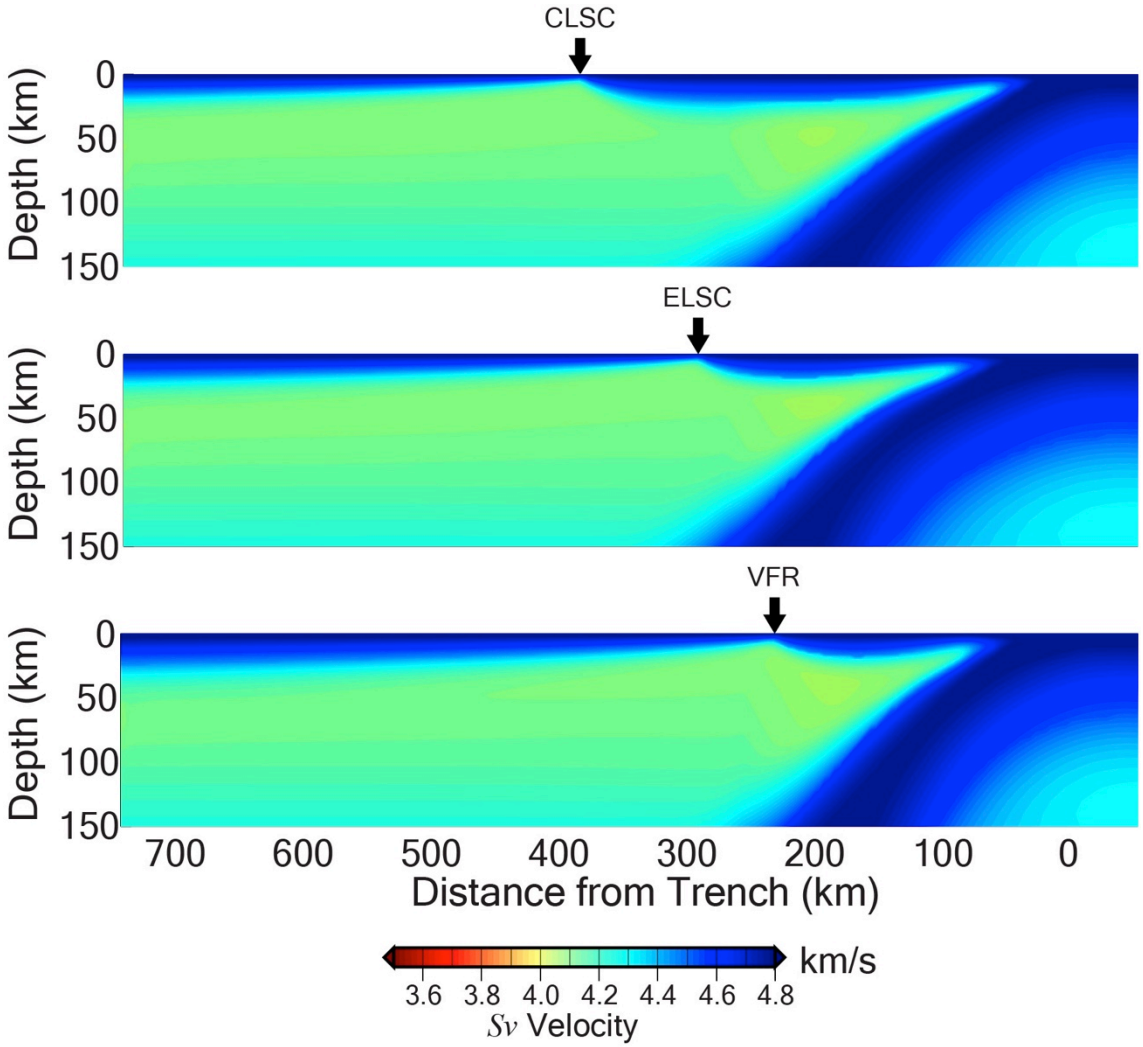

Figure 2.11. Cross-sections of predicted shear velocity.

Calculations are based on numerical models of temperature and water content [*Harmon and Blackman*, 2010], extended Burgers model [*Jackson and Faul*, 2010], and corrections of radial anisotropy [*Nishimura and Forsyth*, 1989] and effects of water [*Karato*, 2012]. Notice the color scale is the same in Fig. 2.2. Although compared to the CLSC, the temperature beneath the VFR is lower due to the slab cooling, potentially increasing the seismic velocity, the much higher water content reduces the velocity more significantly and leads to a stronger signal of low velocity in the prediction.

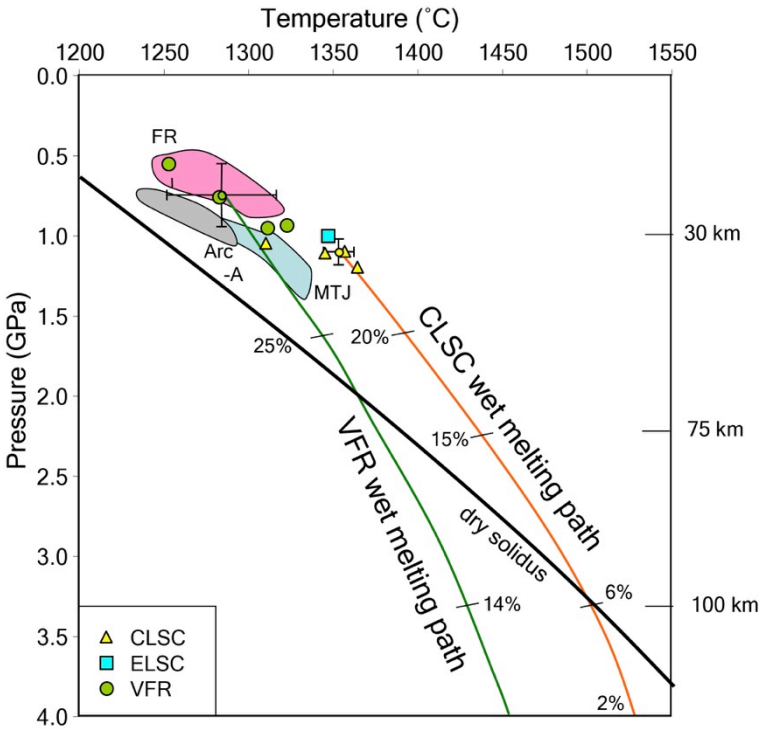

Figure 2.12. Pressures and temperatures of equilibration of Lau Basin glasses with Fo90 mantle.

We used major elements, H_2O measurements, f_{O2} constraints and the thermobarometer of *Lee et al.* [2009] to calculate *P-T* paths for most primitive melts (crystallizing olivine only). Back-arc averages for VFR and CLSC-ELSC high-temperature cluster are shown with smaller symbols and error bars for ± 1 s.d. Fields are given for FRSC, MTJ and Tonga Arc Volcano A for comparison. All data are from PetDB [*Kamenetsky et al.*, 1997; *Lehnert et al.*, 2000; *Kent et al.*, 2002; *Tian et al.*, 2008; *Hahm et al.*, 2012; *Lytle et al.*, 2012] and *Cooper et al.* [2010]. Dry solidus is from *Hirschmann* [2000]. Back-arc averages are backtracked along wet decompression melting paths, using method given in Section 2.4.5.

Table 2.1. Erupted Compositions downloaded from PetDB

(http://www.earthchem.org/petdb) [*Lehnert et al.*, 2000]

Region	Sample	Latitude (˚)	Longitude (˚)	Elevation (m)	Reference	SiO_2	TiO_2	$Al2O_3$	FeOT	MnO	MgO	CaO	Na_2O	K_2O	P_2O_5	H_2O, wt%	Fe^{3+}/FeT	Mg#	MgO-pl-in
CLSC	SSV0708-061-001-001	-18.206	-176.39	-2188	*Lytle et al.* [2012]	50.49	0.71	15.04	9.38	0.18	8.64	14.02	1.92	0.03	0.06	0.09	0.14	63	8.10
CLSC	WASRNDB-026-002	-18.228	-176.26	-2296	*Tian et al.* [2008]; *Hahm et al.* [2012]	50.64	0.93	15.52	9.63	0.20	8.46	13.25	2.05	0.05	0.06	0.12	0.14	62	8.07
CLSC	SSV0708-063-001-001	-18.257	-176.45	-2716	*Lytle et al.* [2012]	48.77	0.78	17.33	8.36	0.14	10.36	12.85	1.98	0.01	0.05	0.06	0.14	69	8.12
CLSC	SSV0708-062-001-001	-18.347	-176.50	-2523	*Lytle et al.* [2012]	50.16	0.90	15.44	9.08	0.18	8.74	13.96	2.12	0.04	0.06	0.08	0.14	64	8.10
ELSC	WASRNDB-005-008	-19.908	-176.06	-2436	*Tian et al.* [2008]; *Hahm et al.* [2012]	51.32	0.89	14.93	9.28	0.18	8.14	13.19	1.94	0.04	0.06	0.24	0.14	62	7.96
VFR	SO48/61GC	-21.822	-176.44	1760	*Kent et al.* [2002]	51.01	0.68	15.36	8.33	0.16	7.79	12.63	1.51	0.23	0.08	1.30	0.16	64	6.97
VFR	SO35/84KD1	-22.140	-176.61	1723	*Kent et al.* [2002]	50.36	0.76	15.92	8.86	0.16	7.31	12.61	1.55	0.16	0.06	1.26	0.16	61	7.00
VFR	SON0048-114	-22.188	-176.54	-1500	*Kent et al.* [2002]	50.91	0.58	15.05	9.21	0.19	7.10	12.30	1.35	0.28	0.08	1.35	0.16	59	6.92
VFR	SON0035-128	-22.290	-176.57	-1550	*Kamenetsky et al.* [1997]	53.38	0.50	13.44	8.45	0.23	8.20	11.98	1.25	0.51	0.09	2.05	0.18	65	6.27

* H_2O concentration as measured in glasses; MgO-pl-in is MgO calculated for appearance of plagioclase on the cotectic [*Langmuir et al.*, 2006].

** Fe^{3+}/FeT calculated from H_2O, using correlation in *Kelley and Cottrell* [2009].

Table 2.2 Calculated primary mantle melt compositions

Region	Sample	SiO_2	TiO_2	Al_2O_3	FeO	MnO	MgO	CaO	Na_2O	K_2O	P_2O_5	H_2O	Fe_2O_3	Mg#	T (°C)	P (GPa)
CLSC	SSV0708-061-001-001	49.19	0.63	13.43	8.35	0.16	12.60	12.52	1.71	0.03	0.05	0.08	1.30	70	1357.35	1.10
CLSC	WASRNDB-026-002	49.04	0.82	13.60	8.58	0.18	12.92	11.61	1.80	0.04	0.05	0.11	1.31	70	1364.73	1.20
CLSC	SSV0708-063-001-001	48.29	0.76	16.96	7.17	0.14	10.82	12.57	1.94	0.01	0.05	0.06	1.27	70	1310.82	1.05
CLSC	SSV0708-062-001-001	48.95	0.81	13.98	8.03	0.16	12.11	12.64	1.92	0.04	0.05	0.07	1.28	70	1345.61	1.11
ELSC	WASRNDB-005-008	49.98	0.79	13.22	8.35	0.16	12.58	11.68	1.72	0.04	0.05	0.21	1.28	70	1347.33	1.00
VFR	SO48/61GC	50.57	0.63	14.23	7.39	0.15	11.15	11.70	1.40	0.21	0.07	1.20	1.37	70	1282.91	0.76
VFR	SO35/84KD1	49.62	0.68	14.20	7.99	0.14	12.06	11.25	1.38	0.14	0.05	1.12	1.41	70	1311.38	0.95
VFR	SON0048-114	50.17	0.51	13.21	8.41	0.17	12.69	10.79	1.18	0.25	0.07	1.18	1.44	70	1322.86	0.94
VFR	SON0035-128	52.47	0.47	12.54	7.18	0.21	10.83	11.17	1.17	0.48	0.08	1.91	1.58	70	1252.86	0.55

[+] Primary compositions are calculated by incrementally adding equilibrium olivine until melt is in equilibrium with Fo90 (using the Fe3+/FeT given, and assuming KD=0.3).

[++] *T* and *P* are equilibrium temperature and pressure calculated using *Lee et al.* [2009] thermobarometer, assuming liquids in equilibrium with Fo90 mantle.

Chapter 3

Upper mantle structure of the Tonga-Lau-Fiji region from Rayleigh wave tomography

Abstract

We investigate the seismic structure of the upper mantle in the Tonga-Lau-Fiji region by jointly inverting the phase velocities of Rayleigh wave from the ambient-noise tomography and the two-plane-wave tomography, using seismic data from ocean bottom seismographs (OBSs) and land stations. 3-D tomographic results suggest a wide low-velocity zone, with a minimum *SV*-velocity of about 3.6 km/s, indicating upwelling hot asthenosphere with extensive partial melting beneath the Lau Basin. The variations of velocity anomalies along the spreading centers suggest the varying mantle porosity filled with melt, further implying a change in the efficiency of melt extraction due to water released from the slab. In the north where the spreading centers are distant from the Tonga slab, the inferred melting commences at about 70 km depth, and forms an inclined zone in the mantle, dipping to the west away from the arc, suggesting a passive decompression melting process supplied by the Australian mantle from the west. In the south, as the supply from the Australian mantle is impeded by the Lau Ridge lithosphere, the subduction-related flux melting dominates in the back-arc, which results in the rapid transition in

geochemistry and axial morphology along the Eastern Lau Spreading Center and the Valu Fa Ridge. The remnant Lau Ridge and the Fiji Plateau are characterized by a thick lithosphere and a hot asthenosphere. Our results suggest the removal of the lithosphere of the eastern Fiji Plateau and northern Lau Ridge, where the active Taveuni Volcano exists. This, along with the low-velocity anomalies beneath the northwestern Lau Basin, implies a second origin from the deep mantle in addition to the Samoan mantle plume. Azimuthal anisotropy shows that the mantle flow direction rotates from eastwards beneath Fiji to southwards beneath the Lau Basin, providing evidence for the southwards flow of the mantle wedge and the Samoan plume.

3.1. Introduction:

Back-arc spreading centers are usually compared with mid-ocean ridges (MORs) due to the similar mechanisms and contributions to the global plate tectonics. However, because of the significant influence of the adjacent subduction process, the back-arc spreading centers are obviously different from the MORs in geomorphological, geophysical, and geochemical perspectives [e.g. *Taylor et al.*, 1996; *Zhao et al.*, 1997; *Kelley et al.*, 2006]. The Lau back-arc basin and the adjacent areas are exemplary locations for understanding the interactions between the back-arc spreading and the subduction processes. While the Pacific Plate is subducting along the Tonga trench beneath the Australian Plate, new oceanic crust is generated at the back-arc spreading centers in the Lau Basin (Fig. 3.1).

The Lau back-arc started extending at about 6 Ma, then transitioned to seafloor spreading at about 4 Ma in the north [*Taylor et al.*, 1996]. This process propagated southwards and split the ancient Lau-Colville arc, which ceased its volcanic activities at about 5 Ma [*Parson and Wright*, 1996], into the Lau Ridge and Tonga Ridge, and formed the Lau back-arc basin with the active Tofua volcanic arc immediately to the west of the Tonga Ridge. Currently the total spreading rate of the ridges in the northern part of the Lau Basin is about 160 mm/yr, while the convergence rate at the trench also reaches a maximum of about 240 mm/yr in the north [*Bevis et al.*, 1995]. Therefore, the rigid Tonga Ridge is rotating clockwise, resulting in a larger distance from the spreading center to the trench in the north than in the south. This variation of distance from the back-arc spreading centers to the subducting slab presumably causes systematic variations in the geological features of the spreading centers [*Martinez and Taylor*, 2002]. The CLSC, 160-185 km away from the volcanic arc, is characterized by a normal crustal thickness of 6-7 km, shallow bathymetry, fast spreading rates of 85-95 mm/yr, and mid-ocean ridge basalt

(MORB)-like geochemical features. To the south, the ELSC is 60-110 km away from the arc, and has a thin crust, deep axial bathymetry, and intermediate spreading rates of 60-95 mm/yr. Lavas from the ELSC are strongly depleted compared to the MORB, and their arc geochemical signatures are weaker than that from the VFR. To the further south, the VFR, 40-60 km away from the arc, is characterized by a thick crust (7.5-9 km), shallow bathymetry, slower spreading rates of 40-60 mm/yr, and primarily arc-like compositions of rocks [*Pearce et al.*, 1994; *Turner et al.*, 1999; *Zellmer and Taylor*, 2001; *Martinez and Taylor*, 2002; *Crawford et al.*, 2003]. This distance-controlling hypothesis explains the along-strike variations resulting from increasing input of subduction-related materials southwards [*Martinez and Taylor*, 2002], though direct evidence from seismic imaging are needed.

More recent studies of geochemistry and geophysics in this region revealed additional complexities, in smaller scales, beyond the distance-controlling hypothesis. Geomorphological surveys indicated that the spreading center becomes flatter and more faulted when the spreading rate increases, which is opposite to the usual trend at MORs globally [*Martinez et al.*, 2006]. Although the distance from the spreading centers to the arc decreases southwards gradually, Mg # and trace element concentrations (e.g. Ba, Th, and La) of the lavas show abrupt transitions at latitudes of about 20.6˚S and 21.2˚S [*Escrig et al.*, 2009], coinciding with the transitions of the axial morphology from the northern ELSC to the central ELSC and the central ELSC to the VFR, respectively [*Martinez et al.*, 2006]. In addition, the crustal and mantle structure of the Fiji Plateau and the Lau Ridge are poorly known [e.g. *Dubois et al.*, 1973]. Although most geochemical evidence shows a signature of the Samoan plume in the northern Lau Basin [e.g. *Wendt et al.*, 1997; *Turner and Hawkesworth*, 1998], studies of the Fijian volcanoes and the back-arc spreading centers in the northwestern Lau Basin imply more complexities in terms of

mantle source materials [*Gill and Whelan*, 1989; *Lytle et al.*, 2012]. A detailed seismic model for the Fiji Plateau is essential to address these problems.

Previous passive seismological studies in this region mainly consist of the Southwest Pacific Seismic Experiment (SPASE) (November, 1993 to December, 1995) and the Lau Basin ocean-bottom seismograph survey (LABATTS) (September, 1994 to December, 1994). Body wave tomographic results showed a region with low seismic velocities [*Zhao et al.*, 1997; *Conder and Wiens*, 2006] and high attenuation [*Roth et al.*, 1999] in the uppermost mantle beneath the CLSC, and shifting westwards asymmetrically. Shear wave splitting results suggested that mantle flow is parallel to the convergence direction beneath the Fiji Plateau, and rotates perpendicular to the convergence direction with increasing proximity to the trench [*Smith et al.*, 2001]. However, since most of the seismic stations in these two experiments were deployed linearly across the Tonga Ridge, the CLSC and the Fiji Plateau, the previous studies were only able to demonstrate the variations of seismic properties along the E-W direction, but failed to show the complex 3-D patterns. Particularly, the changes along the spreading centers and the characteristics of the Fiji Plateau were not fully addressed.

The Ridge2000 Lau Spreading Center Imaging project in 2009-2010 provides high quality seismic data to help us better understand the N-S striking variations. 3-D active seismic surveys related the abrupt changes in geomorphology and geochemistry along the ELSC-VFR to a zoned structure with a rapid transition from a typical oceanic crust to an abnormally hydrous crust southwards, implying a dramatic increase in the influence of subduction as the spreading center moves closer to the arc [*Dunn and Martinez*, 2011; *Dunn et al.*, 2013; *Arai and Dunn*, 2014]. Ambient-noise tomography further supported this idea by directly imaging the connection between the back-arc and arc melting regions beneath the VFR [*Zha et al.*, 2014]. Moreover, the

Rayleigh wave tomography using teleseismic data emphasized the melt extraction rate, influenced by the water released from the slab, as one of the crucial factors in controlling the magmatism in the Lau Basin [*Wei et al.*, 2015].

Although *Zha et al.* [2014] and *Wei et al.* [2015] inverted for the *S*-wave velocity structures of the Lau Basin from ambient-noise tomography (ANT) at short periods and teleseismic Rayleigh waves with two-plane-wave tomography [*Forsyth and Li*, 2005; *Yang and Forsyth*, 2006] (TPWT) at long periods, respectively, no study has investigated the entire dispersion curves over all periods. Both methods provide structural information in complimentary period bands: ANT inverts phase velocities at periods from 8 to 18 s, most sensitive to depths of about 10-25 km, whereas TPWT inverts those from 23 to 88 s, most sensitive to depths of about 30-140 km. Inverting the entire dispersion curve can greatly improving the resolutions at depths of 25-35 km, where the interactions between the arc and back-arc magmatism are expected to be intense. Additionally, the structures of the Lau Ridge, Fiji Plateau, and the Tofua arc have not been investigated in detail. Therefore, in this study, we first present new results of azimuthal anisotropy of Rayleigh waves and *S*-wave velocities by jointly inverting from phase velocities of ANT and TPWT. In the light of our *S*-wave velocity structure as well as previous studies, we try to construct a comprehensive model of the upper mantle for Tonga, Lau, Fiji, and the adjacent regions.

3.2. Data and Methods

3.2.1 Data collection

Most of the data used in the phase-velocity inversion was collected from 49 OBSs deployed

from November 2009 to November 2010 (red and black dots in Fig. 3.2), and 17 island-based seismic stations operated from October 2009 to December 2010 (red triangles in Fig. 3.2). The OBS array consisted of two main profiles extending across the ELSC to the active Tofua arc, one profile along the ELSC between the two main profiles, and several sparsely distributed sites. Each OBS from Woods Hole Oceanographic Institution (WHOI) contains a Guralp CMG3T seismometer and a Quanterra Q330 datalogger, while other OBSs from Lamont-Doherty Earth Observatory (LDEO) use Sercel (formerly Mark Products) L-4C seismometers and LDEO-designed dataloggers. The land stations were deployed over islands of Tonga and Fiji. Each of them contains a broadband three-component seismometer (Guralp CMG3T, Streckeisen STS-2, or Nanometrics Trillium 120PA) and a Reftek 130-01 recorder. We additionally used data from 14 OBSs of the LABATTS experiment and 9 island-based stations of the SPASE project collected from September to December 1994 for the TPWT.

3.2.2 Phase-velocity inversion: ambient noise cross-correlation

The ANT was conducted in a similar way as *Zha et al.* [2014] using a frequency-domain method [*Ekström et al.*, 2009], but we additionally included the data from land stations in this study. The daily seismograms recorded by vertical channels were first quality-controlled, corrected for clock drift and instrument responses, downsampled to 5 sps, cut into 100 overlapping windows, and then Fourier-transformed to the frequency domain. A cross-correlation spectrum between each station pair was normalized by the spectral amplitudes, averaged over all windows in a day, and stacked over all days. This frequency-domain normalization for each short time window effectively removes the effects of large earthquakes.

We calculated phase velocities using the zero-crossing of the averaged cross-correlation

spectra to generate a suite of possible dispersion curves [*Ekström et al.*, 2009]. In order to extract the most reasonable dispersion curve, we adopted previous results for the crustal structure [*Crawford et al.*, 2003] and a *Vp/Vs* ratio of 1.85 [*Conder and Wiens*, 2006] as a reference model. We discarded dispersion curves between stations that have bathymetry differences greater than 1 km, and the average water depth between the stations were adopted into the reference model. All dispersion curves were manually examined to exclude those with physically unreasonable values.

752 dispersion curves were used for the phase-velocity inversion with a grid of node spacing 0.2˚. The finite-frequency sensitivity kernels were calculated using the method of *Yoshizawa and Kennett* [2002] and the Pacific Ocean model by *Nishimura and Forsyth* [1989] (henceforth the NF89 model) for 0-4 Myr lithospheric age as the starting model. The tomographic inversion inverts for both isotropic and azimuthally anisotropic components of the Rayleigh wave phase velocity. However, robust results of anisotropy can be only resolved in a small region where most OBSs are concentrated, which has been discussed by *Menke et al.* [2015] along with the results of *S*-wave splitting. Therefore, the anisotropic components of the ANT results were not included in the rest of data processing and discussions. Since the quality of data from OBSs is restricted in a narrow frequency band, we were only able to get robust phase velocities at periods from 8 to 18 s. Readers are referred to *Zha et al.* [2014] for more technical details.

3.2.3 Phase-velocity inversion: two-plane wave method for teleseismic data

Following *Wei et al.* [2015], we selected seismograms of 357 earthquakes with surface-wave magnitudes (Ms) larger than 4.5 and epicentral distances between 30º and 150º, which occurred during the time when stations were operating (inset of Fig. 3.2). Prior to the tomographic

inversion, data were down-sampled to 1 sps and instrument responses were removed. For each period of interest from 19 to 88 s, we used a narrow bandpass filter (4th order Butterworth, zero-phase shift) centered at the frequency of interest to filter the seismograms. The filtered data were then windowed manually to isolate the fundamental mode of the Rayleigh wave. Noise in seismograms at long periods (> 50 s) due to ocean swell and associated water pressure variations, as well as tilt caused by local currents, was removed by correcting the vertical channel using the horizontal and pressure channels [*Webb and Crawford*, 1999; *Crawford and Webb*, 2000; *Bell et al.*, 2015].

We then applied the two-plane-wave analysis method [*Forsyth and Li*, 2005] with 2-D Fréchet kernels [*Yang and Forsyth*, 2006] to invert phase velocity at each period with isotropic and anisotropic components. The advantages of this method include (1) addressing wavefront effects of global heterogeneities outside of the study region with the two-plane-wave approximation, (2) correcting the effects of scattering and multipathing within the inversion region with the 2-D finite-frequency Fréchet kernels, (3) computational efficiency, and (4) being able to combine two datasets over different time periods (1994 and 2009-2010) to expand the resolving region.

In order to take account of azimuthal anisotropy, the study region was divided into four subregions according to the tectonic setting: Lau Basin, Fiji Plateau-Lau Ridge, Tonga Ridge and background, and the average anisotropy of each subregion is included in the inversion. We then conducted a series of TPWT phase-velocity inversions with progressively finer grids (extending down to 58.7 km spacing) and smaller smoothing length (ending at 50-80 km depending on the period). Such a strategy can largely eliminate the dependence on the starting model and the *a priori* information [*Rau and Forsyth*, 2011]. More details of the TPWT phase-velocity inversions

are discussed by *Wei et al.* [2015]. Both azimuthally isotropic and anisotropic components of the phase velocity were solved simultaneously, but only the isotropic phase velocities were used for the *SV*-velocity inversion.

3.2.4 Combining dispersion curves

Combining ANT and TPWT provides more complete measurements of phase velocity for the next step of the *SV*-velocity inversion. However, as these two methods are based on different principles and assumptions, the results of phase velocity at the common periods from two methods are usually not identical [*Yao et al.*, 2006]. In this study, we were not able to resolve the results of ANT and TPWT at a common period because of the high noise level of the OBS data. The data around the period of 20 s had too much seafloor noise from other sources to obtain good results with ANT, and 20 s is at the shortest period end for realistic application of TPWT. Fig. 3.3 shows that the resulting phase velocities agree well at the adjacent periods, although small-scale discrepancies still exist. A further investigation that compares the TPWT with Eikonal and Helmholtz tomography of the OBS data [*Lin et al.*, 2009; *Lin and Ritzwoller*, 2011; *Jin and Gaherty*, 2015] suggests that the real uncertainties of phase velocities are as large as 0.2 km/s at periods of 19 and 21 s for such geometry of the seismic array, significantly larger than the standard deviation given by the TPWT inversion (< 0.1 km/s). Since the Eikonal and Helmholtz tomography require regularly distributed stations deployed over the same time, which largely limit the usability of our data and the resolving region, we use the phase velocities from the TPWT but amplified the uncertainties according to the comparisons with the Helmholtz tomography.

The two sets of dispersion curves were combined in the geographical region well resolved by

both methods (blue outline in Fig. 3.3a) for the *SV*-velocity inversion. The phase velocities were interpolated onto a uniform grid of nodes spacing 0.2˚ before being combined at each node (Figs. 3.4a and 3.4b). The phase velocities at periods of 19 and 21 s were discarded due to the large uncertainties, and the uncertainties at other periods were amplified following the rule that at each period, the minimum uncertainty was amplified to a reference value and uncertainties of other nodes were amplified in the same scale. According to previous experience [*Yang et al.*, 2008; *Shen et al.*, 2013] and the comparison between Helmholtz tomography and the TPWT mentioned above, the reference uncertainty is assigned as 0.2 km/s for periods of 18-23 s, 0.15 km/s for periods of 16, 17, 25.6, and 28.2 s, and 0.1 km/s for other periods. A modified running average filter was applied so that the resulting dispersion curve is smoother but the phase velocity at each period can be adjusted only within the uncertainties. In the outer regions where no ANT results were available, we used phase velocities from the TPWT at all periods to invert for *SV*-velocity (Fig. 3.6c), and the resolving boundary (black polygon in Fig. 3.5a) was defined as *Wei et al.* [2015].

It is worthwhile to examine the noticeable depression of the dispersion curve at certain nodes. This depression can be observed solely by TPWT (Fig. 3.4c) or by combining ANT and TPWT (Fig. 3.4a), and has been previously observed at the East Pacific Rise [*Forsyth et al.*, 1998]. Therefore, we conclude that the depression of the dispersion curve convincingly reflects a strong low-velocity zone (LVZ) beneath a very thin lithosphere.

3.2.5 *SV*-wave-velocity inversion with a Bayesian Monte-Carlo algorithm

Previous studies [e.g. *Wei et al.*, 2015] suggest that the linearized inversion of *SV*-velocity from phase velocity dispersion curves [*Herrmann*, 2004] depends upon the starting model. In

order to avoid the potential biases due to the starting model, we applied a Bayesian Monte-Carlo method [*Shen et al.*, 2012] to invert for the *SV*-wave velocity at each node.

The Bayesian Monte-Carlo method constructs a prior distribution of *SV*-velocity models at each node defined by perturbations relative to the starting model and models constraints. The posterior distribution thus provides statistical information of all possible *SV*-velocity models that satisfy the Rayleigh wave dispersion data within tolerances depending on data uncertainties. Each model consists 6 layers: (1) water with fixed thickness from a topography/bathymetry model by *Lindquist et al.* [2004]; (2) sediments with a thickness of 500 ± 500 m and a fixed V_{SV} of 2 km/s; (3) crust with V_{SV} linearly increasing from 3.4 ± 0.3 km/s at the top to 3.8 ± 0.3 km/s at the bottom, and a thickness of 7 ± 3 km for nodes in oceanic crust, 25 ± 7 km for nodes on the ridges, or intermediate values for nodes in the transition region according to a previous seismic refraction survey [*Crawford et al.*, 2003]; (4) uppermost mantle from the Moho to a LVZ with a thickness of 35 ± 20 km and V_{SV} characterized by a B-spline perturbing ± 15%; (5) a LVZ with a thickness of 10 ± 7 km and a constant V_{SV} with a perturbation of ± 15%; (6) mantle beneath the LVZ with a fixed thickness of 150 km and V_{SV} characterized by a B-spline perturbing ± 10%. The 4th to 6th layers were designed to capture the strong LVZ suggested by the dispersion curves. We also applied a physical dispersion correction [*Kanamori and Anderson*, 1977] using a 1-D *Q* model simplified from a seismic attenuation study in the same region (Chapter 4).

Examples of the *SV*-velocity inversion at certain nodes are shown in Fig. 3.6. The results of the Bayesian Monte-Carlo inversion fit the measured dispersion curves as well as the linearized inversion. But this technique significantly reduces the dependence on the starting model and, more importantly, eliminates the artificial vibrations that induce low velocities beneath the high velocities, or vice versa (Fig. 3.4h).

3.3. Results

3.3.1 Azimuthally averaged phase velocity

Fig. 3.5 shows 2-D maps of azimuthally averaged phase velocities at representative periods from the ANT and TPWT. Since the ANT inverts waveform cross-correlations among stations, the resolving region is confined in a smaller area and varies slightly at different periods. The TPWT provides results encompassing larger areas, because it has some limited resolution outside the array and because we included data from the 1994 deployment. Because of the varying wavelengths of Rayleigh waves, the resolution length of the ANT is as small as 50 km at shortest periods, whereas the TPWT has larger resolving lengths (Fig. 3.6). As discussed in Section 3.2.4, the L_2 norm of the model actually underestimates the phase-velocity uncertainties. We thus amplify the errors according to previous experience (Figs. 3.4a-c).

3.3.2 Azimuthal anisotropy of phase velocity

Seismic azimuthal anisotropies were resolved simultaneously with the isotropic phase velocities by the TPWT. Since the Rayleigh waves sample large areas, we divided the study region into 4 tectonic subregions: the Lau Basin, the Fiji Plateau/Lau Ridge, the Tonga Ridge, and the surrounding region, and then inverted for an average anisotropy of each subregion (Fig. 3.7a). This method is best for regions with similar dimensions in each direction and worse for elongated ones. We thus only interpret the results for the Lau Basin and the Fiji Plateau-Lau Ridge (Figs. 3.7b and 3.7c). The magnitude of anisotropy varies depending upon the chosen

parameters of the tomographic inversion such as smoothing length and damping coefficient, but the fast directions are robust. We thus confine our interpretation to the directions of anisotropy.

3.3.3 Azimuthally averaged *SV*-velocity

Fig. 3.5b shows the misfit of the Bayesian Monte-Carlo inversion at each node. The inversion results at most of nodes are well constrained, except 7 nodes with large misfits, which are excluded for further discussion. The average models from the Monte-Carlo inversion are shown in Figs. 3.8 and 3.9 to represent the azimuthally averaged *SV*-velocity structure beneath the Tonga-Lau-Fiji region.

Thanks to the high resolution of the ANT phase velocity maps at short periods, small-scale features are well resolved at shallow depths within the region of the ANT-TPWT joint inversion. But this resolution contrast also introduces artificial discontinuous features at the boundary of the joint-inversion region. For instance, low-velocity anomalies are imaged at the depth of 20 km beneath the LETZ in Fig. 3.7, but artificially stop at the northern boundary of the joint-inversion region (white contour) instead of extending southwards to the CLSC. We believe that the velocities within the white contour are more convincing, and thus hesitate to over interpret any of the shallow features along this boundary.

The most obvious feature in our results is the contrast between the Lau Basin and the remnant arcs. The Tonga Ridge, Fiji Plateau, and Lau Ridge are characterized by low velocities at depths shallower than 30 km and by high velocities at depths of 30-50 km, indicating the crust and mantle lithosphere respectively. In contrast, a *V*-shaped low-velocity zone (LVZ) has been imaged in the uppermost mantle of the Lau Basin, forming an asymmetric triangular region beneath the back-arc spreading centers. While the depth increases to about 100 km, all these

features fade away, leaving the subducting slab with high velocities as the dominant structure.

3.4. Discussion

3.4.1 Factors controlling seismic velocity

Interpreting seismic observations always results in non-unique solutions since many factors can influence seismic velocity. In order to study the distribution of melt, it is necessary to distinguish the effects of melt from other effects before discussing the implications. Generally speaking, seismic properties of mantle rocks are controlled by temperature, composition, grain size, and melt/free fluid through anharmonic and anelastic behaviors.

Thermal variations affect seismic properties in both anharmonic and anelastic ways. For high frequency seismic waves, a reduction in density due to thermal expansion (anharmonic oscillation) results in reductions in elastic moduli and thus seismic velocity [*Anderson*, 2007]. However in the seismically observable frequency band (0.01-1 Hz), anelasticity can be equivalently important as seismic attenuation also affects seismic velocity [*Karato*, 1993]. The effects of temperature on anharmonic and anelastic behaviors are revealed by experiments of rock deformation [e.g. *Isaak*, 1992; *Faul and Jackson*, 2005; *Jackson and Faul*, 2010]. Seismological and geochemical comparisons among different back-arc basins suggest that temperature plays a dominant role in the back-arc system [*Wiens et al.*, 2006].

Compositional variations of mantle rocks have been considered unimportant to the variations observed in seismic results because the shear modulus is increased by the depletion of FeO in olivine but also reduced by the depletion of Al_2O_3 [*Faul and Jackson*, 2005]. However, studies on natural peridotite [*Lee*, 2003; *Schutt and Lesher*, 2010] indicate that melt depletion leads to an

increase of about 0.7% in *S*-wave velocity, much smaller than regional velocity variations (> 10%) observed in our results.

Structurally bound water is thought to reduce seismic velocity through by increasing anelasticity [*Karato*, 2003]. However, since water also enhances grain growth and this has the opposite effect on anelasticity, this competing effect may eliminate the effects of water on seismic properties [*Abers et al.*, 2014]. In contrast to the relatively dry MORs with the water concentrations of 0.01-0.05 wt % in the mantle source, the CLSC and ELSC lie on the upper bound of the MOR regime with the water content of 0.04-0.06 wt %, and the VFR is characterized with significantly larger water content of 0.22 wt % [*Kelley et al.*, 2006]. In addition, since the water concentrations in many regions beneath the Lau Basin exceed the minimum storage capacity of nominally anhydrous mantle minerals [*Kelley et al.*, 2006], a certain amount of free water may exist in the mantle wedge. Therefore, the effects of water content to the seismic velocity could be significant, thus have to be taken into account. On the other hand, high water content facilitates partial melting by reducing rock melting point, thus it is difficult to distinguish the effect of water from temperature and melt. Along the Lau spreading centers, the magnitude of slow anomaly increases from south to north (Fig. 3.8), opposite to the trend of decreasing water content [*Kelley et al.*, 2006], implying that the structurally bound water content is not the predominant factor controlling the seismic velocity. The mantle water content is also higher near the slab, whereas the largest seismic anomalies occur beneath the back-arc spreading center, again suggesting that the observed slow velocity anomalies do not result directly from mantle water.

Melt/fluid (such as free water) introduces more complex effects on seismic velocity. It is generally accepted that partial melting decreases the anharmonic shear modulus of the rocks and

the reduction of the *S*-wave velocity highly depends on melt geometry [e.g. *Hammond and Humphreys*, 2000a; *Takei*, 2002]. However, the effects of partial melting on seismic attenuation and consequently seismic velocity through anelastic behavior have not been well constrained. *Hammond and Humphreys* [2000b] did not observe melt-related attenuation in the seismic band in numerical calculations while *Jackson et al.* [2004] claimed that melt influences seismic attenuation through grain-boundary sliding based on experiments. On the other hand, partial melting may dehydrate residual mantle rocks [*Hirth and Kohlstedt*, 1996], causing a decrease in seismic attenuation and an increase in seismic velocity due to a reduction in anelasticity. The latter effect also depends upon the water supply. Geochemical studies reveal a positive correlation between the water concentration of the mantle and the extent of melting beneath the back-arc spreading centers [*Kelley et al.*, 2006], in contrast to a negative correlation beneath the MORs [*Asimow and Langmuir*, 2003].

Following *Wei et al.* [2015], we converted recent 2-D numerical models of mantle wedge flow by *Harmon and Blackman* [2010] to *SV*-velocities in order to visualize the potential effects of temperature and water on seismic velocity. Such conversion is based on available rock physical models and experimental constraints, including an extended Burgers model that fits data of forced torsional oscillation experiments [*Jackson and Faul*, 2010] and the effects of bound water on seismic velocity as proposed by *Karato* [2012]. The calculated isotropic *S*-wave velocities are converted to *SV*-velocities for comparison with the results from this study using the radial anisotropy as a function of depth from the NF89 0-4 Myr model [*Nishimura and Forsyth*, 1989]. Since the potential temperature used in the numerical models is 1450 ˚C [*Harmon and Blackman*, 2010], consistent with the value revealed at the CLSC but slightly higher than that at the ELSC and VFR [*Wei et al.*, 2015], and the exponent constant of water effects *r* lies on the

upper limit [*Karato*, 2012], the predicted values in Fig. 3.9 should provide a lower bounds for *SV*-velocity. We acknowledge that several parameters of the models are poorly constrained, and other models [e.g. *Goes et al.*, 2012] may produce a predicted model of *SV*-velocity slightly closer to our observations. But none of these models can explain the low velocities solely by variations of temperature and water content. Therefore, it is reasonable to attribute the extremely low *SV*-velocities to partial melting, though calculating the mantle porosity filled with melt (melt porosity hereafter) is beyond current knowledge of rock physics [*Faul and Jackson*, 2015].

In summary, the large-scale contrast of the subducting slab with fast seismic velocities versus the spreading centers with slow seismic velocities is interpreted as being thermally controlled. Water incorporated in the mineral structure further reduces the *S*-wave velocity. Basaltic melt with variable water content, which significantly decreases seismic velocity in the melting region, provides a good explanation for the very low velocity anomalies observed in the Lau Basin beneath the spreading centers and volcanic arc.

3.4.2 CLSC-ELSC-VFR, Tofua arc, and Tonga Ridge

At shallow depths (20 km in Fig. 3.7), the low-velocity anomalies correlate well with topography, showing the contrast between the thicker arc crust and the thin oceanic crust. Although we are not able to resolve the Moho precisely without constraints of converted seismic waves (e.g. receiver functions), it is reasonable to conclude that the crustal thickness is about 25 km beneath the Tonga Ridge and less than 10 km in the Lau Basin. The back-arc spreading centers are also characterized by low-velocity anomalies, indicating melt in the upper mantle.

At greater depths, an LVZ encompasses an N-S striking broad region beneath the Lau Basin. Since these depths are convincingly below the lithosphere-asthenosphere boundary (LAB)

predicted by a simple half-space cooling model [*Wei et al.*, 2015], this *V*-shaped LVZ illustrates a contrast between the hot asthenosphere of the Lau Basin and the cold and thicker lithosphere of the Tonga and Lau ridges. Cross-sections (Fig. 3.8) show this LVZ becoming deeper with distance away from the arc, indicative of a broad and asymmetric hot region beneath the back-arc basin. As discussed in the previous sections, the widespread low velocity in the mantle indicates high temperature, while the extremely slow anomalies at depths of 30-70 km beneath the arc and spreading center represent high melt porosity in the mantle wedge. So the inclined LVZ implies that hot materials upwell from the deep west governed by the mantle wedge corner flow [*Conder et al.*, 2002], triggering extensive passive decompression melting, similar to the asymmetric melting region beneath the East Pacific Rise (EPR) [*Forsyth et al.*, 1998; *The MELT Seismic Team*, 1998]. The onset of melt appears to occur at depths of 70-80 km west of the spreading centers (Fig. 3.8), consistent with petrological expectations [*Shen and Forsyth*, 1995]. The off-axis melt may percolate towards to spreading centers along the bottom of the thermal/compositional lithosphere driven by the focusing effects [*Sparks and Parmentier*, 1993; *Phipps Morgan*, 1997]. On the other hand, off-ridge volcanism in the Lau Basin [*Falloon et al.*, 1992] may be also related to these melts.

The *V*-shaped LVZ can be explained by the opening of the back-arc basin, since the hot asthenosphere is wider in the north than in the south. However, this mechanism cannot explain the small-scale variations of the extreme-low-velocity anomalies along the spreading centers, as the along-strike thermal variation is only about 50 ˚C, potentially resulting in a slight change in velocity of 0.1 km/s [*Wei et al.*, 2015]. Therefore, we attribute these along-strike variations to changes in melt porosity. Our results suggest the melt porosity is highest beneath the northeastern Lau Basin and the CLSC, and decreases southwards to the VFR. Additionally, the

melting commences deeper in the north, and becomes shallower in the south. However, higher melt production and deeper onset of melting are expected in the south due to the higher mantle water content there according to previous numerical models [*Harmon and Blackman*, 2010], petrological studies [*Kelley et al.*, 2006], and surveys of crustal structure [*Dunn and Martinez*, 2011], opposite to our inferences. These discrepancies imply that the efficiency of melt extraction varies along the spreading centers, due to the water released from the slab or the existence of a nearby spreading center [*Wei et al.*, 2015]. At the VFR, an enormous amount of water from the slab enters the back-arc melting region, which reduces melt viscosity and/or increases mantle grain size, and further enhancing the upward melt transport by porous flow extraction and reducing melt porosity. At the CLSC, the mantle water content drops to the regime of MORB [*Kelley et al.*, 2006], so water has little effect on melt extraction. The large melt production and rapid upwelling rate of the matrix help the mantle to retain the partial melt. At the northeastern Lau Basin, between the CLSC and the FRSC, a melts generated in the mantle wedge are trapped in the mantle because of the lack of an effective magma channel, either slowly solidifying or migrating laterally in large distances to one of the spreading centers.

The combination of the ANT and the TPWT greatly strengthen our capability of studying the interactions between the arc and back-arc melting. The arc is presumably dominated by flux melting whereas the back-arc is dominated by decompression melting. The cross-sections B-B' and C-C' (Fig. 3.9) show that in the north where the CLSC and ELCS are distant from the volcanic arc, two melting regions are separated in the uppermost mantle but connect at greater depths. This is also observed in the Mariana Island Arc, where the back-arc spreading center is located more than 100 km away from the volcanic arc [*Barklage et al.*, 2015]. In the south as the VFR is closer to the arc, two melting regions with different mechanisms interact at all depths.

These observations provide the direct seismic evidence for the distance-controlling hypothesis, that the interactions between the arc and back-arc melting predominantly determine the along-strike variations of geology, petrology, and geomorphology [*Martinez and Taylor*, 2002]. Due to the low lateral resolution of Rayleigh wave tomography, it is difficult to resolve the details of flux melting, especially the dehydration of the slab and the hydration of the mantle wedge. However, the high-velocity anomalies corresponding to the slab show a gap at the depths of 50-100 km, potentially illustrating these reactions. The slow anomalies are generally weaker beneath the Tofua volcanic arc than that in the back-arc. This could partially result from the strong depletion at the arc, but also imply that the melt porosity beneath the arc is significantly lower than that in the back-arc. The more water-riched arc magma segregates and erupts more efficiently compared to the back-arc magma that lies in the MOR regime of low water content [*Kelley et al.*, 2006].

Comparisons among cross-sections also reveal the cause of the abrupt change in geochemical signatures and axial morphology along the ELSC-VFR at about 20.6˚S and 21.2˚S [*Bézos et al.*, 2009; *Escrig et al.*, 2009]. The cross-sections B-B' and C-C' (Fig. 3.9) suggest that the major sources of mantle materials of the CLSC and ELSC are the Australian mantle from the west with a small contribution from the slab-influenced mantle wedge. In contrast, the LVZ beneath the VFR appears to be disconnected to the west, implying that the supply of mantle materials from the Australian asthenosphere is impeded by the thick lithosphere of the Lau Ridge. On the other hand, the influence of subduction increases consistently to become the dominant material source at the VFR. We propose that the sudden transition in magma chemistry at about 20.6˚S and 21.2˚S represents the transition between spreading centers fed by Australian mantle from the west and those restricted to melts generated near the Tonga slab. In other words, this abrupt

transition not only reflects a gradual change in the influence from subduction, but also another gradual change in the influence from the Australian mantle in an opposite trend. We also notice that these variations of seismic velocity structure coincide with a transition in the extinct Lau Ridge between uplifted section to the north and the submerged section to the south. Our inferences suggest that the uplifted section to the north corresponds to areas underlain by rising warm mantle capable of providing buoyancy, and the southern section lacking such mantle structure.

3.4.3 Fiji Plateau and Lau Ridge

Figs. 3.8 and 3.9 suggest the crustal thickness of the Fiji Plateau-Lau Ridge is about 25-30 km. The high-velocity anomalies in the mantle are indicative of cold lithosphere of this ancient arc with a thickness of 70-80 km. The asthenosphere is characterized by a thick LVZ with *SV*-velocity of 4.1-4.3 km/s, consistent with previous observations [*Dubois et al.*, 1973] as well as the typical *SV*-velocity for young oceanic asthenosphere given by *Nishimura and Forsyth* [1989]. The slow velocities in the LVZ can be explained by thermal variations without any significant existence of melt, although the role of small amounts of partial melt in the asthenosphere generally is a subject of considerable debate [e.g. *Goes et al.*, 2012; *Holtzman*, 2016].

One intriguing feature is a slow anomaly at the depths of 50-60 km beneath the active Taveuni Volcano and the northernmost Lau islands, which connects to the broad *V*-shaped LVZ in the central Lau Basin. This suggests the removal of the lithosphere of the eastern Fiji Plateau and the northern Lau Ridge. Although this anomaly appears to be an arm extending from the *V*-shaped LVZ beneath the Lau Basin, isotopic studies reveal that the magma from the Taveuni Volcano has similar origin with the Samoa mantle plume rather than the Lau spreading centers

[*Pearce et al.*, 2007]. Additionally, analyses of trace elements suggested that the magmatism rejuvenated since 3 Ma with a strong signal of ocean-island basalt (OIB) [*Gill and Whelan*, 1989]. Therefore, one reasonable explanation is that hot materials from deep mantle, perhaps related to the Samoa mantle plume, upwell and erode the lithosphere beneath the Taveuni Volcano, although the mechanism of removing the lithosphere is unclear.

3.4.4 Northern Lau Basin

Although it is widely accepted that material from the Samoan mantle plume enters into the Tonga mantle wedge from north [*Turner and Hawkesworth*, 1998; *Pearce et al.*, 2007], the details of this process, especially beneath the northern Lau Basin, are unclear. There are two series of back-arc spreading centers in this region: the eastern series consisting of the Fonualei Rift and Spreading Center (FRSC) and the Mangatolu Triple Junction (MTJ) close to the Tonga trench, and the western series including the Lau Extensional Transform Zone (LETZ), the Peggy Ridge (PR), and the Northwest Lau Spreading Center (NWLSC). Recent isotopic geochemical analyses of rock samples collected from these two series reveal heterogeneities across the northern Lau Basin. In the west along the NWLSC-PR-LETZ, the diversity of geochemical signatures suggest that the magma originates from more than two mantle sources, including the Samoan mantle plume, a shallow MORB-like source beneath the spreading centers, and a possible second plume from deep west [*Lytle et al.*, 2012]. In the east along the MTJ-FRSC, the lavas are dominated by flux melting resembling those at the VFR but with a strong signature of the Samoan plume [*Caulfield et al.*, 2012].

Figs. 3.8 and 3.9 show two distinct LVZs at the depth of 20-30 km beneath the MTJ-FRSC and the NWLSC-PR-LETZ, respectively, but connecting and forming a broader LVZ at the

depths below 40 km. These results suggest that hot materials of the Samoan plume enter into the Tonga mantle wedge within a broad flow, supplying both series of spreading centers. But as the mantle rises, the hot materials are confined along the spreading centers due to the focusing effect of the ridges. Unlike the similar feature observed at the CLSC (cross-section A-A'), the connection of the LVZ at the depths below 40 km does not imply much interaction between the melting processes beneath two series of spreading centers, since no geochemical signature of subduction is found at the NWLSC-PR-LETZ. This can explain the existence of partial melt trapped beneath the northeastern Lau Basin, as the lateral material exchange is inactive across such a long distance from the MTJ-FRSC to the NWLSC-PR-LETZ. In addition, the cross-section E-E' (Fig. 3.9) shows a connection between the PR and the removal of Fijian lithosphere. Given the fact that the OIB signatures have been observed in both locations [*Gill and Whelan*, 1989; *Lytle et al.*, 2012], this connection potentially reveals a mutual origin of the lavas at the NWLSC-PR-LETZ and northeastern Fiji.

3.4.5 Mantle flow: indicated by the seismic anisotropy

The azimuthal anisotropy results (Figs. 3.7 and 3.11) suggest that the mantle anisotropy beneath the Lau Basin changes its fast direction from spreading-parallel (largely E-W) at periods shorter than 30 s to trench-parallel (mostly N-S) at longer periods, before becoming statistically unresolvable at the longest periods. These observations differ somewhat from previous studies of *S*-wave splitting and the ANT that consistently show trench-parallel anisotropy in the Lau Basin [*Smith et al.*, 2001; *Menke et al.*, 2015]. However, the *S*-wave splitting analysis only measures the accumulated anisotropy along all depths, so would be unable to resolve changes with depth. The ANT in *Menke et al.* [2015] was confined in a small area near the ELSC, where the 4-Myr

old [*Taylor et al.*, 1996] oceanic lithosphere is expected to be less than 20-km thick. Given the sensitivity kernels of Rayleigh waves, the trench-parallel anisotropy shown in *Menke et al.* [2015] may represent the mantle flow in the uppermost asthenosphere near the spreading center.

In contrast, our results (Fig. 3.7b and Fig. 3.11) show the spreading-parallel anisotropy at shorter periods, reflecting the shear strain parallel to the spreading direction frozen in the newborn oceanic lithosphere (about 40-km thick in average), resembling the East Pacific Rise [*Forsyth et al.*, 1998]. Trench-parallel anisotropy is observed at longer periods, indicating the underlying mantle flow parallel to the trench. The fast direction changes at the period of 31 s, while the corresponding Rayleigh waves are most sensitive to the depths of 40-50 km. These transition depths roughly coincide with the depths where large melt porosity exists, probably implying that the decoupling between the lithosphere and asthenosphere is facilitated by partial melt.

It is worthwhile to notice that the fast directions beneath the lithosphere are not perfectly aligned with the expected directions of mantle flow. Beneath the Fiji Plateau-Lau Ridge, the fast direction appears to be E-W striking with an oblique angle of about 15˚ with respect to the subduction direction. This may reflect the fact the corner flow of the mantle wedge is not exactly perpendicular to the trench as the subduction rate and the rate of slab roll-back are faster in the north than that in the south [*Bevis et al.*, 1995]. Beneath the Lau Basin, although the fast axis of mantle rocks show an N-S strike with an oblique angle of about 15˚ with respect to the trench. One possible explanation is that the observed fast direction reflects a combined flow pattern including the along-strike southwards flow of the Samoan plume (striking 195˚ from north) superposed by the mantle wedge corner flow away from the slab (striking 270˚ from north). An alternative explanation is that our observation implies a complex history of deformation [*Boneh*

and Skemer, 2014; *Boneh et al.*, 2015], that even if the mantle flow has been rotated from E-W striking to trench-parallel (striking 195˚ from north), the rotation of the fast axis of crystallographic preferred orientation (CPO) is lagged to striking 180˚ from north.

Beneath the Fiji Plateau-Lau Ridge, the fast directions at periods shorter than 40 s presumably indicate the anisotropy formed when the arc was active and later frozen in the lithosphere. The fast directions appear more complex, possibly because the Fijian islands rotated counterclockwise by about 90˚ since 6.8 Ma [*Malahoff et al.*, 1982]. Many fore-arcs and arcs show along strike fast directions that may result from horizontal compression. However, anisotropy at longer periods consistently strikes E-W, suggesting a mantle flow perpendicular to the trench which is consistent with previous studies of *S*-wave splitting [*Smith et al.*, 2001] and geodynamic expectations [*Harmon and Blackman*, 2010].

3.5. Conclusions

We obtained a comprehensive structure of *SV*-velocity for the Tonga-Lau-Fiji region by jointly inverting the Rayleigh wave phase velocities from the ANT and the TPWT with a Bayesian Monte-Carlo method [*Shen et al.*, 2012]. Our results suggest a thin crust (about 7 km thick) and lithosphere of the Lau Basin in contrast to the 25-35 km-thick crust and 40-50 km-thick lithosphere beneath the Tonga Ridge and the Fiji Plateau-Lau Ridge. A broad LVZ is imaged in the uppermost mantle beneath the Lau Basin, indicative of hot materials upwelling from the Australian mantle in the west. Additionally, extremely low-velocity anomalies exist beneath the Lau Basin at the depths of 20-80 km, suggesting partial melting mainly commences at 70-80 km depth. The broadly distributed melting region, along with the asymmetric mantle

upwelling, proves that decompression melting is the dominant melting process in the back-arc.

More detailed investigations on the variations of the seismic low velocities along the spreading centers suggest that the water released from the slab significantly facilitate the melt transport and extraction at the VFR where the spreading center is much closer to the Tofua volcanic arc compared to the CLSC and ELSC in the north. The abrupt changes in geochemistry and geomorphology at about 20.6˚S and 21.2˚S along the ELSC-VFR result from a transition of the dominating source of mantle materials. The magmas at the CLSC and ELSC are predominantly supplied by the Australian mantle from the west, while the materials at the VFR mainly come from the subduction-related mantle wedge from the east.

The lithosphere of the northeastern Fiji Plateau and north Lau Ridge appears to be removed by a hot spot from deep mantle, which may also contribute to the spreading centers in the northwestern Lau Basin. The MTJ and FRSC are dominated by flux melting similar to the VFR. All these spreading centers in the northern Lau Basin are significantly influenced by the Samoan mantle plume originating from deep north. This is also supported by our results of azimuthal anisotropy, which suggest that the mantle flow direction changes from eastwards beneath the Fiji Plateau to southwards beneath the Lau Basin.

References

Abers, G. A., K. M. Fischer, G. Hirth, D. A. Wiens, T. Plank, B. K. Holtzman, C. McCarthy, and E. Gazel (2014), Reconciling mantle attenuation-temperature relationships from seismology, petrology, and laboratory measurements, *Geochem. Geophys. Geosyst.*, *15*(9), 3521-3542, doi: 10.1002/2014GC005444.

Anderson, D. L. (2007), *New Theory of the Earth*, 2nd ed., p.^pp. 235-241, Cambridge University Press, Cambridge, UK.

Arai, R., and R. A. Dunn (2014), Seismological study of Lau back arc crust: Mantle water, magmatic differentiation, and a compositionally zoned basin, *Earth Planet. Sci. Lett.*, *390*, 304-317, doi: 10.1016/j.epsl.2014.01.014.

Asimow, P. D., and C. H. Langmuir (2003), The importance of water to oceanic mantle melting regimes, *Nature*, *421*(6925), 815-820, doi: 10.1038/nature01429.

Barklage, M., D. A. Wiens, J. A. Conder, S. Pozgay, H. Shiobara, and H. Sugioka (2015), P and S velocity tomography of the Mariana subduction system from a combined land-sea seismic deployment, *Geochem. Geophys. Geosyst.*, *16*(3), 681-704, doi: 10.1002/2014GC005627.

Bell, S. W., D. W. Forsyth, and Y. Ruan (2015), Removing Noise from the Vertical Component Records of Ocean‐Bottom Seismometers: Results from Year One of the Cascadia Initiative, *Bull. Seism. Soc. Amer.*, *105*(1), doi: 10.1785/0120140054.

Bevis, M., F. W. Taylor, B. E. Schutz, J. Recy, B. L. Isacks, S. Helu, R. Singh, E. Kendrick, J. Stowell, B. Taylor, and S. Calmantli (1995), Geodetic observations of very rapid convergence and back-arc extension at the Tonga arc, *Nature*, *374*(6519), 249-251.

Bézos, A., S. Escrig, C. H. Langmuir, P. J. Michael, and P. D. Asimow (2009), Origins of chemical diversity of back-arc basin basalts: A segment-scale study of the Eastern Lau Spreading Center, *J. Geophys. Res.*, *114*(B6), doi: 10.1029/2008jb005924.

Boneh, Y., and P. Skemer (2014), The effect of deformation history on the evolution of olivine CPO, *Earth Planet. Sci. Lett.*, *406*, 213-222, doi: 10.1016/j.epsl.2014.09.018.

Boneh, Y., L. F. G. Morales, E. Kaminski, and P. Skemer (2015), Modeling olivine CPO evolution with complex deformation histories: Implications for the interpretation of seismic anisotropy in the mantle, *Geochem. Geophys. Geosyst.*, n/a-n/a, doi: 10.1002/2015GC005964.

Caulfield, J., S. Turner, R. Arculus, C. Dale, F. Jenner, J. Pearce, C. Macpherson, and H. Handley (2012), Mantle flow, volatiles, slab-surface temperatures and melting dynamics in the north Tonga arc–Lau back-arc basin, *J. Geophys. Res.*, *117*(B11), B11209, doi: 10.1029/2012JB009526.

Conder, J. A., D. A. Wiens, and J. Morris (2002), On the decompression melting structure at volcanic arcs and back-arc spreading centers, *Geophys. Res. Lett.*, *29*(15), 1727, doi: 10.1029/2002gl015390.

Conder, J. A., and D. A. Wiens (2006), Seismic structure beneath the Tonga arc and Lau back-arc basin determined from joint Vp, Vp/Vs tomography, *Geochem. Geophys. Geosyst.*, *7*(3), Q03018, doi: 10.1029/2005gc001113.

Crawford, W. C., and S. C. Webb (2000), Identifying and Removing Tilt Noise from Low-Frequency (<0.1 Hz) Seafloor Vertical Seismic Data, *Bull. Seism. Soc. Amer.*, *90*(4), 952-963, doi: 10.1785/0119990121.

Crawford, W. C., J. A. Hildebrand, L. M. Dorman, S. C. Webb, and D. A. Wiens (2003), Tonga Ridge and Lau Basin crustal structure from seismic refraction data, *J. Geophys. Res.*, *108*(B4), 2195, doi: 10.1029/2001jb001435.

Dubois, J., G. Pascal, M. Barazangi, B. L. Isacks, and J. Oliver (1973), Travel times of seismic waves between the New Hebrides and Fiji Islands: A zone of low velocity beneath the Fiji Plateau, *J. Geophys. Res.*, *78*(17), 3431-3436.

Dunn, R. A., and F. Martinez (2011), Contrasting crustal production and rapid mantle transitions beneath back-arc ridges, *Nature*, *469*(7329), 198-202, doi: 10.1038/nature09690.

Dunn, R. A., F. Martinez, and J. A. Conder (2013), Crustal construction and magma chamber properties along the Eastern Lau Spreading Center, *Earth Planet. Sci. Lett.*, *371–372*(0), 112-124, doi: 10.1016/j.epsl.2013.04.008.

Ekström, G., G. A. Abers, and S. C. Webb (2009), Determination of surface-wave phase velocities across USArray from noise and Aki's spectral formulation, *Geophys. Res. Lett.*, *36*(18), L18301, doi: 10.1029/2009GL039131.

Escrig, S., A. Bézos, S. L. Goldstein, C. H. Langmuir, and P. J. Michael (2009), Mantle source variations beneath the Eastern Lau Spreading Center and the nature of subduction components in the Lau basin–Tonga arc system, *Geochem. Geophys. Geosyst.*, *10*(4), doi: 10.1029/2008gc002281.

Falloon, T. J., A. Malahoff, L. P. Zonenshaina, and Y. Bogdanova (1992), Petrology and geochemistry of back-arc basin basalts from Lau Basin spreading ridges at 15°, 18° and 19°S, *Mineralogy and Petrology*, *47*(1), 1-35, doi: 10.1007/BF01165295.

Faul, U., and I. Jackson (2015), Transient Creep and Strain Energy Dissipation: An Experimental Perspective, *Annu. Rev. Earth Planet. Sci.*, *43*(1), 541-569, doi: doi:10.1146/annurev-earth-060313-054732.

Faul, U. H., and I. Jackson (2005), The seismological signature of temperature and grain size variations in the upper mantle, *Earth Planet. Sci. Lett.*, *234*(1-2), 119-134.

Forsyth, D. W., S. C. Webb, L. M. Dorman, and Y. Shen (1998), Phase Velocities of Rayleigh Waves in the MELT Experiment on the East Pacific Rise, *Science*, *280*(5367), 1235-1238, doi: 10.1126/science.280.5367.1235.

Forsyth, D. W., and A. Li (2005), Array Analysis of Two-Dimensional Variations in Surface Wave Phase Velocity and Azimuthal Anisotropy in the Presence of Multipathing Interference, in *Seismic Earth: Array Analysis of Broadband Seismograms*, edited by A. Levander and G. Nolet, pp. 81-97, American Geophysical Union, Washington, D. C.

Gill, J., and P. Whelan (1989), Postsubduction Ocean Island Alkali Basalts in Fiji, *J. Geophys. Res.*, *94*(B4), 4579-4588, doi: 10.1029/JB094iB04p04579.

Goes, S., J. Armitage, N. Harmon, H. Smith, and R. Huismans (2012), Low seismic velocities below mid-ocean ridges: Attenuation versus melt retention, *J. Geophys. Res.*, *117*(B12), B12403, doi: 10.1029/2012jb009637.

Hammond, W. C., and E. D. Humphreys (2000a), Upper mantle seismic wave attenuation: Effects of realistic partial melt distribution, *J. Geophys. Res.*, *105*(B5), 10987-10999, doi: 10.1029/2000jb900042.

Hammond, W. C., and E. D. Humphreys (2000b), Upper mantle seismic wave velocity: Effects of realistic partial melt geometries, *J. Geophys. Res.*, *105*(B5), 10975-10986, doi: 10.1029/2000jb900041.

Harmon, N., and D. K. Blackman (2010), Effects of plate boundary geometry and kinematics on mantle melting beneath the back-arc spreading centers along the Lau Basin, *Earth Planet. Sci. Lett.*, *298*(3-4), 334-346, doi: 10.1016/j.epsl.2010.08.004.

Hayes, G. P., D. J. Wald, and R. L. Johnson (2012), Slab1.0: A three-dimensional model of global subduction zone geometries, *J. Geophys. Res.*, *117*(B1), B01302, doi: 10.1029/2011jb008524.

Herrmann, R. B. (2004), Computer Programs in Seismology, edited, Earthquake Center, Saint Louis Unversity, St. Louis.

Hirth, G., and D. L. Kohlstedt (1996), Water in the oceanic upper mantle: implications for rheology, melt extraction and the evolution of the lithosphere, *Earth Planet. Sci. Lett.*, *144*(1-2), 93-108, doi: 10.1016/0012-821x(96)00154-9.

Holtzman, B. K. (2016), Questions on the existence, persistence, and mechanical effects of a very small melt fraction in the asthenosphere, *Geochem. Geophys. Geosyst.*, n/a-n/a, doi: 10.1002/2015GC006102.

Isaak, D. G. (1992), High-Temperature Elasticity of Iron-Bearing Olivines, *J. Geophys. Res.*, *97*(B2), 1871-1885, doi: 10.1029/91jb02675.

Jackson, I., U. H. Faul, J. D. Fitz Gerald, and B. H. Tan (2004), Shear wave attenuation and dispersion in melt-bearing olivine polycrystals: 1. Specimen fabrication and mechanical testing, *J. Geophys. Res.*, *109*(B6), B06201, doi: 10.1029/2003jb002406.

Jackson, I., and U. H. Faul (2010), Grainsize-sensitive viscoelastic relaxation in olivine: Towards a robust laboratory-based model for seismological application, *Phys. Earth Planet. In.*, *183*(1-2), 151-163.

Jin, G., and J. B. Gaherty (2015), Surface wave phase-velocity tomography based on multichannel cross-correlation, *Geophys. J. Int.*, *201*(3), 1383-1398, doi: 10.1093/gji/ggv079.

Kanamori, H., and D. L. Anderson (1977), Importance of physical dispersion in surface wave and free oscillation problems: Review, *Rev. Geophys.*, *15*(1), 105-112, doi: 10.1029/RG015i001p00105.

Karato, S.-I. (1993), Importance of anelasticity in the interpretation of seismic tomography, *Geophys. Res. Lett.*, *20*(15), 1623-1626, doi: 10.1029/93gl01767.

Karato, S.-I. (2003), Mapping water content in the upper mantle, in *Inside the Subduction Factory*, edited by J. M. Eiler, pp. 135-152, American Geophysical Union, Washington, DC.

Karato, S.-i. (2012), On the origin of the asthenosphere, *Earth Planet. Sci. Lett.*, *321-322*, 95-103, doi: 10.1016/j.epsl.2012.01.001.

Kelley, K. A., T. Plank, T. L. Grove, E. M. Stolper, S. Newman, and E. Hauri (2006), Mantle melting as a function of water content beneath back-arc basins, *J. Geophys. Res.*, *111*(B9), B09208, doi: 10.1029/2005jb003732.

Lee, C.-T. A. (2003), Compositional variation of density and seismic velocities in natural peridotites at STP conditions: Implications for seismic imaging of compositional heterogeneities in the upper mantle, *J. Geophys. Res.*, *108*(B9), 2441, doi: 10.1029/2003jb002413.

Lin, F.-C., M. H. Ritzwoller, and R. Snieder (2009), Eikonal tomography: surface wave tomography by phase front tracking across a regional broad-band seismic array, *Geophys. J. Int.*, *177*(3), 1091-1110, doi: 10.1111/j.1365-246X.2009.04105.x.

Lin, F.-C., and M. H. Ritzwoller (2011), Helmholtz surface wave tomography for isotropic and azimuthally anisotropic structure, *Geophys. J. Int.*, *186*(3), 1104-1120, doi: 10.1111/j.1365-246X.2011.05070.x.

Lindquist, K. G., K. Engle, D. Stahlke, and E. Price (2004), Global topography and bathymetry grid improves research efforts, *Eos*, *85*(19), 186-186, doi: 10.1029/2004EO190003.

Lytle, M. L., K. A. Kelley, E. H. Hauri, J. B. Gill, D. Papia, and R. J. Arculus (2012), Tracing mantle sources and Samoan influence in the northwestern Lau back-arc basin, *Geochem. Geophys. Geosyst.*, *13*(10), Q10019, doi: 10.1029/2012GC004233.

Malahoff, A., S. R. Hammond, J. J. Naughton, D. L. Keeling, and R. N. Richmond (1982), Geophysical evidence for post-Miocene rotation of the island of Viti Levu, Fiji, and its

relationship to the tectonic development of the North Fiji Basin, *Earth Planet. Sci. Lett.*, *57*(2), 398-414, doi: 10.1016/0012-821x(82)90159-5.
Martinez, F., and B. Taylor (2002), Mantle wedge control on back-arc crustal accretion, *Nature*, *416*(6879), 417-420, doi: 10.1038/416417a.
Martinez, F., B. Taylor, E. T. Baker, J. A. Resing, and S. L. Walker (2006), Opposing trends in crustal thickness and spreading rate along the back-arc Eastern Lau Spreading Center: Implications for controls on ridge morphology, faulting, and hydrothermal activity, *Earth Planet. Sci. Lett.*, *245*(3-4), 655-672, doi: 10.1016/j.epsl.2006.03.049.
Menke, W., Y. Zha, S. C. Webb, and D. K. Blackman (2015), Seismic anisotropy indicates ridge-parallel asthenospheric flow beneath the Eastern Lau Spreading Center, *J. Geophys. Res.*, 2014JB011154, doi: 10.1002/2014JB011154.
Nishimura, C. E., and D. W. Forsyth (1989), The anisotropic structure of the upper mantle in the Pacific, *Geophys. J. Int.*, *96*(2), 203-229, doi: 10.1111/j.1365-246X.1989.tb04446.x.
Parson, L. M., and I. C. Wright (1996), The Lau-Havre-Taupo back-arc basin: A southward-propagating, multi-stage evolution from rifting to spreading, *Tectonophysics*, *263*(1-4), 1-22, doi: 10.1016/s0040-1951(96)00029-7.
Pearce, J. A., M. Ernewein, S. H. Bloomer, L. M. Parson, B. J. Murton, and L. E. Johnson (1994), Geochemistry of Lau Basin volcanic rocks: influence of ridge segmentation and arc proximity, *Geological Society, London, Special Publications*, *81*(1), 53-75, doi: 10.1144/gsl.sp.1994.081.01.04.
Pearce, J. A., P. D. Kempton, and J. B. Gill (2007), Hf-Nd evidence for the origin and distribution of mantle domains in the SW Pacific, *Earth Planet. Sci. Lett.*, *260*(1-2), 98-114, doi: 10.1016/j.epsl.2007.05.023.
Phipps Morgan, J. (1997), The generation of a compositional lithosphere by mid-ocean ridge melting and its effect on subsequent off-axis hotspot upwelling and melting, *Earth Planet. Sci. Lett.*, *146*(1–2), 213-232, doi: 10.1016/S0012-821X(96)00207-5.
Rau, C. J., and D. W. Forsyth (2011), Melt in the mantle beneath the amagmatic zone, southern Nevada, *Geology*, *39*(10), 975-978, doi: 10.1130/g32179.1.
Roth, E. G., D. A. Wiens, L. M. Dorman, J. Hildebrand, and S. C. Webb (1999), Seismic attenuation tomography of the Tonga-Fiji region using phase pair methods, *J. Geophys. Res.*, *104*(B3), 4795-4809, doi: 10.1029/1998jb900052.
Schutt, D. L., and C. E. Lesher (2010), Compositional trends among Kaapvaal Craton garnet peridotite xenoliths and their effects on seismic velocity and density, *Earth Planet. Sci. Lett.*, *300*(3-4), 367-373, doi: 10.1016/j.epsl.2010.10.018.
Shen, W., M. H. Ritzwoller, V. Schulte-Pelkum, and F.-C. Lin (2012), Joint inversion of surface wave dispersion and receiver functions: a Bayesian Monte-Carlo approach, *Geophys. J. Int.*, doi: 10.1093/gji/ggs050.
Shen, W., M. H. Ritzwoller, and V. Schulte-Pelkum (2013), A 3-D model of the crust and uppermost mantle beneath the Central and Western US by joint inversion of receiver functions and surface wave dispersion, *J. Geophys. Res.*, *118*(1), 262-276, doi: 10.1029/2012JB009602.
Shen, Y., and D. W. Forsyth (1995), Geochemical constraints on initial and final depths of melting beneath mid-ocean ridges, *J. Geophys. Res.*, *100*(B2), 2211-2237, doi: 10.1029/94jb02768.

Smith, G. P., D. A. Wiens, K. M. Fischer, L. M. Dorman, S. C. Webb, and J. A. Hildebrand (2001), A Complex Pattern of Mantle Flow in the Lau Backarc, *Science*, *292*(5517), 713-716, doi: 10.1126/science.1058763.

Sparks, D. W., and E. M. Parmentier (1993), The Structure of Three-Dimensional Convection Beneath Oceanic Spreading Centres, *Geophys. J. Int.*, *112*(1), 81-91, doi: 10.1111/j.1365-246X.1993.tb01438.x.

Takei, Y. (2002), Effect of pore geometry on V_P/V_S: From equilibrium geometry to crack, *J. Geophys. Res.*, *107*(B2), 2043, doi: 10.1029/2001jb000522.

Taylor, B., K. Zellmer, F. Martinez, and A. Goodliffe (1996), Sea-floor spreading in the Lau back-arc basin, *Earth Planet. Sci. Lett.*, *144*(1-2), 35-40, doi: 10.1016/0012-821x(96)00148-3.

The MELT Seismic Team (1998), Imaging the Deep Seismic Structure Beneath a Mid-Ocean Ridge: The MELT Experiment, *Science*, *280*(5367), 1215-1218, doi: 10.1126/science.280.5367.1215.

Turner, I. M., C. Peirce, and M. C. Sinha (1999), Seismic imaging of the axial region of the Valu Fa Ridge, Lau Basin—the accretionary processes of an intermediate back-arc spreading ridge, *Geophys. J. Int.*, *138*(2), 495-519, doi: 10.1046/j.1365-246X.1999.00883.x.

Turner, S., and C. Hawkesworth (1998), Using geochemistry to map mantle flow beneath the Lau Basin, *Geology*, *26*(11), 1019-1022, doi: 10.1130/0091-7613(1998)026<1019:ugtmmf>2.3.co;2.

Webb, S. C., and W. C. Crawford (1999), Long-period seafloor seismology and deformation under ocean waves, *Bull. Seism. Soc. Amer.*, *89*(6), 1535-1542.

Wei, S. S., D. A. Wiens, Y. Zha, T. Plank, S. C. Webb, D. K. Blackman, R. A. Dunn, and J. A. Conder (2015), Seismic evidence of effects of water on melt transport in the Lau back-arc mantle, *Nature*, *518*(7539), 395-398, doi: 10.1038/nature14113.

Wendt, J. I., M. Regelous, K. D. Collerson, and A. Ewart (1997), Evidence for a contribution from two mantle plumes to island-arc lavas from northern Tonga, *Geology*, *25*(7), 611-614, doi: 10.1130/0091-7613(1997)025<0611:efacft>2.3.co;2.

Wiens, D. A., K. A. Kelley, and T. Plank (2006), Mantle temperature variations beneath back-arc spreading centers inferred from seismology, petrology, and bathymetry, *Earth Planet. Sci. Lett.*, *248*(1-2), 30-42.

Yang, Y., and D. W. Forsyth (2006), Regional tomographic inversion of the amplitude and phase of Rayleigh waves with 2-D sensitivity kernels, *Geophys. J. Int.*, *166*(3), 1148-1160, doi: 10.1111/j.1365-246X.2006.02972.x.

Yang, Y., M. H. Ritzwoller, F. C. Lin, M. P. Moschetti, and N. M. Shapiro (2008), Structure of the crust and uppermost mantle beneath the western United States revealed by ambient noise and earthquake tomography, *J. Geophys. Res.*, *113*(B12), B12310, doi: 10.1029/2008JB005833.

Yao, H., R. D. van Der Hilst, and M. V. de Hoop (2006), Surface-wave array tomography in SE Tibet from ambient seismic noise and two-station analysis — I. Phase velocity maps, *Geophys. J. Int.*, *166*(2), 732-744, doi: 10.1111/j.1365-246X.2006.03028.x.

Yoshizawa, K., and B. L. N. Kennett (2002), Determination of the influence zone for surface wave paths, *Geophys. J. Int.*, *149*(2), 440-453, doi: 10.1046/j.1365-246X.2002.01659.x.

Zellmer, K. E., and B. Taylor (2001), A three-plate kinematic model for Lau Basin opening, *Geochem. Geophys. Geosyst.*, *2*(5), doi: 10.1029/2000gc000106.

Zha, Y., S. C. Webb, S. S. Wei, D. A. Wiens, D. K. Blackman, W. Menke, R. A. Dunn, and J. A. Conder (2014), Seismological imaging of ridge–arc interaction beneath the Eastern Lau Spreading Center from OBS ambient noise tomography, *Earth Planet. Sci. Lett.*, *408*, 194-206, doi: 10.1016/j.epsl.2014.10.019.

Zhao, D., Y. Xu, D. A. Wiens, L. Dorman, J. Hildebrand, and S. Webb (1997), Depth Extent of the Lau Back-Arc Spreading Center and Its Relation to Subduction Processes, *Science*, *278*(5336), 254-257, doi: 10.1126/science.278.5336.254.

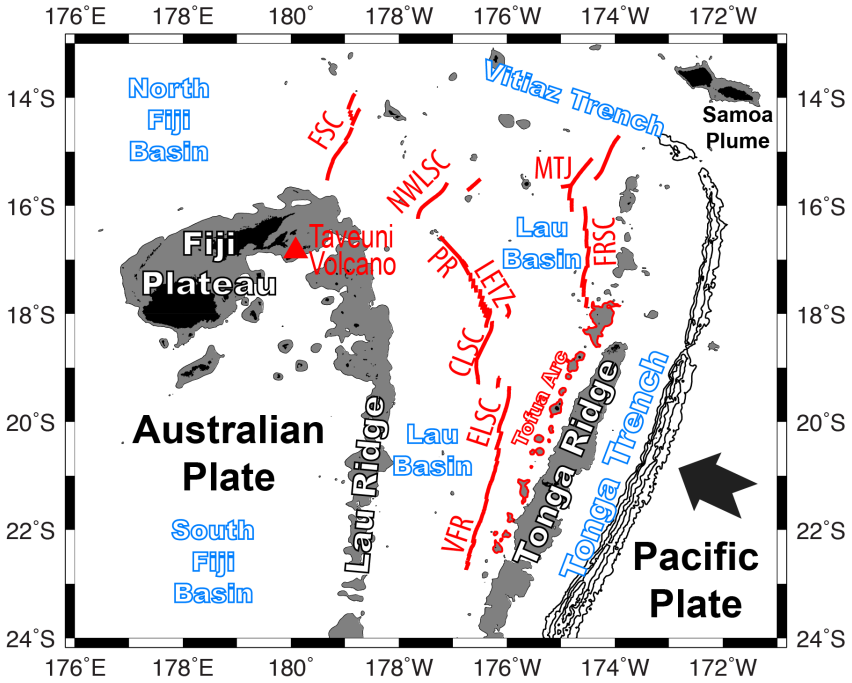

Figure 3.1. Tectonic map of the Lau Basin and adjacent areas with back-arc spreading centers (red curves).

The Pacific Plate subducts beneath the Tonga trench (delineated by bathymetry contours of 7, 8, 9, and 10 km) from the southeast (bold arrow). Areas with bathymetry shallower than 1 and 0 km are shaded in gray and black, respectively. Features with active magmatism are labeled in red. CLSC, Central Lau Spreading Center; ELSC, East Lau Spreading Center; LETZ, Lau Extensional Transform Zone; FRSC, Fonualei Rift and Spreading Center; FSC, Futuna Spreading Center; MTJ, Mangatolu Triple Junction; NWLSC, Northwest Lau Spreading Center; VFR, Valu Fa Ridge.

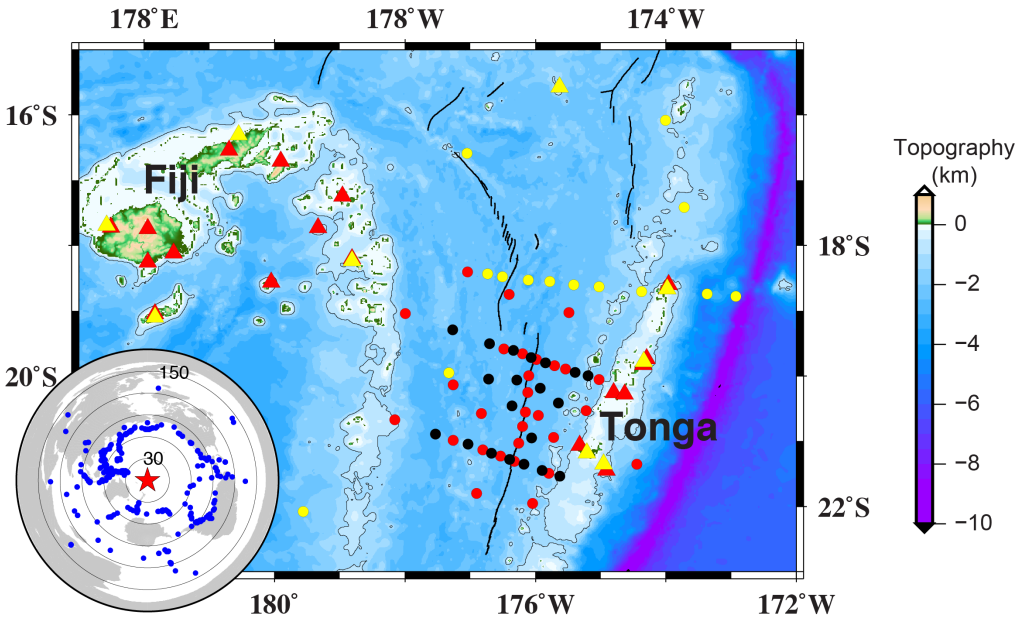

Figure 3.2. Seismic stations and earthquakes used in this study.

Red triangles represent island-based stations operated from Oct. 2009 to Dec. 2010. Red and black dots are WHOI and LDEO OBSs deployed from Nov. 2009 to Nov. 2010, respectively. Yellow dots and triangles indicate OBSs and island-based stations deployed during Sep. to Dec. 1994, respectively. Spreading centers are denoted by black curves, and the 1000 m bathymetric contours are shown. The inset shows the earthquakes (blue dots) used in this study centered at the Lau Basin (red star).

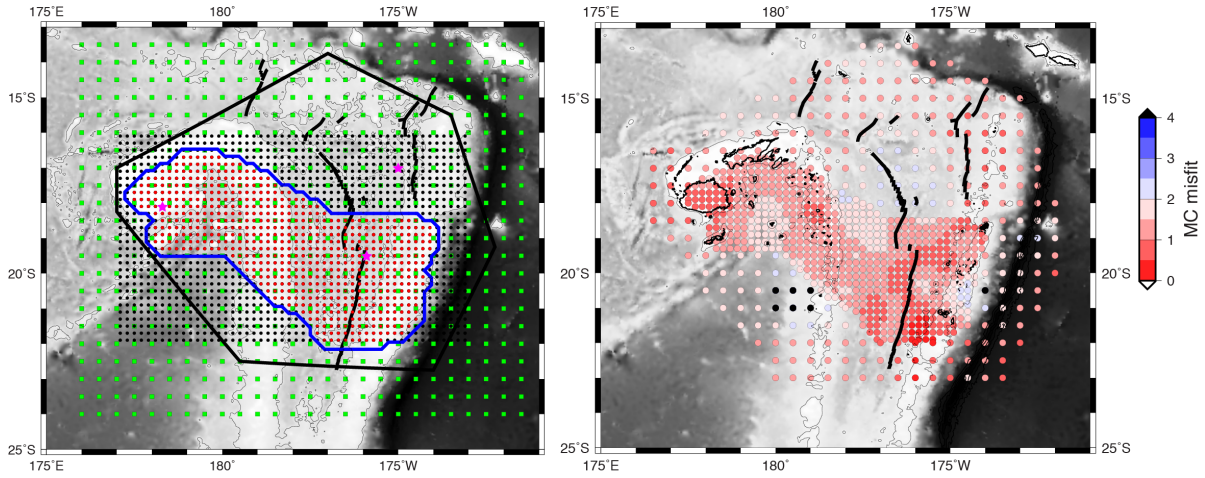

Figure 3.3. Nodes for *SV*-velocity inversion.

(a) Green dots represent the nodes for the TPWT, black dots indicated the nodes for the ANT, and red dots included by the blue contour are the nodes for the ANT-TPWT joint inversion. Black polygon outlines the region in which we display the TPWT inversion, and blue outlines the region in which we display the joint ANT-TPWT inversion, based on the areas of good resolution for each method. Magenta stars illustrate nodes used as examples shown in Fig. 3.4. (b) Misfit of the Bayesian Monte-Carlo inversion for each node. 7 nodes (black) with large misfits are discarded. The misfit is defined as the mean square root of the errors normalized by the phase-velocity uncertainties.

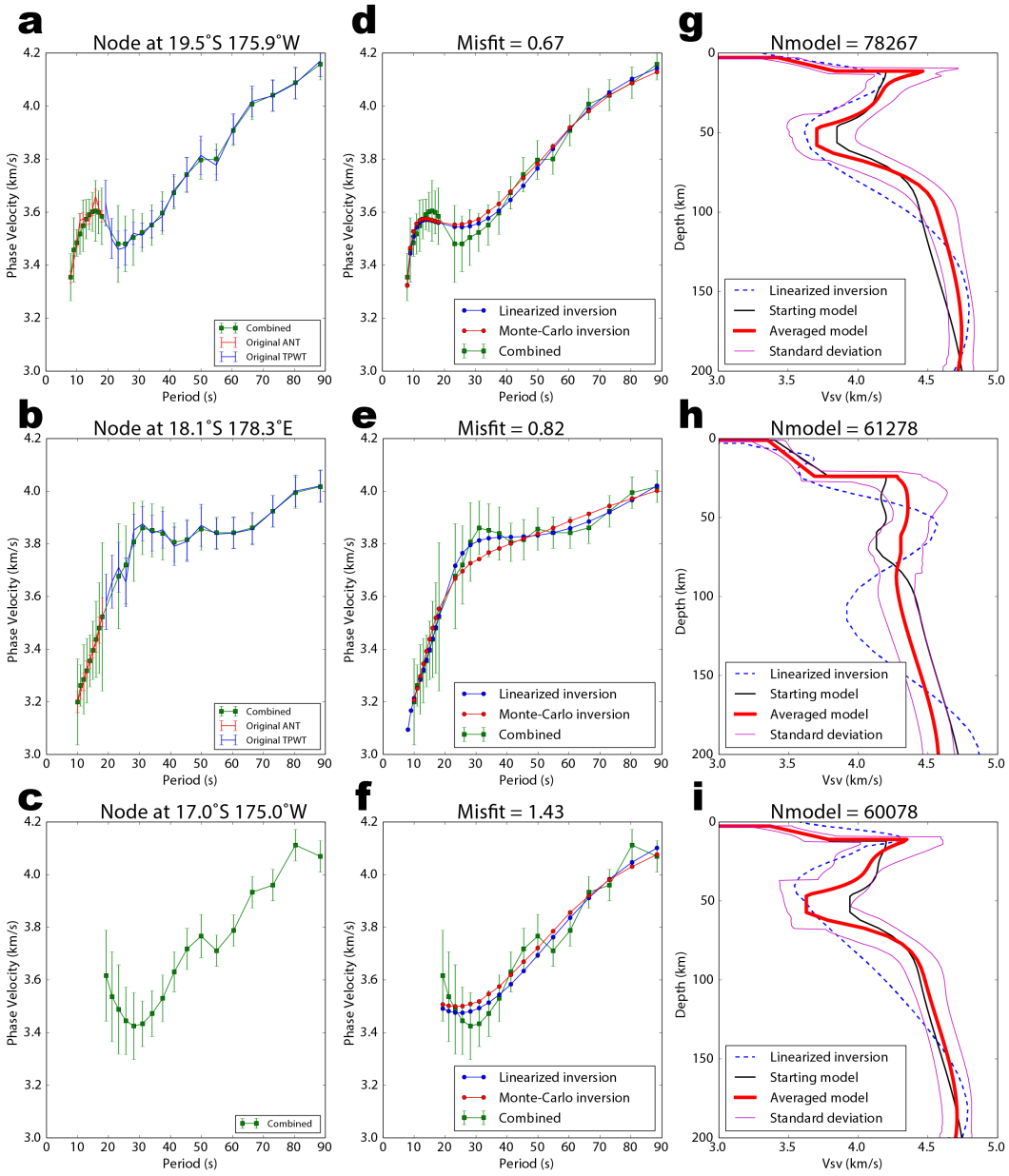

Figure 3.4. Examples of the joint ANT-TPWT dispersion curves and the results of the *SV*-velocity inversion.

Each row shows the dispersion curves and *SV*-velocity models of nodes at the ELSC (a, d, g), at the Fiji Plateau (b, e, h), and in the northern Lau Basin without ANT coverage (c, f, i). (a-c): original dispersion curves measured by the ANT (red) and the TPWT (blue) with error bars showing the standard deviations. Green curves indicate the combined dispersion curve with

amplified uncertainties. (d-f): Fit to the observed dispersion curves, with measured dispersion curves (green), dispersion curves corresponding to the linearized inversion (blue), and the average *SV*-velocity model from the Monte-Carlo inversion (red). (g-i): Resulting SV velocity models from various inversions, showing the averaged accepted model (red) with the standard deviations (magenta) in comparison with the starting model (black) and the linearized inversion result (blue dashed curve).

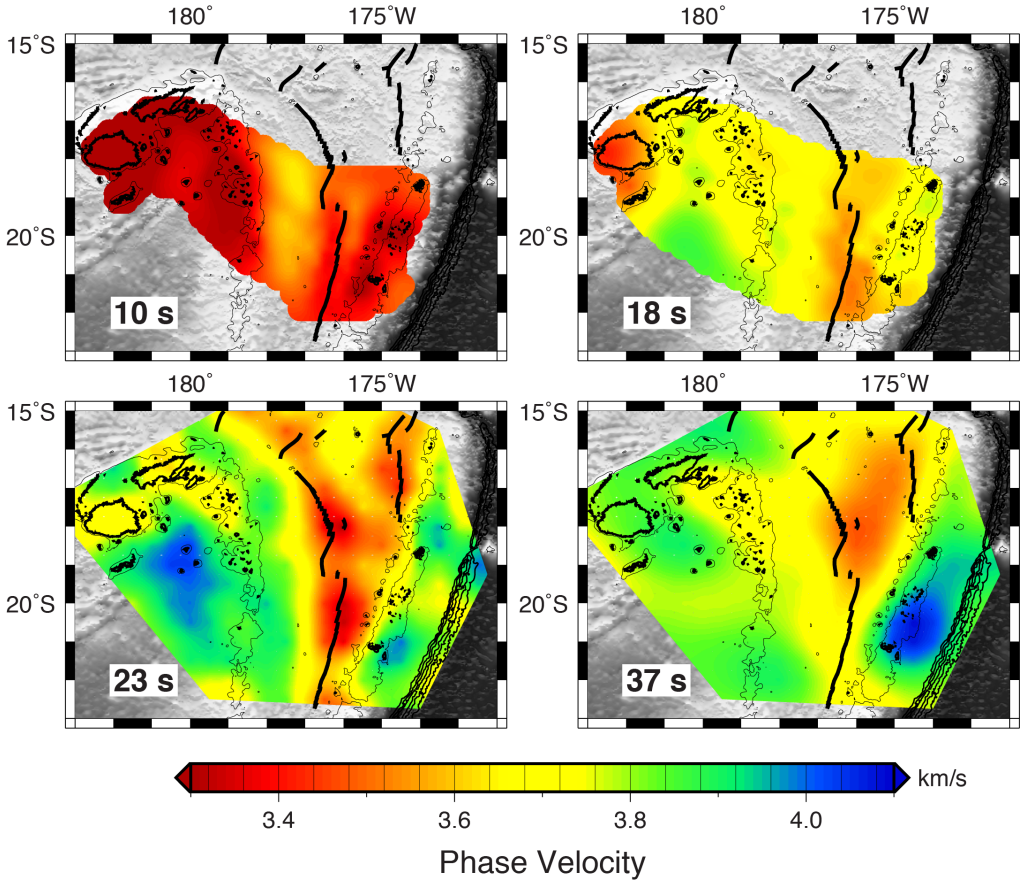

Figure 3.5. Maps of azimuthally averaged phase velocity at periods of 10 and 18 s inverted by ANT, 23 and 37 s inverted by TPWT.

Spreading centers are denoted by black lines. The 1 km bathymetric contour and the coastlines are shown to outline the Tonga Ridge, Tofua arc, Lau Ridge, and Fiji Plateau. The 7, 8, 9, and 10 km contours are also shown to delineate the Tonga trench.

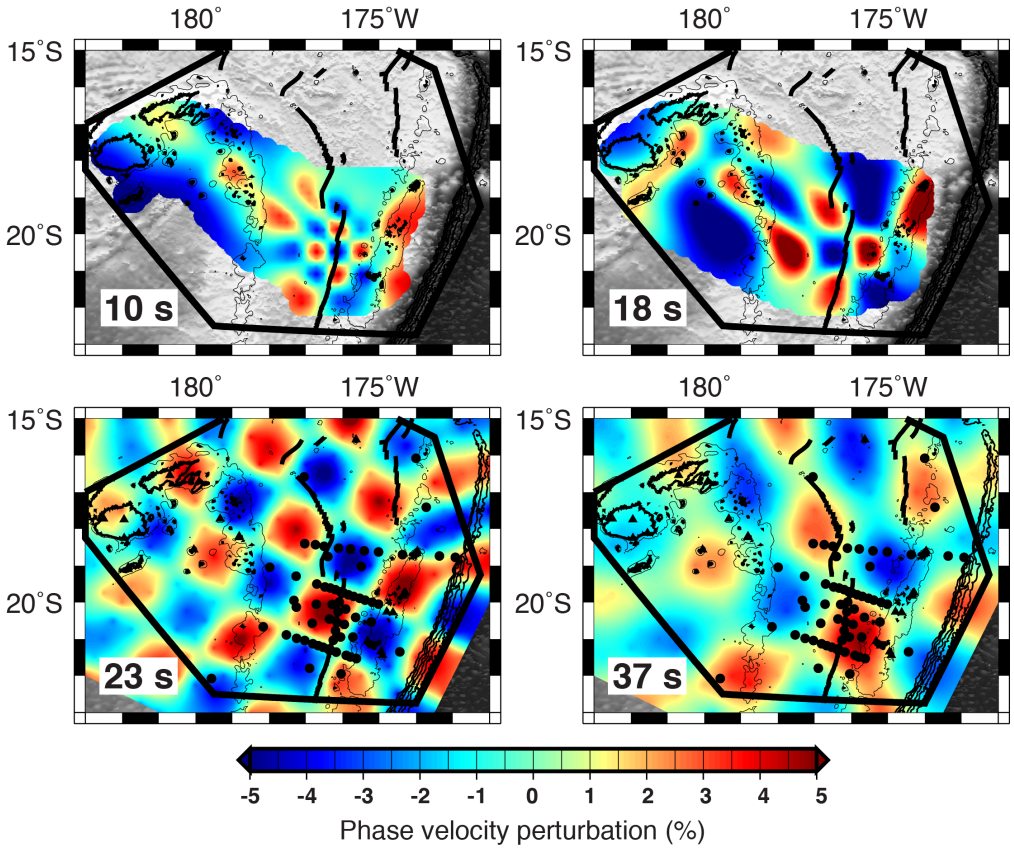

Figure 3.6. Checker board tests at periods of 10 and 18 s from the ANT, and 23 and 27 s from the TPWT.

Spreading centers and bathymetric contours are labeled the same as Fig. 3.5. The black polygon outlines the region of reasonable resolution in the TPWT phase-velocity inversion, that is displayed in the results section. Black dots on the TPWT maps show the locations of the seismic stations.

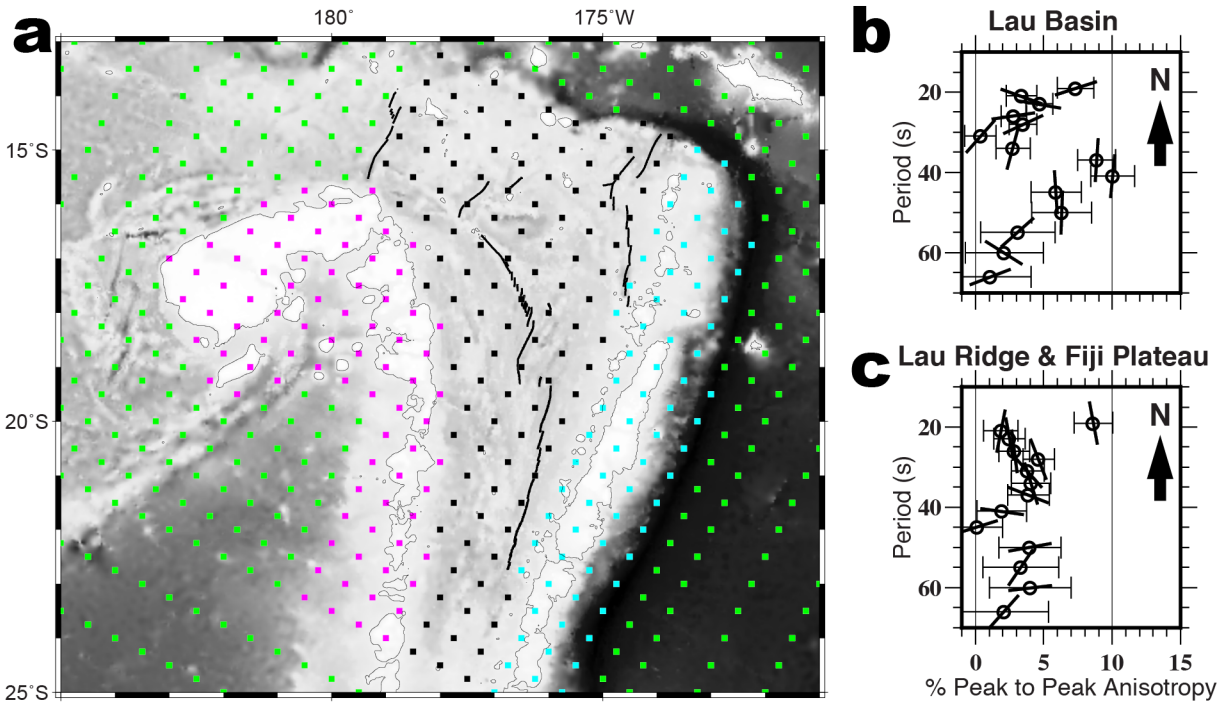

Figure 3.7. Azimuthal Rayleigh wave anisotropy results from TPWT.

(a) The nodes for the TPWT are divided into 4 tectonic subregions: the Lau Basin (black dots), the Fiji Plateau/Lau Ridge (magenta dots), the Tonga Ridge (cyan dots), and the surrounding region (green dots). Spreading centers and bathymetry contours are labeled the same as Fig. 3.5. (b) The relationship of azimuthal anisotropy to period for the Lau basin. The period is displayed on the y-axis with period increasing downwards, since shorter periods are sensitive to shallower structure. Short bars through each symbol show the fast direction in map view (the arrow shows the direction of north in map view). Error bars display doubled standard deviations. (c) The relationship of anisotropy to period for the Fiji Plateau-Lau Ridge, with symbols the same as in b.

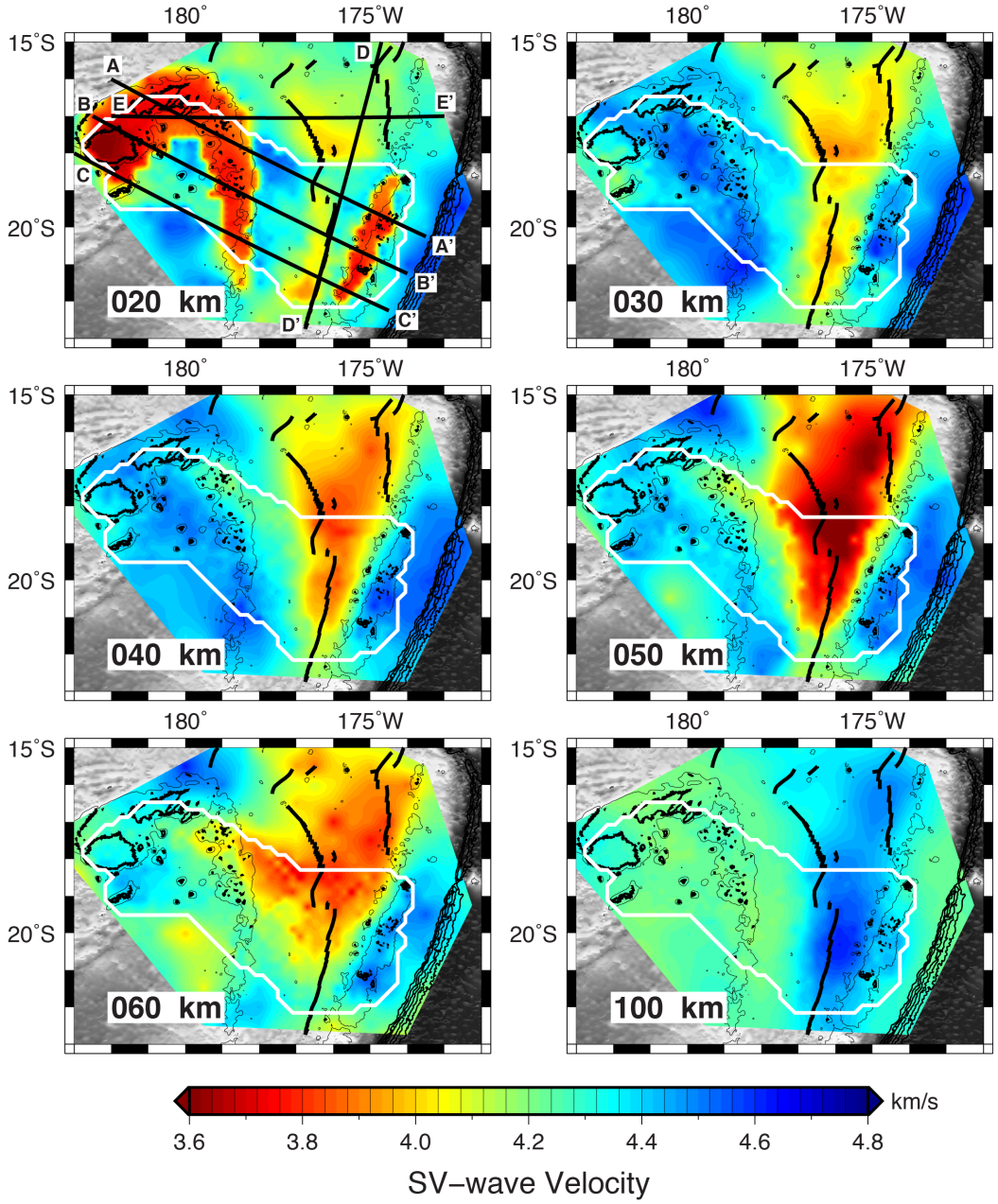

Figure 3.8. Maps of azimuthally averaged *SV*-velocity at depths of 20, 30, 40, 50, 60, and 100 km relative to sea level.

White contour encloses the region of the ANT-TWPT joint inversion. Black straight lines show the cross-sections in Fig. 3.9. The cross-sections A-A', B-B', and C-C' start from and extend perpendicular to the Tonga trench. Spreading centers and bathymetry contours are labeled as in Fig. 3.5.

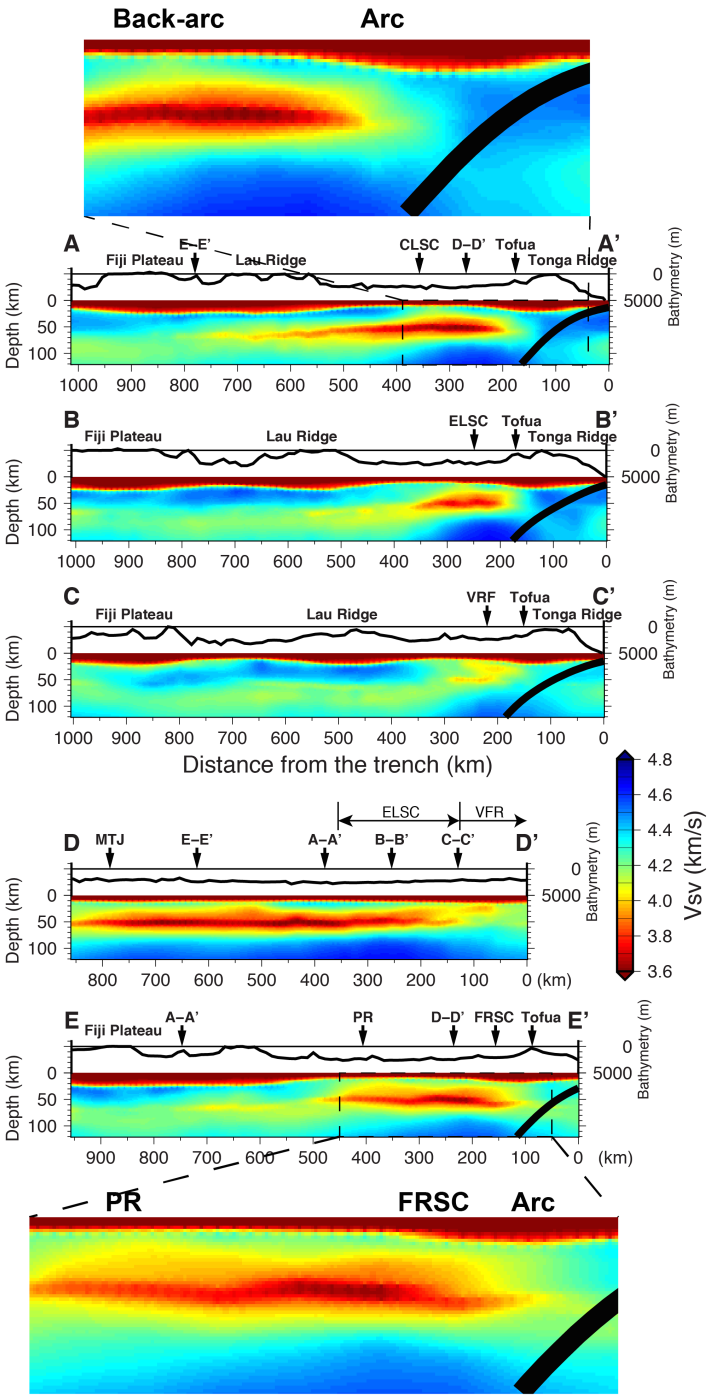

Figure 3.9. Cross-sections showing azimuthally averaged *SV*-velocity.

Black bold curves delineate the surface of the subducting slab from the Slab 1.0 model [*Hayes et al.*, 2012]. The bathymetry is plotted above with vertical exaggeration. The Lau Basin part of the cross-sections A-A' and E-E' are enlarged to show details.

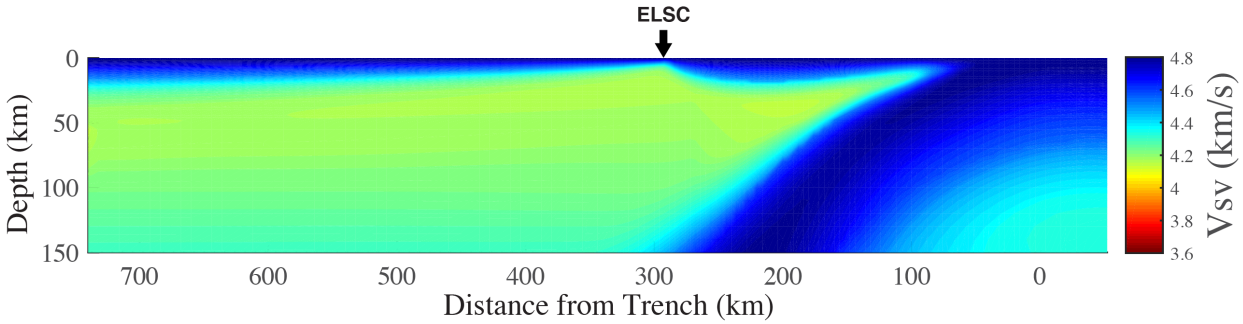

Figure 3.10. Cross-section of the predicted *SV*-velocities for the ELSC based on temperature and water content.

Calculations are based on numerical models of temperature and water content [*Harmon and Blackman*, 2010], extended Burgers model fit of experimental results relating temperature and velocity [*Jackson and Faul*, 2010], and the effects of water extrapolated from rheological relationships [*Karato*, 2012]. Isotropic S velocities predicted by the numerical results are converted to SV velocities using *Nishimura and Forsyth* [1989]. Notice the color scale is the same in Fig. 3.9. Modified from the Extended Data Fig. 8 in *Wei et al.* [2015].

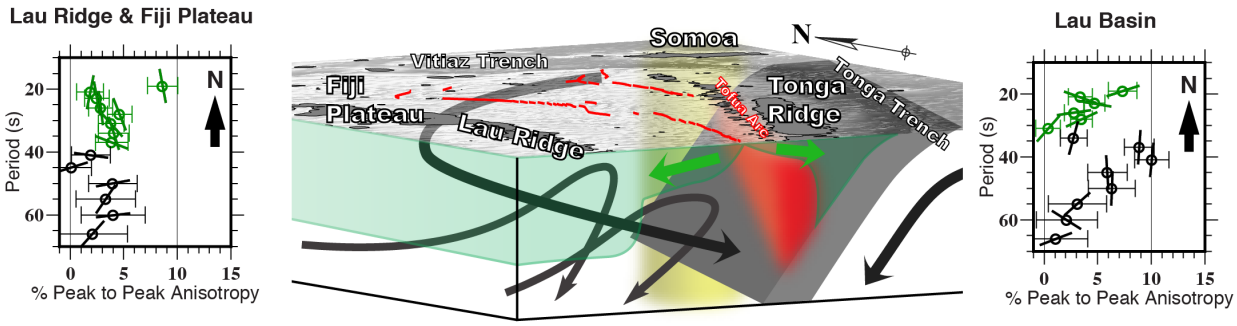

Figure 3.11. Conceptual explanation of the azimuthal anisotropy results from TPWT. Two insets are from Fig. 3.7, showing the relationship of anisotropy to period for the Fiji Plateau-Lau Ridge (left) and the Lau Basin (right). Short bars through circles indicate the fast direction in map view (the arrow shows the direction of north in map view). Error bars display doubled standard deviations. Rayleigh wave samples shallower structure at shorter periods and deeper earth at longer periods. Its maximum sensitivity to shear velocity perturbations is located at a depth of about one third of its wavelength. Consequently, we color-code the anisotropy within the lithosphere with green and those in the mantle with black, corresponding to the motion of lithosphere (green arrows) and mantle (black arrows) in the schematic plot.

Chapter 4

3-D Seismic Attenuation Structure of the Tonga-Lau-Fiji Subduction System and Implications for Mantle Melting

Abstract

We image the 3-D attenuation structures of the Tonga subduction zone and the Lau back-arc basin using local earthquake waveforms recorded by the 2009-2010 Ridge2000 Lau Spreading Center Imaging project, which consisted of 49 ocean-bottom seismographs (OBSs) and 17 island-based seismic stations deployed in Tonga, Fiji, and the Lau Basin for about one year. The amplitude spectra of *P* and *S* waves from local earthquakes are inverted for the path-average attenuation operator (t^*) along with the seismic moment and corner frequency with varying frequency-dependent exponent (α). Analysis shows that the data are best fit by the assumption of $\alpha \approx 0.27$, supporting the laboratory-based models of grain boundary sliding. The t^* measurements are inverted with various techniques to obtain 3-D tomographic models of Q_P, Q_S, and Q_P/Q_S. Results show strong anomalies of high *P*- and *S*-wave attenuation within the upper 100 km of the mantle beneath the back-arc basin, with perhaps the highest seismic attenuation ($Q_P < 30$ and $Q_S < 20$) known in the mantle found immediately beneath the spreading center.

High attenuation anomalies form an inclined zone dipping from the back-arc spreading centers to the west away from the slab. This high-attenuation zone in the back-arc requires not only the abnormally high temperature but also the existence of partial melt, suggesting that hot materials supplied from the Australian mantle upwell along with the mantle wedge flow pattern, triggering extensive decompression melting near the back-arc spreading centers. The backarc basin attenuation anomalies show low Q_P/Q_S ratios (< 1.5), in contrast to more conventional Q_P/Q_S ratios (> 1.8) beneath the Fiji Platform, implying significant bulk attenuation in the region of the mantle containing significant partial melt. *P*-wave attenuation displays different N-S trend along the back-arc spreading centers compared to *SV*-wave velocity and *S*-wave attenuation, suggesting the significant impacts of melt/free fluid on bulk attenuation.

4.1. Introduction

Melting processes in the mantle wedge are of great importance for understanding the interaction between subduction, arc volcanism, and back-arc spreading. It is widely accepted that the volatiles released from the subducting slab lower the melting temperature of the mantle wedge, resulting in flux melting to supply the volcanic arc. On the other hand, the extensional environment in the back-arc triggers decompression melting to form new crust at back-arc spreading centers [*Wiens et al.*, 2008]. Studies within the last two decades suggest that these two melting processes interact with each other, determining the geomorphology and crustal properties observed at the seafloor [*Martinez and Taylor*, 2002; *Kelley et al.*, 2006; *Dunn and Martinez*, 2011; *Zha et al.*, 2014; *Wei et al.*, 2015]. However, more details remain unknown due to the lack of high-resolution observations constraints on the subsurface structure and processes.

Therefore, investigating the details of the mantle wedge melting requires integration of various types of seismic observations. Particularly, since the structurally bound water plays a more important role in controlling seismic properties due to its abundant presence in the mantle wedge, detecting water becomes a serious challenge for seismic studies. However, it is difficult to distinguish the effects of water on seismic velocity from that of temperature [*Karato*, 2003]. Seismic attenuation provides an alternative approach to identify spatial variations of temperature, water content, and partial melt due to the different dependences of attenuation on these physical factors [*van der Lee and Wiens*, 2006].

The Tonga subduction zone and the adjacent Lau back-arc basin, one of the most active regions in the world, offer a unique opportunity to study the detailed processes of the mantle wedge melting. Here we present seismic tomographic structures of *P* and *S* wave attenuation in the Tonga-Lau-Fiji system and discuss their implications for understanding seismic attenuation

mechanisms in the mantle, as well as backarc melt distribution and subduction dynamics.

4.1.1 Tectonic Setting

The Tonga subduction zone and the adjacent Lau back-arc basin are characterized by abnormally fast convergence and back-arc spreading rates [*Bevis et al.*, 1995], as well as unusually high temperatures and large extent of melting in the back-arc [*Kelley et al.*, 2006]. The back-arc mantle melting process is thought to be significantly influenced by the adjacent subduction and the supply of slab-derived fluids, which leads to systematic variations in geochemistry [*Bézos et al.*, 2009; *Escrig et al.*, 2009], petrology [*Kelley et al.*, 2006], geomorphology [*Martinez et al.*, 2006], and seismology [*Dunn and Martinez*, 2011; *Dunn et al.*, 2013; *Arai and Dunn*, 2014; *Zha et al.*, 2014; *Wei et al.*, 2015]. In the north of the study region (Fig. 4.1a), where the Central Lau Spreading Center (CLSC) is 160-185 km away from the active Tofua arc, the influence of the subduction is minor so that the spreading center acts like a normal mid-ocean ridge (MOR) with a normal crustal thickness of 6-7 km and mid-ocean ridge basalt (MORB)-like lavas [*Kelley et al.*, 2006]. Further south, where the East Lau Spreading Center (ELSC) is 60-110 km away from the arc, the arc and back-arc melting processes interact with each other extensively to produce a thin crust with strongly depleted lavas compared to MORB. At the southernmost extent of the study region, where the Valu Fa Ridge (VFR) is 40-60 km away from the arc, the arc melting process is so dominating that the ridge appears to be assemble to the Tofua arc with similar geochemistry signatures and large crustal thickness (7.5-9 km) [*Pearce et al.*, 1994; *Turner et al.*, 1999; *Martinez and Taylor*, 2002; *Crawford et al.*, 2003; *Jacobs et al.*, 2007].

In addition to this subduction-influencing melting process, comparisons between melt

production and mantle *in situ* melt content (mantle porosity filled with melt, hereinafter melt porosity) suggest that the melt segregation and extraction are also significantly influenced by the subduction, as the water released from the slab enhances melt mobility [*Wei et al.*, 2015].

The Fiji Plateau and the Lau Ridge are parts of a remnant volcanic arc that ceased and split about 4-6 Ma before the formation of the Lau Basin. Previous seismic studies reveal a 25-35 km thick crust, a 40-50 thick lithosphere with high seismic velocity, and a hot asthenosphere with low seismic velocity and high attenuation in this region [*Roth et al.*, 1999; *Conder and Wiens*, 2006; *Wiens et al.*, 2008; *Wei et al.*, 2015; Chapter 3].

4.1.2 Seismic attenuation

Seismic attenuation quantifies the energy loss of seismic waves during propagation due to intrinsic energy dissipation by the media. The attenuation of *P* and *S* waves are characterized by the inverse of the quality factors Q_P and Q_S, respectively, and are directly determined by the anelasticity of the bulk and shear elastic moduli Q_κ^{-1} and Q_μ^{-1} as

$$1/Q_P = (1-R)/Q_\kappa + R/Q_\mu \tag{4.1}$$

$$1/Q_S = 1/Q_\mu \tag{4.2}$$

where $R = (4V_S^2)/(3V_P^2)$, V_P and V_S are the *P*- and *S*-wave velocities, respectively [*Aki and Richards*, 2002].

According to rock physics, seismic attenuation results from the anelastic behavior of mantle rocks, including grain boundary sliding, dislocation creep, and other mechanisms. Laboratory experiments at seismic frequencies show that grain boundary sliding is probably the predominant mechanism in the upper mantle, so that seismic attenuation increases exponentially with respect to temperature *T* as

$$Q^{-1} \propto \left(\omega d^m e^{\frac{E}{RT}} \right)^{-\alpha} \tag{4.3}$$

where ω is the angular frequency, d is the grain size, m is a grain-size-dependent exponent, E is the activation energy, and α is a universal frequency-dependent exponent [*Jackson et al.*, 2002; *Faul and Jackson*, 2005; *Jackson and Faul*, 2010; *Abers et al.*, 2014; *Faul and Jackson*, 2015] The anelastic response consists of a broad high-temperature background superposed by a high-frequency peak. The former background is attributed to diffusionally assisted grain boundary sliding with a strong grain-size dependence (m = 2 or 3) and a mildly frequency dependence (α = 0.27), whereas the latter peak corresponds to elastically accommodated grain boundary sliding with linear dependences on grain size and frequency (m = 1 and α = 1) [*Jackson and Faul*, 2010; *Faul and Jackson*, 2015]. Therefore, the frequency dependence should be 0.2-0.4, as used by previous seismic studies [*Stachnik et al.*, 2004; *Rychert et al.*, 2008; *Pozgay et al.*, 2009]. The extended Burgers model based on these experiments provides a quantitative way to relate temperature to seismic properties for melt- and water-free olivine aggregates [*Jackson and Faul*, 2010], though the extrapolation of these laboratory-based models needs to be carefully examined.

Although *Faul et al.* [2004] observed a strong reduction of seismic velocity and an increase of attenuation related to partial melt, the mechanism is still unclear, leading to difficulties to extrapolating experimental results to the upper mantle condition. The effect of melt is highly dependent on the geometry of the melts [*Mavko and Nur*, 1975; *O'Connell and Budiansky*, 1977; *Schmeling*, 1985; *Faul and Jackson*, 2015]. At low melt porosity, isolated melt pockets cause no energy dissipation at the seismic frequencies and affect seismic velocity only by reducing the elastic modulus. As the melt porosity increases, the melt flow between adjacent pockets may

dissipate seismic energy only for disk-shaped inclusions [*Schmeling*, 1985]. But these two mechanisms contribute only to shear attenuation, leading to $Q_P/Q_S = 2.25$. Furthermore, when the melt porosity becomes large enough, bulk fluid flow of melt in response to pressure gradients can cause bulk attenuation [*Faul and Jackson*, 2015], resulting in a smaller Q_P/Q_S ratio observed in Tonga and Marianas previously [*Roth et al.*, 1999; *Pozgay et al.*, 2009].

Structurally bounded water, i.e. hydrogen defects, could significantly increase seismic attenuation [*Karato*, 2003; *Aizawa et al.*, 2008; *Karato*, 2012]. On the other hand, the increasing water content may also lead to larger grain sizes, reducing seismic attenuation through grain boundary sliding [*Abers et al.*, 2014]. The consequence of these two competing effects is not clear, but study of mantle regions known to have a high water content, like this study, may provide some constraints. Additionally, since the water concentration beneath the Lau Basin exceeds the minimum storage capacity of nominally anhydrous mantle minerals at certain locations [*Kelley et al.*, 2006], free water may locally exist in the mantle wedge, affecting seismic properties in similar ways as melt. At greater depths and higher temperatures, however, free water will not exist and high water concentrations will produce an aqueous melt [*Hirschmann*, 2006].

4.2. Data and Methods

4.2.1 Data collection and processing

In this study we analyzed seismic data recorded at 49 ocean-bottom seismographs (OBSs) in the Lau Basin and 17 island-based temporary seismic stations on Tonga and Fiji islands (red symbols in Fig. 4.1b) deployed for about one year. Each OBS from Woods Hole Oceanographic

Institution (WHOI) used a Guralp CMG3T seismometer and a Quanterra Q330 datalogger, whereas other OBSs from Lamont-Doherty Earth Observatory (LDEO) were equipped with Sercel L-4C seismometers and LDEO-designed recorders. Each island-based station consisted of a broadband 3-component seismometer (Guralp CMG3T or Streckeisen STS-2 or Nanometrics Trillium 120 PA) and a Reftek 130-01 datalogger.

1163 local earthquakes (gray dots in Fig. 4.1b), with 94851 *P* arrivals and 14772 *S* arrivals, were manually located using this dataset. Of these events, 764 were listed in the Reviewed ISC Bulletin [*ISC*, 2013] whereas the other 399 were newly detected (Chapter 5). Since large numbers of deep earthquakes (depths 500-680 km) are present in Tonga, we detected and located new events in a depth range of 50-450 km in order to increase the amount of intermediate-depth earthquakes for better-balanced sources of tomography. Events shallower than 50 km were excluded to prevent strong wave propagations effects associated with the Moho and near-source shallow structure. We then windowed the three-channel seismogram for each event-station pair that has a clear *P* arrival. Data was downsampled to 40 sps and corrected for instrument responses. Horizontal channels were rotated into a radial-transverse coordinate system based on previously determined OBS orientations [*Zha et al.*, 2013].

4.2.2 Determining *t** and Source Parameters

We investigated path-averaged attenuation by inverting for $t^* = t/Q$, where t is the travel time for each event-station pair. For the k-th earthquake recorded at the j-th station, the displacement spectrum $A_{jk}(f_i)$ can be expressed as

$$A_{jk}(f_i) = \frac{C_{jk} M_{0k} e^{-\pi f_i^{1-\alpha} t^*_{0\,jk}}}{1+(f_i/f_{ck})^2} \tag{4.4}$$

$$\ln\left\{A_{jk}\left(f_i\right)\right\}+\ln\left\{1+\left(f_i/f_{ck}\right)^2\right\}-\ln\left\{C_{jk}\right\}=\ln\left\{M_{0k}\right\}-\pi f_i^{1-\alpha}t_{0jk}^{*} \quad (4.5)$$

where C_{jk} is a constant factor for each event-station (*k-j*) pair accounting for frequency-independent effects, M_{0k} and f_{ck} are the seismic moment and corner frequency for this event *k*, respectively, and t_{0jk}^{*} is the attenuation factor at 1 Hz for event *k* and station *j* [e.g. *Anderson and Hough*, 1984]. C_{jk} can be approximately estimated by combining effects of geometric spreading [*Kanamori and Stewart*, 1976], free surface [*Helmberger*, 1974], and a spherically averaged radiation pattern [*Aki and Richards*, 2002]. Eq. 4.5 is then solved with a non-negative least square algorithm for the attenuation along each path t_{0j}^{*} as well as M_0 and f_c for the event. This method has been widely used at several subduction zones [*Stachnik et al.*, 2004; *Rychert et al.*, 2008; *Pozgay et al.*, 2009], so here we emphasize the differences and improvements.

For each *P* wave, the signal was windowed for 5 s starting 0.5 s before the arrival pick on the vertical channel, and the noise was windowed with the same length immediately preceding the signal window (Fig. 4.2a). Both spectra of signal and noise were calculated with a multi-taper technique [*Lees and Park*, 1995], and the frequency band used in Eq. 4.5 was automatically determined as the largest frequency range in which the spectral signal-to-noise ratio (SNR) is consistently higher than 2 (Fig. 4.2c). Only spectra with a frequency range larger than 3 Hz are used in the inversion. For each *S* wave, the data window and frequency band are determined in the similar way on the transverse channel, with a window length of 8 s, the critical SNR of 1.8, and the minimum frequency range of 1 Hz (Figs. 4.2b and 4.2d). Even with this weaker quality control for *S* waves, the amount of usable *S* signals is about one tenth of that of *P* signals due to the extremely high *S*-wave attenuation in the back-arc (Fig. 4.3).

Because of the intrinsic trade-off between the source corner frequency (f_c) and the attenuation

term (t^*), the inversion sometimes results in unrealistic values of f_c. We applied *a priori* information about how corner frequency scales with body-wave magnitude (m_b) from the Reviewed ISC Bulletin [*ISC*, 2013] to constrain f_c within a reasonable range of stress drops. We use the assumption of a circular rupture [*Anderson*, 1986] and empirical relationships

$$f_c = 0.49\beta\left(\Delta\sigma/M_0\right)^{1/3} \tag{4.6}$$

$$\log M_0 = 1.5M_W + 9.095 \tag{4.7}$$

$$M_W = 1.54m_b - 2.54 \tag{4.8}$$

where β is the shear velocity (assumed as 4 km/s), $\Delta\sigma$ is the stress drop, and M_W is the moment magnitude [*Anderson and Hough*, 1984; *Hough*, 1996; *Hough et al.*, 1999; *Pozgay et al.*, 2009; *Das et al.*, 2011]. The magnitude-frequency distribution of the Reviewed ISC Bulletin [*ISC*, 2013] suggests a complete detection of earthquakes with m_b larger than 4, whereas some smaller events as small as m_b = 3 can still be detected [*Willemann*, 1999]. Therefore, we assume m_b as 3.0 for those earthquakes not listed in the Reviewed ISC Bulletin [*ISC*, 2013]. We use upper and lower bounds of $\Delta\sigma$ of 20 and 0.5 MPa to determine reasonable bounds on the minimum and maximum f_c, and carried out a grid search over those f_c using Eq. 4.5 to determine the best fitting f_c and t^* (Figs. 4.2e and 4.2f). In addition, we required the *S*-wave corner frequency $f_{c(S)}$, usually poorly constrained because of the limited *S* wave frequency range, to be equal to $f_{c(P)}$. After trying different values of α, we assumed a slight frequency dependence with α = 0.27 according to previous laboratory experiments [*Jackson et al.*, 2002; *Jackson and Faul*, 2010]. The validation of these assumptions will be discussed in the next section.

After the first round of inversion of Eq. 4.5 for each event, we compared the observed spectrum with the synthetic one calculated from the inverted f_c and t^* values. Event-station pairs with a poor fit were discarded and only the good pairs were input for the second round of

inversion to produce the final results of t^*. In this way very poor fitting data due to high noise levels or instrument malfunction were not used in the overall estimates of M_0 for each event and the final t^* measurements.

4.2.3 Evaluating Assumptions of the t^*-inversion

In order to test our assumptions for the corner frequency and α value, we additionally conducted t^*-inversions over all events with a fixed stress drop (the corner frequency of each event is fixed according to Eqs. 4.6-4.8) and α value, and then use the average misfit of all t^*-inversions for each set of parameters as an indicator of the goodness of our assumptions. Fig. 4.4 shows that the method of determining the corner frequency by a grid search produces lower misfit by introducing an additional variable, but misfits with fixed stress drops do not show significant preference. This means that the choice of the stress drop and the corner frequency does not dramatically affect the t^*-inversion. We thus conclude that the grid search over f_c is the best way to eliminate the trade-off between f_c and t^*, as previously discussed by *Stachnik et al.* [2004], *Rychert et al.* [2008], and *Pozgay et al.* [2009].

Although we are not able to directly invert for α, the misfit reaches minimum when $\alpha = 0.3$ for every set of stress drops. This agrees well with the value suggested by laboratory experiments (0.27) for attenuation in high temperature polycrystalline olivine, which is interpreted using a model of grain boundary relaxation [*Jackson et al.*, 2002; *Jackson and Faul*, 2010]. Because of the generally good agreement with the laboratory results, and because we cannot determine the best fitting α with high precision, we use t^* measurements determined assuming $\alpha = 0.27$ as suggested by laboratory experiments and a grid search over the stress drop and f_c for the tomographic inversion.

4.2.4 Tomographic Inversion

The tomographic problem for attenuation structure is given by

$$t_i^* = \sum_j \frac{l_{ij}}{v_j} \frac{1}{Q_j} = G_{ij} m_j \tag{4.9}$$

where t_i^* is the t^* measurement of the i-th seismic ray, the seismic velocity of the j-th node (v_j) and the path length for the i-th ray in the block around the j-th node (l_{ij}) together form the tomography kernel G_{ij}, and the attenuation of the j-th node (Q_j^{-1}) is the model parameter m_j. We inverted Eq. 4.9 separately for Q_P and Q_S using the measurements of $t^*_{(P)}$ and $t^*_{(S)}$, respectively. A 2-D *P*- and *S*-wave velocity model from previous regional tomography [*Conder and Wiens*, 2006], was adopted and projected parallel to the trench to build a 3-D velocity model. Seismic path lengths and travel times were calculated by ray tracing with a pseudo-bending algorithm [*Um and Thurber*, 1987]. We ignored the uncertainties of the velocity model, raypaths, and travel times, since the uncertainties of the t^* measurements are much more significant.

The tomographic inversion was performed using a generalized least-squares method with a maximum-likelihood linear inverse solution [*Tarantola and Valette*, 1982; *Menke*, 2012; 2014]. An assumed uncertainty in theory of 0.03 s was input into the inversion based on previous experience [*Stachnik et al.*, 2004; *Rychert et al.*, 2008]. Since the most attenuated signal should be buried in noise, the tomographic results of attenuation could be underestimated. For the same reason, we set the *a priori* model of Q^{-1} as zero, so that the final results would give a lower bond of attenuation structure. A second-derivative smoothing and damping constraints were also imposed as *a priori* information. We conducted a series of inversions with different smoothing and damping coefficients, and chose the values that best balance the model resolution and misfit

(details in Section 4.3.3).

The much smaller number of good *S*-wave t^* measurements resulting from the high attenuation causes some difficulty in determining a good Q_S model and in comparing Q_S and Q_P structure. Therefore we utilized a several different methods for the tomographic inversions. Table 4.1 lists all cases of Q inversion. The last column shows the cases producing the final reliable results that we use for the discussion and interpretation.

For the Q_P inversion with more than 10,000 $t^*_{(P)}$ values, we used a 3-D grid of nodes spacing 29 km horizontally and 25 km vertically down to the depth of 300 km and a 1-D structure between 300-700 km where lateral resolution is poor (Case 1). We excluded t^* measurements with from earthquakes outside the study region with raypaths that have sampled structures above 300 km before entering the 3-D grid. A biconjugate-gradient technique [*Barrett et al.*, 1994] was used to reduce the computational expense. However, this technique may result in negative Q_P^{-1} values at certain nodes with poor data coverage. In order to avoid these unrealistic solutions, we started with the best parameters for the final inversion, and iteratively increased the damping coefficient. The starting model in each iteration was adopted from the previous inverted model except that all negative Q_P^{-1} values were replaced by 0.0001 [*Rychert et al.*, 2008]. For Q_S with only a few thousands of $t^*_{(S)}$ measurements, we used a sparser grid of nodes spacing 77 km horizontally and 25-100 km vertically down to the depth of 300 km (Case 2). The tomographic inversion was performed in the same way as for Q_P^{-1} except that a non-negative least square algorithm instead of the biconjugate-gradient technique with iterations was utilized.

Since the amount of *S*-wave data is less than 1/10 of the *P*-wave data, we additionally inverted $t^*_{(S)}$ with the more robust Q_P model, so that *P*-wave data helps constrain the *S*-wave attenuation (Case 3):

$$\left(t^{*}_{(S)}\right)_i = \sum_j \left[\frac{\left(l_S\right)_{ij}}{\left(v_S\right)_{ij}} \left(\frac{1}{Q_P} \right)_j \right] \left(\frac{Q_P}{Q_S} \right)_j = G_{ij} m_j \tag{4.10}$$

Compared to the Eq. 4.9, the model parameter becomes $(Q_P/Q_S)_j$ at the j-th node, and Q_P^{-1} is inverted with $t^*_{(P)}$ data previously. Unlike the direct inversions of Q^{-1}, this inversion of Q_P/Q_S does not produce negative solutions. We thus used the damped Singular Value Decomposition (SVD) method to invert the Eq. 4.10 with the same grid of nodes used for independently inverting for Q_S^{-1}. The Q_S^{-1} model is simply the product of the inverted Q_P/Q_S and the Q_P^{-1} model, which is separately inverted with $t^*_{(P)}$ data. This strategy greatly improves the vertical resolution of Q_S beneath the Fiji Plateau (Figs. 4.8e and 4.8h), since almost all *S* waves recorded at the Fijian stations come from deep earthquakes along near-vertical raypaths.

However, the joint inversion of Q^{-1} may introduce biases to Q_P/Q_S due to the different sampling of *P* and *S* waves. As shown in Fig. 4.3, *S* waves are more attenuated than *P* waves. So S waves are often not observed for the most highly attenuating paths, while *P* signals are analyzed and contribute to the tomographic inversion. This may produce a bias in which Q_S^{-1} and Q_P/Q_S are underestimated. Therefore, to obtain the best estimate of the Q_P/Q_S ratio, we selected event-station pairs which have both reliable measurements of $t^*_{(P)}$ and $t^*_{(S)}$, and inverted for Q_P^{-1} and Q_S^{-1} independently with same damping and smoothing coefficients (Case 4). The inversions were performed in the same way as Case 2. The final model of Q_P/Q_S is given by directly dividing Q_S^{-1} model by Q_P^{-1} model with the optimistic parameters. Nodes with too high Q_P or Q_S were masked out to avoid computational instabilities. Due to the limited data and resolution, we do not invert for bulk attenuation, but infer it from Q_P/Q_S ratios.

4.3. Results

4.3.1 Path-averaged Attenuation at each Station

We obtained 20716 robust measurements of *P*-wave t^* and 1523 for *S* wave. Extreme t^* values ($t^* < 0$ or path-averaged $1/Q_P > 30$ or path-averaged $1/Q_S > 50$), which may result from the non-negative least squares inversion, were discarded, leaving 20690 $t^*_{(P)}$ and 1514 $t^*_{(S)}$. About 10% of these t^* measurements were further excluded for the tomographic inversions as those raypaths sample structures out of the inversion grid, leaving the number of data shown in Table 4.1. Fig. 4.5 plots the depth distribution of all earthquakes for these t^* measurements, showing that earthquakes are the predominant sources. Consequently, the majority of the raypaths are nearly vertical, resulting in limited vertical resolution in the tomography.

Before the tomographic inversions, we estimate the path-averaged attenuation $Q^{-1} = t^*/t$ and path-averaged $Q_P/Q_S = (t^*_{(S)}/t_S)/(t^*_{(P)}/t_P)$ for each event-station pair. Fig. 4.6a shows an example of *P* waves from one earthquake recorded at several stations. The path-averaged attenuation observed at the fore-arc and the Fiji Plateau is obviously lower than near the back-arc spreading center. The mean values of the path-averaged attenuation and Q_P/Q_S originating from the entire dataset of earthquakes deeper than 410 km are plotted at each station in Fig. 4.6. The fore-arc stations are characterized by low *P*- and *S*-attenuation whereas high attenuations are observed in the back-arc. Perhaps surprisingly, the Fijian stations show somewhat higher *S*-attenuation compared to the ones in the Lau Basin. This probably reflects a thick layer of high asthenospheric attenuation beneath the Fiji Plateau and the Lau Ridge lithosphere as shown in the tomographic results in the next section, as well as the fact that the path-averaged Q_P/Q_S appears is near the expected value (2.25) beneath Fiji but is anomalously low beneath the backarc spreading center.

4.3.2 Tomographic Results

Tomographic Q_P^{-1} images show strong high-attenuation anomalies in the upper mantle beneath the Lau Basin in contrast to the subducting slab with low attenuation (Fig. 4.7). These anomalies form an inclined zone extending from shallow in the back-arc to deep away from the subducting slab (Figs. 4.7e-4.7g). The strongest anomalies are imaged along the southern ELSC and northern VFR but are lower amplitude at the CLSC, which may partially reflect less dense station and raypath coverage in this area. The Fiji Plateau-Lau Ridge is characterized by a thick lithosphere with low attenuation underlying by a thick high-attenuation asthenosphere. Since the majority of the sources are deep earthquakes, the poor vertical resolution may bias the depths and thickness of the high-attenuation anomalies. Similar features are also imaged in a *S*-velocity structure from Rayleigh wave tomography [*Wei et al.*, 2015] but with a better constraint on depths. It should be noted that these results have poor relative resolution in areas of very low attenuation, thus some regions have zero attenuation when they almost certainly should have small but non-zero values.

The *S*-wave dataset contains relatively fewer sources at intermediate depths (Fig. 4.5), because the intermediate-depth events are smaller on average. This results in much fewer non-vertical raypaths contributing to the tomographic inversion for *S* waves than for *P* waves. In fact, the *S*-wave attenuation in the back-arc is so high that no *S* wave along a near-horizontal raypath can be observed at the Fijian stations, consistent with previous observations by *Barazangi and Isacks* [1971]. Thus no horizontal ray contributes to the independent inversion of Q_S (Case 2), leading to poorly constrained features beneath Fiji (Fig. 4.8h). Therefore, we prefer the *S*-wave attenuation tomography carried out using the *P*-wave attenuation as a constraint (case 3), which

constrains the structures beneath Fiji with the help of *P* waves (Figs. 4.8a-4.8g). The resulting structures beneath the back-arc (Fig. 4.8e) are similar to the results of Case 2 (Fig. 4.8g), supporting the usage of this strategy. A similar high-attenuation region for *S* waves is imaged beneath the Lau Basin compared to the Q_P model. However, the depth range of high attenuation beneath the Lau Basin might be underestimated as more *S*-wave signals from intermediate-depth events are missed.

Q_P/Q_S ratios determined using the above methods may be biased due to the much better sampling of *P* waves, for instance, the extremely low Q_P/Q_S anomaly near the slab beneath the back-arc in Fig. 4.9a. We thus prefer the Q_P/Q_S results using only source-station pairs with both *P* and *S* observations (Case 4) shown in Figs. 4.9b and 4.9c. Extremely low Q_P/Q_S ratios down to 0.8 are imaged near the intermediate-depth slab and beneath the back-arc basin, whereas the Q_P/Q_S beneath Fiji is about 1.8-2.0, relatively close to the expected 2.25 for attenuation purely in shear. The Q_P/Q_S values in the mantle wedge are consistently lower than 1.5. Overall these results are consistent with *Roth et al.* [1999], who determined an average Q_P/Q_S ratio of 1.75 for the entire region.

4.3.3 Resolution and Extreme Values

One crucial question of the tomographic inversions is the choice of damping and smoothing coefficients. We first conducted a series of inversions with varying coefficients and then calculated the model misfits (Fig. 4.10). The misfit does not change significantly when the smoothing and damping are small enough, although the inversion results may still vary dramatically.

Therefore, more synthetic tests were carried out to determine the optimal parameters for the

inversions. Figs. 4.11a and 4.11b show the recovery of the *P*-attenuation inversion for a checkerboard structure. We also constructed a synthetic structure as expected to investigate the recovery (Figs. 4.11c and 4.11b). These results suggest that *P*-attenuation structure can be well resolved in the back-arc basin, but the features beneath the Fiji Plateau and the Lau Ridge are significantly elongated and smeared along the dominant direction of the seismic raypaths. This is due to the poor azimuthal coverage of earthquakes used in the tomographic inversions. Therefore, the high-attenuation zone beneath Fiji could likely be thinner with a higher attenuation amplitude compared to features shown in Figs. 4.7 and 4.8. Similar tests were also conducted for the Q_S and Q_P/Q_S inversions to choose the optimal parameters for damping and smoothing.

4.4. Discussion

4.4.1 Physical Implications of High Seismic Attenuation

High seismic attenuation is indicative of high temperature, water content, and/or melt porosity [*Karato*, 2003; *Faul et al.*, 2004; *Jackson and Faul*, 2010; *McCarthy et al.*, 2011; *Faul and Jackson*, 2015], thus giving non-unique implications. In general, our *P*- and *S*-wave attenuation results for the Tofua arc and the Lau back-arc (minimum Q_P = 30-50 and Q_S = 20-35) are much greater than those observed at Alaska (minimum Q_P = 205-345 and Q_S = 95-140) [*Stachnik et al.*, 2004], Central America (minimum Q_S = 38-84) [*Rychert et al.*, 2008], Mariana arc (minimum Q_P = 56-70 and Q_S = 45-58), and Mariana back-arc (minimum Q_P = 43-60 and Q_S = 33-42) [*Pozgay et al.*, 2009]. These values anti-correlate with the inferred *in situ* temperatures, suggesting that temperature is the predominant factor to control seismic attenuation in the

arc/back-arc systems.

In order to investigate the effects of thermal variations and water content, we converted a 2D numerical model for the ELSC and Tonga mantle wedge by *Harmon and Blackman* [2010] to *S*-wave attenuation (Fig. 4.12c). Following *Wei et al.* [2015], the conversion is based on available rock physical models and experimental constraints: (1) the extended Burgers models that fits data of forced torsional oscillation experiments (hereinafter JF10 model [*Jackson and Faul*, 2010]) and (2) an assumption of water effects by scaling the characteristic frequency of grain boundary relaxation ω_{gbs}

$$\frac{\omega_{gbs}(C_W)}{\omega_{gbs}(C_W^0)} = \left(\frac{C_W}{C_W^0}\right)^r \exp\left[-\frac{H^*}{RT_0}\left(\frac{T_0}{T}-1\right)\right] \tag{4.11}$$

where C_W is the water content, C_W^0 is the reference water content (= 10^{-4} wt.%), r is an exponent constant of water effects between 1 and 2, T is the temperature, T_0 is the reference temperature (= 1300 K), and H^* is the activation enthalpy for grain boundary sliding [*Karato*, 2012]. Since the potential temperature used in the numerical models is 1450 ˚C, slightly higher than the value revealed from geochemistry [*Kelley et al.*, 2006], and r is chosen as 2, lying at the upper limit, the predicted seismic attenuation should draw the upper bound for observations. Furthermore, we calculated Q_P models for the ELSC by assuming Q_P/Q_S = 1.75 according to *Roth et al.* [1999] (Fig. 4.12a) or Q_P/Q_S = 2.25 for no bulk attenuation (Fig. 4.12b). We are aware that several parameters of the models are poorly constrained and assumptions are in need of further verifications. However, these calculations provide an effective way to visualize the effects of temperature and water, and estimate the highest possible values of seismic attenuation based on current knowledge.

These calculations, along with other extrapolation of laboratory-based attenuation models

[e.g. *McCarthy et al.*, 2011], always predict several times less attenuation than observed. By comparing Fig. 4.12 with Figs. 4.7f and 4.8e, several first-order discrepancies can be noted. Although high attenuation is predicted beneath the Tofua arc due to the high water content, the observed sharp boundary between high and low attenuation beneath the arc cannot be modeled since the water distribution is more diffusive, and high attenuation is predicted in the fore-arc where we observe low attenuation. In addition, water cannot explain the large attenuation observed centered beneath the ELSC, where the mantle has much lower water content than beneath the Tofua arc. This discrepancy implies that the structurally bound water is not the primary contributor to the observed high attenuation and its effects on seismic properties may be overestimated in the prediction. The observed high-attenuation within the mantle wedge is not predicted by the models, showing a similar discrepancy between the predicted *SV*-velocity and observations [*Wei et al.*, 2015]. The extremely high attenuation beneath the Lau Basin cannot be explained by variations of temperature and water content, even if the big uncertainties of these predications are taken into account.

The extremely high attenuation observed beneath the volcanic arc and back-arc could be explained if melt and/or free water plays a more important role than previous suggestions such as *Hammond and Humphreys* [2000a]. In order to reconcile observations of seismic attenuation over different subduction systems, *Abers et al.* [2014] rescaled the effective viscosity and relaxation time of the JF10 model by a factor of 42. The adjusted JF10 model can fit most observations at arcs with a melt porosity of 1%, although observations at back-arc basins, including this study, requires the melt porosity to be higher than 4% (Fig. 11 in *Abers et al.* [2014]). Such high melt porosity, however, seems to be unrealistic given the U-isotropic studies [*McKenzie*, 2000] and microstructure of mantle rocks [*Zhu et al.*, 2011; *Miller et al.*, 2014],

suggesting the effects of melt on attenuation may be still underestimated. One possible mechanism for melt-related attenuation is melt squirt [*Mavko and Nur*, 1975], which was generally assumed to be effective at frequencies higher than seismic band. But our results unambiguously show Q_P/Q_S lower than 1.5 beneath the back-arc basin, where partial melting is expected, requiring a mechanism for bulk attenuation. Mechanisms involving free fluid flow, such as melt squirt, need to be reconsidered as nonequilibrium melt geometries and stress-driven melt segregation may make these mechanisms more effective at seismic frequency band [*Cooper*, 2002; *Holtzman and Kendall*, 2010; *Abers et al.*, 2014].

Although it is difficult to distinguish the effects of melt/fluid from the big uncertainties of model predictions, melts must play an important role in increasing seismic attenuation to such high values. Therefore, we are confident to attribute the strong anomalies of high attenuation beneath the back-arc spreading centers to the presence of *in situ* partial melting, but hesitated to evaluate the melt porosity.

4.4.2 Back-arc melting with high attenuation

High *P*- and *S*-wave attenuation anomalies are imaged beneath the Lau Basin, forming an inclined zone dipping to the west away from the trench, indicative of high temperature and partial melt. This pattern is in agreement with the *SV*-velocity structure from Rayleigh wave tomography (Fig. 4.13) [*Wei et al.*, 2015; Chapter 3], implying a broad and asymmetric region of hot materials upwelling from the deep west to supply the mantle wedge. This process triggers extensive decompression melting that generates large amount of magma erupting at the back-arc spreading centers as well as remaining in the upper mantle. However, the attenuation structures also show several features different from the *SV*-velocity structure, suggesting more complexities

of the region.

In contrast to Fig. 4.13a that shows lower *SV*-velocities at larger depths beneath the CLSC in the north, higher *P*-attenuation is mapped beneath the southern ELSC and northern VFR (Fig. 4.7) and *S*-attenuation anomalies appear to be localized with a decreasing depth from north to south (Fig. 4.8). This discrepancy partly results from the limited resolving region as *P*- and *S*-attenuation tomography both lose resolution near the CLSC and southern VFR (Fig. 4.11). However, the prominent extremely high *P*-attenuation anomalies beneath the southern ELSC is in the center of our seismic array and thus well resolved. One plausible explanation is that the melt/free fluid significantly increases bulk attenuation and thus *P*-wave attenuation, although its effects on *S*-wave velocity and attenuation are much smaller.

Our results show a sharp boundary between the highly attenuation back-arc and the low attenuation fore-arc along the Tofua arc. Although Fig. 4.11d suggests that the arc signature might be smeared, the high-attenuation anomalies at the Tofua arc are undoubtedly weaker than that in the back-arc, implying that signature of sub-arc melt in the mantle is significantly smaller in extent and intensity compared to the back-arc spreading center melt. Additionally, this sharp boundary in seismic attenuation contradicts the diffusive distribution of water flux beneath the arc as inferred by numerical models [*Harmon and Blackman*, 2010], implying that the structurally bounded water is not the primary factor controlling the seismic attenuation in the Lau Basin. This agrees with the inference by *Wei et al.* [2015], who reached the same conclusion by comparing the along-strike variations of *S*-wave velocity and water content.

4.4.3 High attenuation beneath the Fiji Plateau-Lau Ridge

Both *P*- and *S*-wave results suggest a significant layer of high attenuation beneath the Fiji

Plateau and the Lau Ridge, although its thickness is difficult to constrain. According to Section 4.3, this high-attenuation zone could be thinner with even higher attenuation than it appears in Figs. 4.7 and 4.8. This feature has been also observed by previous studies of Rayleigh wave tomography and interpreted as the hot Fijian asthenosphere with perhaps minor partial melting (Fig. 4.13) [*Wei et al.*, 2015; Chapter 3].

Besides of the high-attenuation in this region, a small area with even stronger anomalies, as well as lower *SV*-velocities, are consistently imaged beneath the northeastern Fiji Plateau and the northern Lau Ridge, where the active Taveuni Volcano exists. Geochemical analyses of trace elements suggest that the magmatism in this region rejuvenated since 3 Ma with an obvious signature of ocean island basalt (OIB) [*Gill and Whelan*, 1989]. Although abundant evidence support the idea that the Samoan mantle plume upwells to influence the whole region of Lau and Fiji [*Pearce et al.*, 2007; *Price et al.*, 2014], a more detailed geochemical study in the northwestern Lau Basin propose a possible second plume originating from deep west [*Lytle et al.*, 2012]. Nevertheless, our results of high attenuation indicate the temperature of the upper mantle beneath the northeastern Fiji Plateau and the northern Lau Ridge is higher than that of the ambient Fijian asthenosphere, potentially implying hot materials upwelling from deep mantle.

4.4.2 Q_P/Q_S variations

Low Q_P/Q_S anomalies are imaged beneath the back-arc basin, indicating significant bulk attenuation. Since the most likely mechanism of bulk attenuation is the bulk fluid flow in response to pressure gradients [*Faul and Jackson*, 2015], these low ratios suggest high porosities of melt and/or free water. One intriguing feature is a region of Q_P/Q_S as low as about 0.7 imaged near the subducting slab down to 200 km deep, potentially indicating the dehydration reactions

of the serpentinized slab at these depths. More high-resolution studies of Q_P/Q_S are needed to clarify it implications.

The relatively low ratios beneath the Fiji Plateau and Lau Ridge (about 1.8-2.0) are in agreement with the value (1.75) proposed by *Roth et al.* [1999], who estimated the average Q_P/Q_S over the whole region of Tonga, Lau, and Fiji.

4.6. Conclusions

We investigate the seismic attenuation of the upper mantle in the Tonga-Lau-Fiji region by analyzing *P* and *S* waveforms from local earthquakes. Average misfits of the t^*-inversion with varying values of α shows that α is approximately 0.3, in good agreement with the value of 0.27 suggested by models based on rock physics experiments [*Faul et al.*, 2004; *Faul and Jackson*, 2005; *Jackson and Faul*, 2010; *Faul and Jackson*, 2015]. This is consistent with the idea that the attenuation is dominated by the thermal effects associated with grain boundary sliding.

We obtain separate Q_P and Q_S models, with the Q_S model constrained by far fewer observations. The preferred Q_S model is obtained using the Q_P model as a constraint. In order to avoid potential bias due to different sampling, the Q_P/Q_S model is obtained by dividing Q_S^{-1} by Q_P^{-1} from each independent inversion using event-station pairs with both reliable $t^*_{(P)}$ and $t^*_{(S)}$ measurements. These strategies optimize the tomographic resolutions and robustness for different purposes, although the depths and thickness of the imaged features are still poorly constrained due to low vertical resolution.

Strong anomalies of high *P*- and *S*-wave attenuation are imaged beneath the Lau back-arc basin, extending deep to the west away from the subduction slab. Tests with currently available

knowledge of rock physics suggest that the extremely high attenuation, $Q_P < 30$ and $Q_S < 20$, are indicative of not only abnormally high temperature but also the presence of partial melt in the back-arc upper mantle. Additionally, low Q_P/Q_S ratios (< 1.5) are also observed beneath the Lau Basin, suggesting significant bulk attenuation due to partial melt. The inclined high-attenuation zone suggests that hot materials supplied from the Australian asthenosphere upwell into the mantle wedge, resulting in extensive decompression melting beneath the back-arc spreading centers. Due to the limited resolving region, the N-S variations of attenuation along the back-arc spreading centers are not as obvious as that of *SV*-velocities [*Wei et al.*, 2015; *Wei et al.*, In prep.]. However, both *SV*-wave velocities and *S*-wave attenuations show a trend of deeper and larger melt porosity in the north, whereas *P*-waves display highest attenuation beneath the northern VFR in the south. This discrepancy might imply more dramatic impacts of melt/free fluid on bulk attenuation than on shear attenuation.

A thick lithosphere with little attenuation is mapped beneath the Fiji Plateau and the Lau Ridge, overlying a hot asthenosphere characterized by high attenuation. A localized anomaly of high attenuation beneath the northeastern Fiji Plateau and northern Lau Ridge, along with the abnormally low *SV*-velocity from Rayleigh wave tomography [*Wei et al.*, 2015; *Wei et al.*, In prep.], indicate hot materials upwelling from deep mantle to supply the Taveuni Volcano and other active magmatism in this region.

References

Abers, G. A., K. M. Fischer, G. Hirth, D. A. Wiens, T. Plank, B. K. Holtzman, C. McCarthy, and E. Gazel (2014), Reconciling mantle attenuation-temperature relationships from seismology,

petrology, and laboratory measurements, *Geochem. Geophys. Geosyst.*, *15*(9), 3521-3542, doi: 10.1002/2014GC005444.
Aizawa, Y., A. Barnhoorn, U. H. Faul, J. D. Fitz Gerald, I. Jackson, and I. Kovács (2008), Seismic Properties of Anita Bay Dunite: an Exploratory Study of the Influence of Water, *J. Petrol.*, *49*(4), 841-855, doi: 10.1093/petrology/egn007.
Aki, K., and P. G. Richards (2002), *Quantitative Seismology*, 2 ed., p.^pp. 700, University Science Books, Sausalito, California.
Anderson, J. G., and S. E. Hough (1984), A model for the shape of the fourier amplitude spectrum of acceleration at high frequencies, *Bull. Seism. Soc. Amer.*, *74*(5), 1969-1993.
Anderson, J. G. (1986), Implication of Attenuation for Studies of the Earthquake Source, in *Earthquake Source Mechanics*, edited by S. Das, et al., pp. 311-318, American Geophysical Union, Washington, D. C.
Arai, R., and R. A. Dunn (2014), Seismological study of Lau back arc crust: Mantle water, magmatic differentiation, and a compositionally zoned basin, *Earth Planet. Sci. Lett.*, *390*, 304-317, doi: 10.1016/j.epsl.2014.01.014.
Barazangi, M., and B. Isacks (1971), Lateral variations of seismic-wave attenuation in the upper mantle above the inclined earthquake zone of the Tonga Island Arc: Deep anomaly in the upper mantle, *J. Geophys. Res.*, *76*(35), 8493-8516, doi: 10.1029/JB076i035p08493.
Barrett, R., M. W. Berry, T. F. Chan, J. Demmel, J. Donato, J. Dongarra, V. Eijkhout, R. Pozo, C. Romine, and H. Van der Vorst (1994), *Templates for the solution of linear systems: building blocks for iterative methods*, 2nd ed., SIAM, Philadelphia, PA.
Bevis, M., F. W. Taylor, B. E. Schutz, J. Recy, B. L. Isacks, S. Helu, R. Singh, E. Kendrick, J. Stowell, B. Taylor, and S. Calmantli (1995), Geodetic observations of very rapid convergence and back-arc extension at the Tonga arc, *Nature*, *374*(6519), 249-251.
Bézos, A., S. Escrig, C. H. Langmuir, P. J. Michael, and P. D. Asimow (2009), Origins of chemical diversity of back-arc basin basalts: A segment-scale study of the Eastern Lau Spreading Center, *J. Geophys. Res.*, *114*(B6), doi: 10.1029/2008jb005924.
Conder, J. A., and D. A. Wiens (2006), Seismic structure beneath the Tonga arc and Lau back-arc basin determined from joint Vp, Vp/Vs tomography, *Geochem. Geophys. Geosyst.*, *7*(3), Q03018, doi: 10.1029/2005gc001113.
Cooper, R. F. (2002), Seismic Wave Attenuation: Energy Dissipation in Viscoelastic Crystalline Solids, *Reviews in Mineralogy and Geochemistry*, *51*(1), 253-290, doi: 10.2138/gsrmg.51.1.253.
Crawford, W. C., J. A. Hildebrand, L. M. Dorman, S. C. Webb, and D. A. Wiens (2003), Tonga Ridge and Lau Basin crustal structure from seismic refraction data, *J. Geophys. Res.*, *108*(B4), 2195, doi: 10.1029/2001jb001435.
Das, R., H. R. Wason, and M. L. Sharma (2011), Global regression relations for conversion of surface wave and body wave magnitudes to moment magnitude, *Nat Hazards*, *59*(2), 801-810, doi: 10.1007/s11069-011-9796-6.
Dunn, R. A., and F. Martinez (2011), Contrasting crustal production and rapid mantle transitions beneath back-arc ridges, *Nature*, *469*(7329), 198-202, doi: 10.1038/nature09690.
Dunn, R. A., F. Martinez, and J. A. Conder (2013), Crustal construction and magma chamber properties along the Eastern Lau Spreading Center, *Earth Planet. Sci. Lett.*, *371–372*(0), 112-124, doi: 10.1016/j.epsl.2013.04.008.
Escrig, S., A. Bézos, S. L. Goldstein, C. H. Langmuir, and P. J. Michael (2009), Mantle source variations beneath the Eastern Lau Spreading Center and the nature of subduction

components in the Lau basin–Tonga arc system, *Geochem. Geophys. Geosyst.*, *10*(4), doi: 10.1029/2008gc002281.
Faul, U., and I. Jackson (2015), Transient Creep and Strain Energy Dissipation: An Experimental Perspective, *Annu. Rev. Earth Planet. Sci.*, *43*(1), 541-569, doi: doi:10.1146/annurev-earth-060313-054732.
Faul, U. H., J. D. Fitz Gerald, and I. Jackson (2004), Shear wave attenuation and dispersion in melt-bearing olivine polycrystals: 2. Microstructural interpretation and seismological implications, *J. Geophys. Res.*, *109*(B6), B06202, doi: 10.1029/2003jb002407.
Faul, U. H., and I. Jackson (2005), The seismological signature of temperature and grain size variations in the upper mantle, *Earth Planet. Sci. Lett.*, *234*(1-2), 119-134.
Gill, J., and P. Whelan (1989), Postsubduction Ocean Island Alkali Basalts in Fiji, *J. Geophys. Res.*, *94*(B4), 4579-4588, doi: 10.1029/JB094iB04p04579.
Hammond, W. C., and E. D. Humphreys (2000), Upper mantle seismic wave attenuation: Effects of realistic partial melt distribution, *J. Geophys. Res.*, *105*(B5), 10987-10999, doi: 10.1029/2000jb900042.
Harmon, N., and D. K. Blackman (2010), Effects of plate boundary geometry and kinematics on mantle melting beneath the back-arc spreading centers along the Lau Basin, *Earth Planet. Sci. Lett.*, *298*(3-4), 334-346, doi: 10.1016/j.epsl.2010.08.004.
Hayes, G. P., D. J. Wald, and R. L. Johnson (2012), Slab1.0: A three-dimensional model of global subduction zone geometries, *J. Geophys. Res.*, *117*(B1), B01302, doi: 10.1029/2011jb008524.
Helmberger, D. V. (1974), Generalized ray theory for shear dislocations, *Bull. Seism. Soc. Amer.*, *64*(1), 45-64.
Hirschmann, M. M. (2006), WATER, MELTING, AND THE DEEP EARTH H_2O CYCLE, *Annu. Rev. Earth Planet. Sci.*, *34*(1), 629-653, doi: doi:10.1146/annurev.earth.34.031405.125211.
Holtzman, B. K., and J. M. Kendall (2010), Organized melt, seismic anisotropy, and plate boundary lubrication, *Geochem. Geophys. Geosyst.*, *11*, Q0AB06, doi: 10.1029/2010gc003296.
Hough, S. E. (1996), Observational constraints on earthquake source scaling: understanding the limits in resolution, *Tectonophysics*, *261*(1–3), 83-95, doi: 10.1016/0040-1951(96)00058-3.
Hough, S. E., J. M. Lees, and F. Monastero (1999), Attenuation and source properties at the Coso Geothermal Area, California, *Bull. Seism. Soc. Amer.*, *89*(6), 1606-1619.
International Seismological Centre (2013), Reviewed ISC Bulletin, http://www.isc.ac.uk, Internatl. Seis. Cent., Thatcham, United Kingdom.
Jackson, I., J. D. Fitz Gerald, U. H. Faul, and B. H. Tan (2002), Grain-size-sensitive seismic wave attenuation in polycrystalline olivine, *J. Geophys. Res.*, *107*(B12), 2360, doi: 10.1029/2001jb001225.
Jackson, I., and U. H. Faul (2010), Grainsize-sensitive viscoelastic relaxation in olivine: Towards a robust laboratory-based model for seismological application, *Phys. Earth Planet. In.*, *183*(1-2), 151-163.
Jacobs, A. M., A. J. Harding, and G. M. Kent (2007), Axial crustal structure of the Lau back-arc basin from velocity modeling of multichannel seismic data, *Earth Planet. Sci. Lett.*, *259*(3-4), 239-255, doi: 10.1016/j.epsl.2007.04.021.

Kanamori, H., and G. S. Stewart (1976), Mode of the strain release along the Gibbs fracture zone, Mid-Atlantic ridge, *Phys. Earth Planet. In.*, *11*(4), 312-332, doi: 10.1016/0031-9201(76)90018-2.

Karato, S.-I. (2003), Mapping water content in the upper mantle, in *Inside the Subduction Factory*, edited by J. M. Eiler, pp. 135-152, American Geophysical Union, Washington, DC.

Karato, S.-i. (2012), On the origin of the asthenosphere, *Earth Planet. Sci. Lett.*, *321-322*, 95-103, doi: 10.1016/j.epsl.2012.01.001.

Kelley, K. A., T. Plank, T. L. Grove, E. M. Stolper, S. Newman, and E. Hauri (2006), Mantle melting as a function of water content beneath back-arc basins, *J. Geophys. Res.*, *111*(B9), B09208, doi: 10.1029/2005jb003732.

Lees, J. M., and J. Park (1995), Multiple-taper spectral analysis: A stand-alone C-subroutine, *Computers & Geosciences*, *21*(2), 199-236, doi: 10.1016/0098-3004(94)00067-5.

Lytle, M. L., K. A. Kelley, E. H. Hauri, J. B. Gill, D. Papia, and R. J. Arculus (2012), Tracing mantle sources and Samoan influence in the northwestern Lau back-arc basin, *Geochem. Geophys. Geosyst.*, *13*(10), Q10019, doi: 10.1029/2012GC004233.

Martinez, F., and B. Taylor (2002), Mantle wedge control on back-arc crustal accretion, *Nature*, *416*(6879), 417-420, doi: 10.1038/416417a.

Martinez, F., B. Taylor, E. T. Baker, J. A. Resing, and S. L. Walker (2006), Opposing trends in crustal thickness and spreading rate along the back-arc Eastern Lau Spreading Center: Implications for controls on ridge morphology, faulting, and hydrothermal activity, *Earth Planet. Sci. Lett.*, *245*(3-4), 655-672, doi: 10.1016/j.epsl.2006.03.049.

Mavko, G., and A. Nur (1975), Melt squirt in the asthenosphere, *J. Geophys. Res.*, *80*(11), 1444-1448, doi: 10.1029/JB080i011p01444.

McCarthy, C., Y. Takei, and T. Hiraga (2011), Experimental study of attenuation and dispersion over a broad frequency range: 2. The universal scaling of polycrystalline materials, *J. Geophys. Res.*, *116*(B9), B09207, doi: 10.1029/2011jb008384.

McKenzie, D. (2000), Constraints on melt generation and transport from U-series activity ratios, *Chemical Geology*, *162*(2), 81-94, doi: 10.1016/S0009-2541(99)00126-6.

Menke, W. (2012), Chapter 5 - Solution of the Linear, Gaussian Inverse Problem, Viewpoint 3: Maximum Likelihood Methods, in *Geophysical Data Analysis: Discrete Inverse Theory (Third Edition)*, edited by W. Menke, pp. 89-114, Academic Press, Boston.

Menke, W. (2014), Review of the Generalized Least Squares Method, *Surveys in Geophysics*, 1-25, doi: 10.1007/s10712-014-9303-1.

Miller, K. J., W.-l. Zhu, L. G. J. Montési, and G. A. Gaetani (2014), Experimental quantification of permeability of partially molten mantle rock, *Earth Planet. Sci. Lett.*, *388*, 273-282, doi: 10.1016/j.epsl.2013.12.003.

O'Connell, R. J., and B. Budiansky (1977), Viscoelastic properties of fluid-saturated cracked solids, *J. Geophys. Res.*, *82*(36), 5719-5735, doi: 10.1029/JB082i036p05719.

Pearce, J. A., M. Ernewein, S. H. Bloomer, L. M. Parson, B. J. Murton, and L. E. Johnson (1994), Geochemistry of Lau Basin volcanic rocks: influence of ridge segmentation and arc proximity, *Geological Society, London, Special Publications*, *81*(1), 53-75, doi: 10.1144/gsl.sp.1994.081.01.04.

Pearce, J. A., P. D. Kempton, and J. B. Gill (2007), Hf-Nd evidence for the origin and distribution of mantle domains in the SW Pacific, *Earth Planet. Sci. Lett.*, *260*(1-2), 98-114, doi: 10.1016/j.epsl.2007.05.023.

Pozgay, S. H., D. A. Wiens, J. A. Conder, H. Shiobara, and H. Sugioka (2009), Seismic attenuation tomography of the Mariana subduction system: Implications for thermal structure, volatile distribution, and slow spreading dynamics, *Geochem. Geophys. Geosyst.*, *10*(4), Q04X05, doi: 10.1029/2008gc002313.

Price, A. A., M. G. Jackson, J. Blichert-Toft, P. S. Hall, J. M. Sinton, M. D. Kurz, and J. Blusztajn (2014), Evidence for a broadly distributed Samoan-plume signature in the northern Lau and North Fiji Basins, *Geochem. Geophys. Geosyst.*, *15*(4), 986-1008, doi: 10.1002/2013GC005061.

Roth, E. G., D. A. Wiens, L. M. Dorman, J. Hildebrand, and S. C. Webb (1999), Seismic attenuation tomography of the Tonga-Fiji region using phase pair methods, *J. Geophys. Res.*, *104*(B3), 4795-4809, doi: 10.1029/1998jb900052.

Rychert, C. A., K. M. Fischer, G. A. Abers, T. Plank, E. Syracuse, J. M. Protti, V. Gonzalez, and W. Strauch (2008), Strong along-arc variations in attenuation in the mantle wedge beneath Costa Rica and Nicaragua, *Geochem. Geophys. Geosyst.*, *9*(10), Q10S10, doi: 10.1029/2008gc002040.

Schmeling, H. (1985), Numerical models on the influence of partial melt on elastic, anelastic and electric properties of rocks. Part I: elasticity and anelasticity, *Phys. Earth Planet. In.*, *41*(1), 34-57, doi: 10.1016/0031-9201(85)90100-1.

Stachnik, J. C., G. A. Abers, and D. H. Christensen (2004), Seismic attenuation and mantle wedge temperatures in the Alaska subduction zone, *J. Geophys. Res.*, *109*(B10), B10304, doi: 10.1029/2004jb003018.

Tarantola, A., and B. Valette (1982), Generalized Nonlinear Problems Solved Using the Least Squares Criterion, *Rev. Geophys. Sp. Phys.*, *20*(2), 219-232, doi: 10.1029/RG020i002p00219.

Turner, I. M., C. Peirce, and M. C. Sinha (1999), Seismic imaging of the axial region of the Valu Fa Ridge, Lau Basin—the accretionary processes of an intermediate back-arc spreading ridge, *Geophys. J. Int.*, *138*(2), 495-519, doi: 10.1046/j.1365-246X.1999.00883.x.

Um, J., and C. Thurber (1987), A fast algorithm for two-point seismic ray tracing, *Bull. Seism. Soc. Amer.*, *77*(3), 972-986.

van der Lee, S., and D. A. Wiens (2006), Seismological constraints on Earth's deep water cycle, in *Earth's Deep Water Cycle*, edited by S. D. Jacobsen and S. v. d. Lee, pp. 13-27, American Geophysical Union, Washington, DC.

Wei, S. S., D. A. Wiens, Y. Zha, T. Plank, S. C. Webb, D. K. Blackman, R. A. Dunn, and J. A. Conder (2015), Seismic evidence of effects of water on melt transport in the Lau back-arc mantle, *Nature*, *518*(7539), 395-398, doi: 10.1038/nature14113.

Wiens, D. A., J. A. Conder, and U. H. Faul (2008), The Seismic Structure and Dynamics of the Mantle Wedge, *Annu. Rev. Earth Planet. Sci.*, *36*(1), 421-455, doi: 10.1146/annurev.earth.33.092203.122633.

Willemann, R. J. (1999), Regional Thresholds of the ISC Bulletin, *Seismol. Res. Lett.*, *70*(3), 313-321, doi: 10.1785/gssrl.70.3.313.

Zha, Y., S. C. Webb, and W. Menke (2013), Determining the orientations of ocean bottom seismometers using ambient noise correlation, *Geophys. Res. Lett.*, *40*(14), 3585-3590, doi: 10.1002/grl.50698.

Zha, Y., S. C. Webb, S. S. Wei, D. A. Wiens, D. K. Blackman, W. Menke, R. A. Dunn, and J. A. Conder (2014), Seismological imaging of ridge–arc interaction beneath the Eastern Lau Spreading Center from OBS ambient noise tomography, *Earth Planet. Sci. Lett.*, *408*, 194-206, doi: 10.1016/j.epsl.2014.10.019.

Zhu, W., G. A. Gaetani, F. Fusseis, L. G. J. Montési, and F. De Carlo (2011), Microtomography of Partially Molten Rocks: Three-Dimensional Melt Distribution in Mantle Peridotite, *Science*, *332*(6025), 88-91, doi: 10.1126/science.1202221.

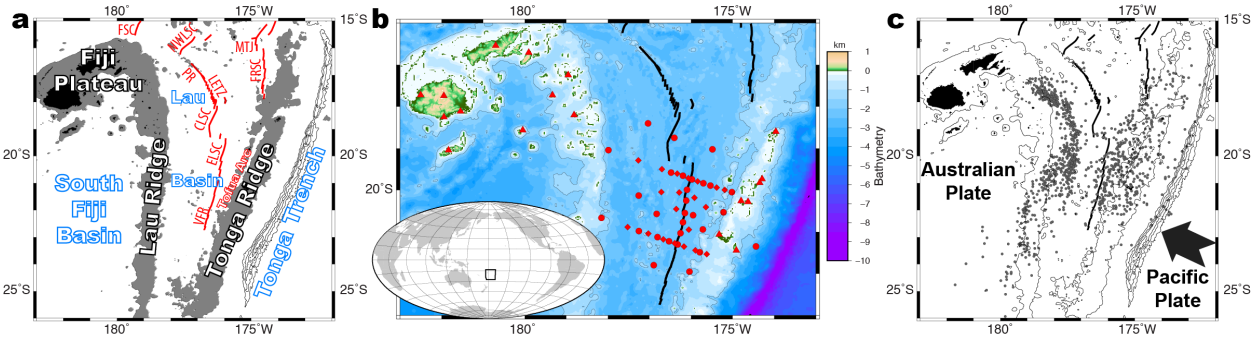

Figure 4.1. Maps of the Tonga-Lau-Fiji region.

(a) Tectonic map with back-arc spreading centers (red lines). The Pacific plate subducts beneath the Tonga trench (delineated by bathymetric contours of 7, 8, 9, and 10 km) from the southeast. Land areas are filled with black, whereas areas with bathymetry shallower than 1.5 km are shaded in gray. CLSC, Central Lau Spreading Centre; ELSC, East Lau Spreading Centre; FRSC, Fonualei Rift and Spreading Centre; FSC, Futuna Spreading Centre; LETZ, Extensional Transform Zone; MTJ, Mangatolu Triple Junction; NWLSC, Northwest Lau Spreading Centre; NELB, northeastern Lau Basin; VFR, Valu Fa Ridge. (b) Seismic stations (red dots for WHOI OBSs, red diamonds for LDEO OBSs, and red triangles for island-based stations) used in this study. Back-arc spreading centers are shown as black curves. Inset display the study region in a global map. (c) Earthquakes (black dots) used in this study, though not all of them are recorded well enough to calculate reliable t^* measurements. Land areas are filled with black, whereas bathymetries of 1.5, 7, 8, 9, and 10 km are contoured.

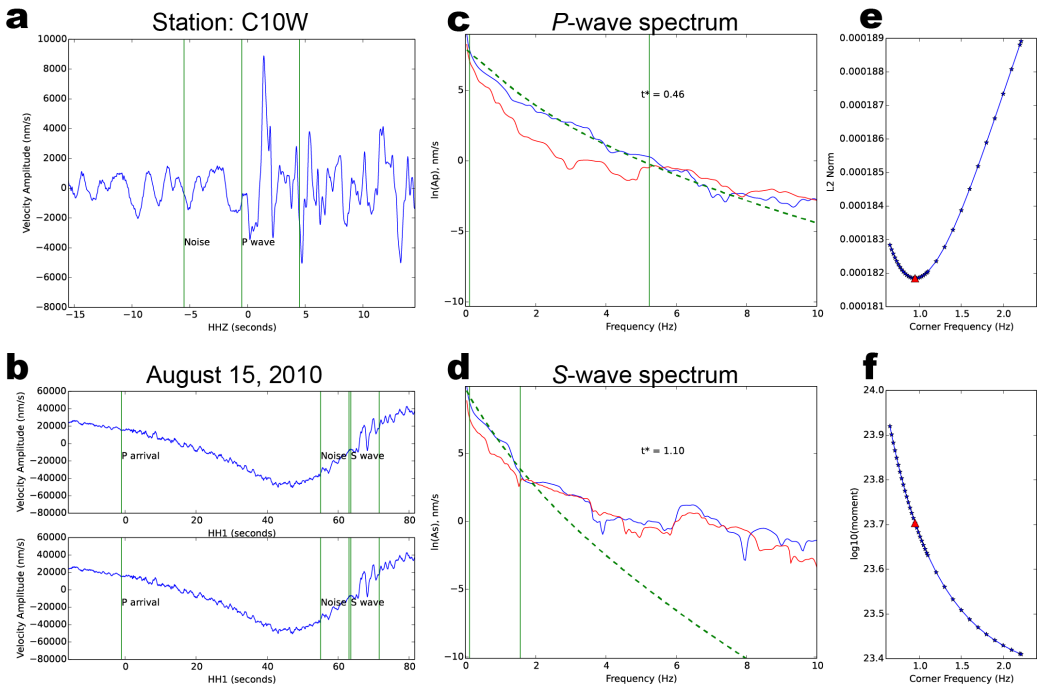

Figure 4.2. Example seismograms recorded at OBS C10W and spectra for *P* and *S* waves. (a) *P* wave recorded on the vertical channel. Green bars bound the windows of the *P* wave and background noise preceding. The earthquake was on August 15th, 2010 (m_b = 4.7) and located at 22.1˚S 179.3˚W. (b) S wave recorded on two horizontal channels. The leftmost green bar indicates the *P* arrival, whereas other green bars bound the windows of the S wave and background noise preceding. (c) Spectra of the *P* wave (blue) and the noise (red) shown in Fig. 4.2a. Green bars bound the frequency band used in the *t**-inversion. Green dashed curve shows the synthetic spectrum defined by the inverted $t^*_{(P)}$ = 0.46. (d) Spectra of the *S* wave (blue) and the noise (red) shown in Fig. 4.2b. Green bars bound the frequency band used in the *t**-inversion. Green dashed curve shows the synthetic spectrum defined by the inverted $t^*_{(S)}$ = 1.10. (e) Misfit of the *t**-inversion as a function of corner frequency. Red triangle represents the best fc corresponding to the final results of *t**. (f) Inverted seismic moment as a function of corner frequency.

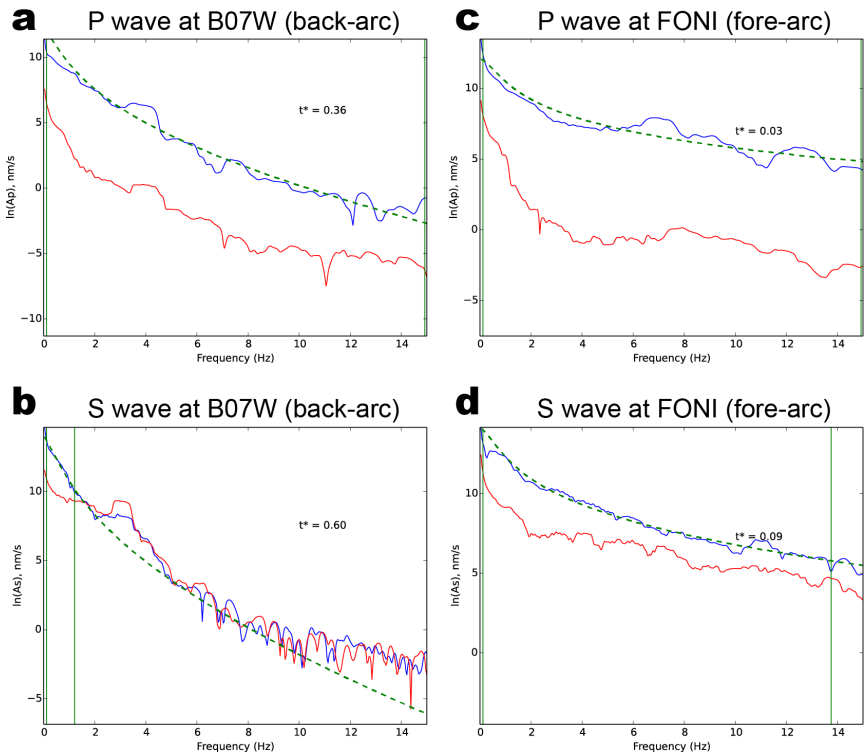

Figure 4.3. Example *P*- and *S*-wave spectra recorded at OBS B07W in the Lau back-arc basin (a, b) and at station FONI on the Tonga fore-arc ridge (c, d).

The event occurred on April 10th, 2010 (m_b = 5.5) and was located at 20.1˚S 175.8˚W. Spectra are plotted in the same manner as Figs. 4.2c and 4.2b. Seismic signals are more attenuated in the back-arc than in the fore-arc, and attenuation is higher on the S wave. Only a small frequency band records the *S* wave above the noise level for the back-arc station.

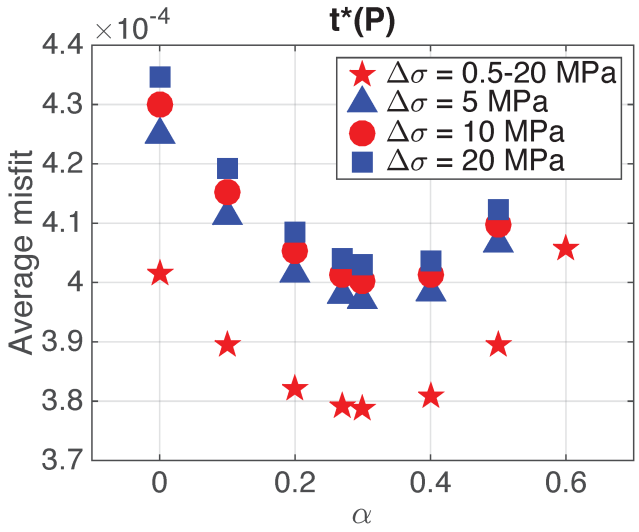

Figure 4.4. Average L_2 norm misfit of *t-inversions over all events as functions of α value and stress drop $\Delta\sigma$.**

The α value corresponding to the minimum misfit is close to the value suggested by experimental constraints (0.27) [*Jackson et al.*, 2002; *Jackson and Faul*, 2010].

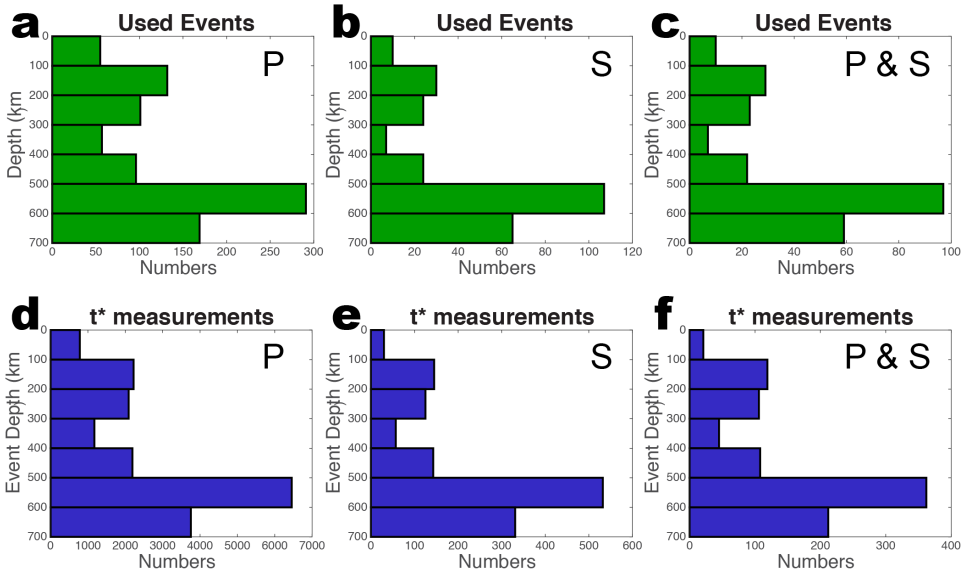

Figure 4.5. Depth distributions of earthquakes (a-c) and source events of *t measurements (d-f) used for inversions of Q_P (Case 1), Q_S (Case 3), and Q_P/Q_S (Case 4).**

Most event-station pairs with a good $t^*_{(S)}$ measurement usually also have a good $t^*_{(P)}$ measurement. But a few exceptions lead to fewer events for the Q_P/Q_S inversion compared to the Q_S inversion.

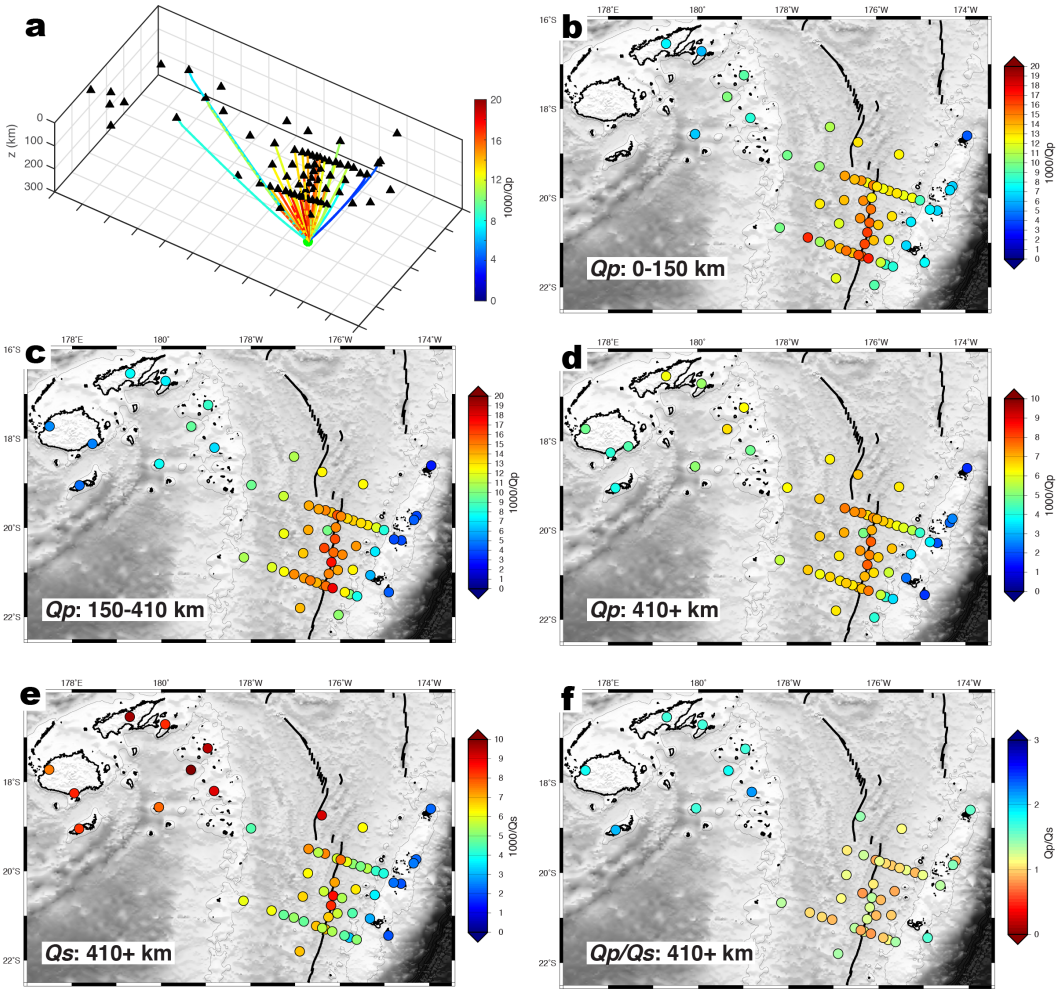

Figure 4.6. Average attenuation along event-station pairs.

(a) *P* waves of an earthquake (green dot) recorded at seismic stations (black triangles). The event occurred on December 20th, 2010 (m_b = 3.9) and was located at 21.3˚S 176.2˚W. Raypaths are color-coded by the path-averaged attenuation along each path. (b) Mean value of the average *P*-wave attenuation at each station over all events shallower than 150 km. Only stations with more than 2 measurements are plotted. (c) Same as (b) for events between 150- and 410-km deep. (d) Same as (b) for events deeper than 410 km. (c) Same as (d) for *S*-wave attenuation. (d) Same as (d) for average Q_P/Q_S.

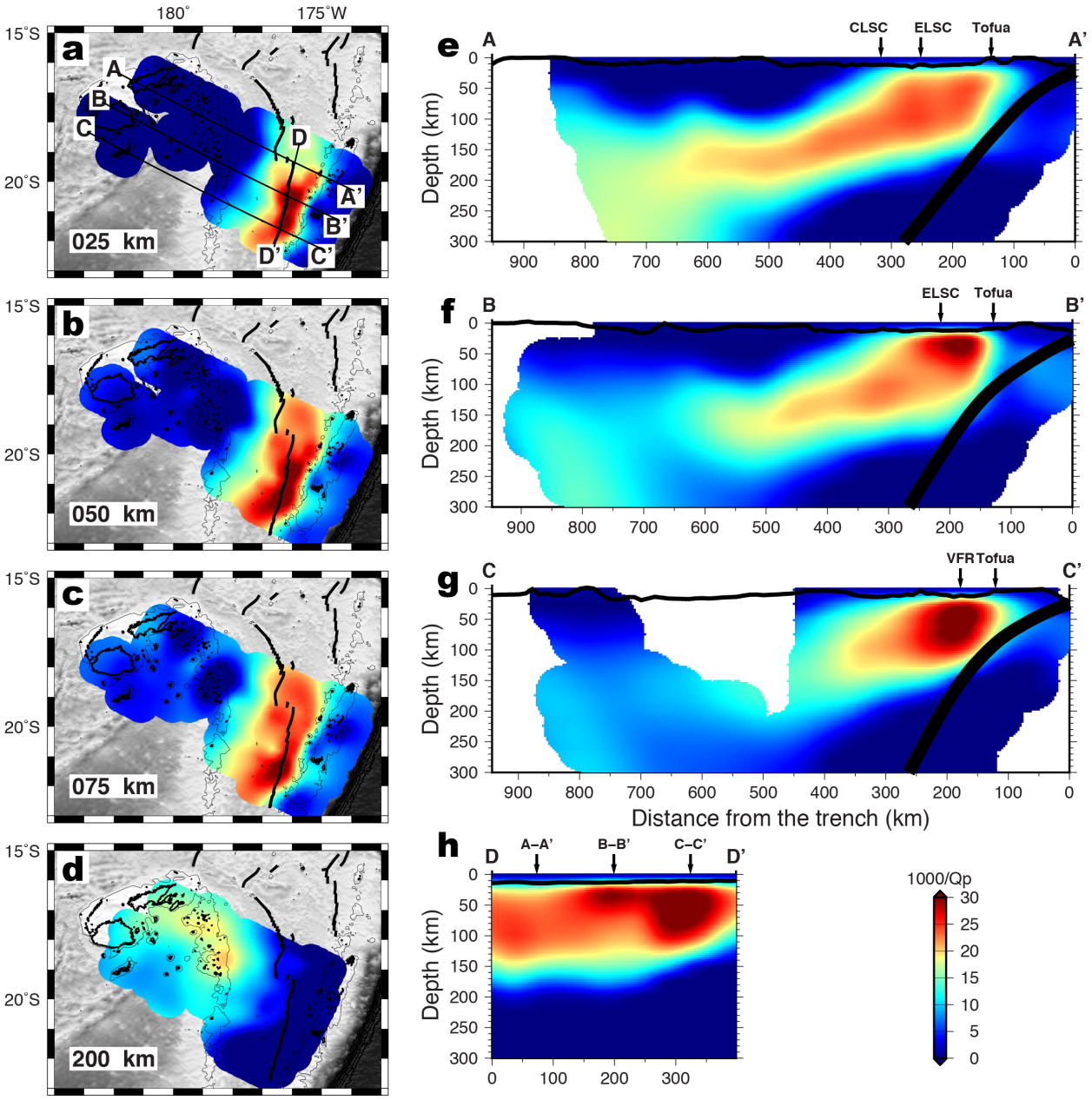

Figure 4.7. *P*-wave attenuation in map view (a-d) and cross-sections (e-h).

The 1000 m bathymetric contour is shown in the map views. Topography and bathymetry are plotted on the top of the cross-sections with a 5-times exaggeration. Black bold curves delineate the surface of the subducting slab in the Slab 1.0 model [*Hayes et al.*, 2012].

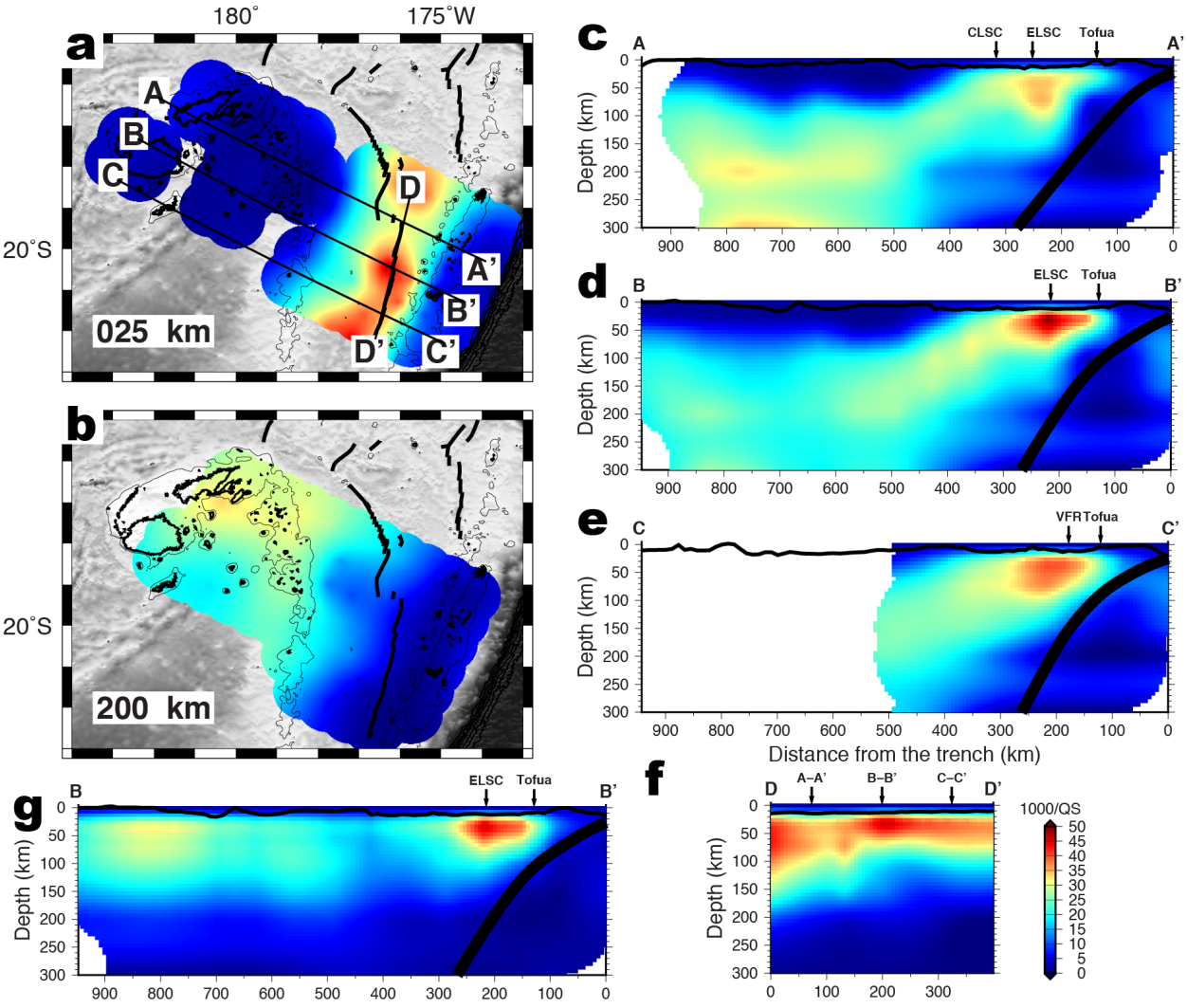

Figure 4.8. *S*-wave attenuation in map view (a, b) and cross-sections (c-f).

(a-f) are plotted in the same manner as Fig. 4.7. (g) S-wave attenuation inverted independently. The location of the cross-section is the same as (d). Because of little vertical resolution beneath the Fiji Plateau, high-attenuation anomalies are wrongly mapped at shallow depths with stronger amplitudes.

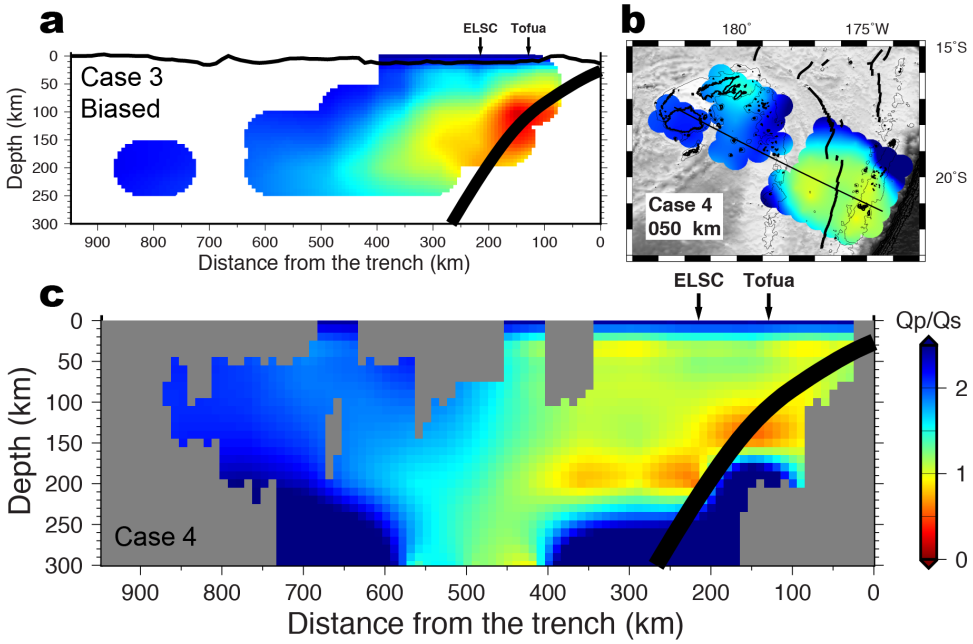

Figure 4.9. Q_P/Q_S results.

(a) Q_P/Q_S is inverted from $t^*_{(S)}$ and the Q_P model (Case 3). (b,c) Q_P/Q_S is inverted using only t* measurements along the same raypaths (Case 4). Due to the different sampling of *P* and *S* waves, Case 3 may underestimate Q_P/Q_S near the slab. Black line in Fig. 4.9b illustrates the location of the cross-section in Figs. 4.9a and 4.9c.

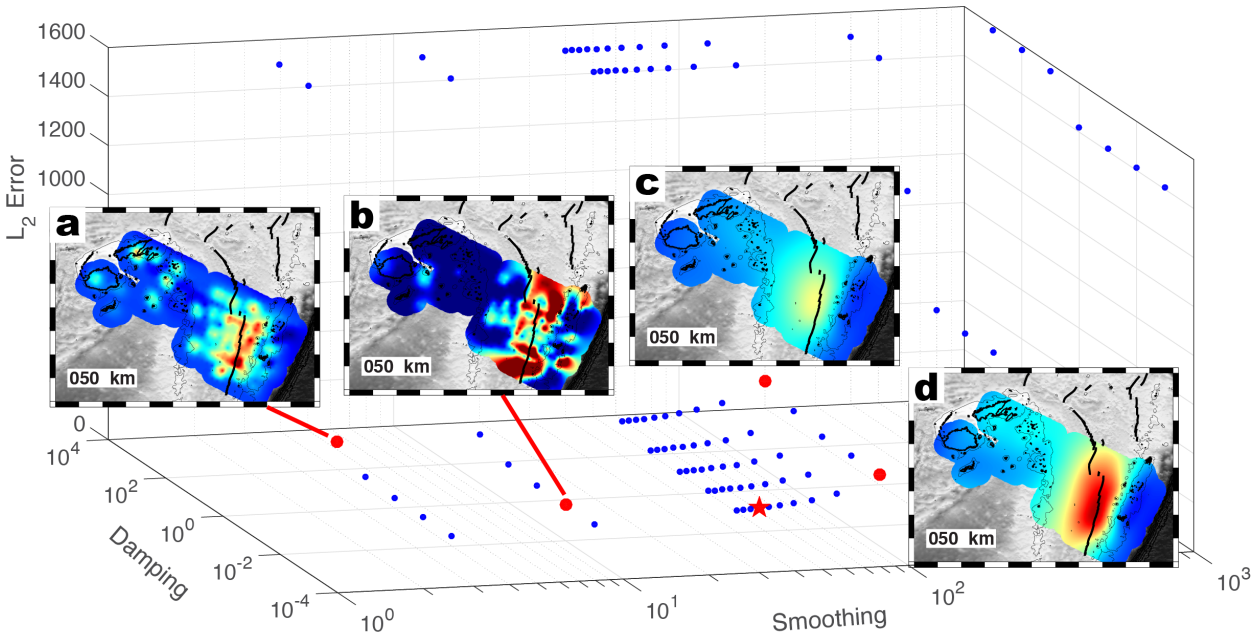

Figure 4.10. Misfit of Q_P-inversion (blue or red dots) with varying damping and smoothing coefficients.

Results corresponding to selected parameters (red dots) are shown as examples. Red star represents the parameters chosen for the final results. Larger damping coefficients (a, c) lead to relatively smaller anomaly amplitudes, whereas larger smoothing coefficients (c, d) result in relatively smoother models but greater misfit.

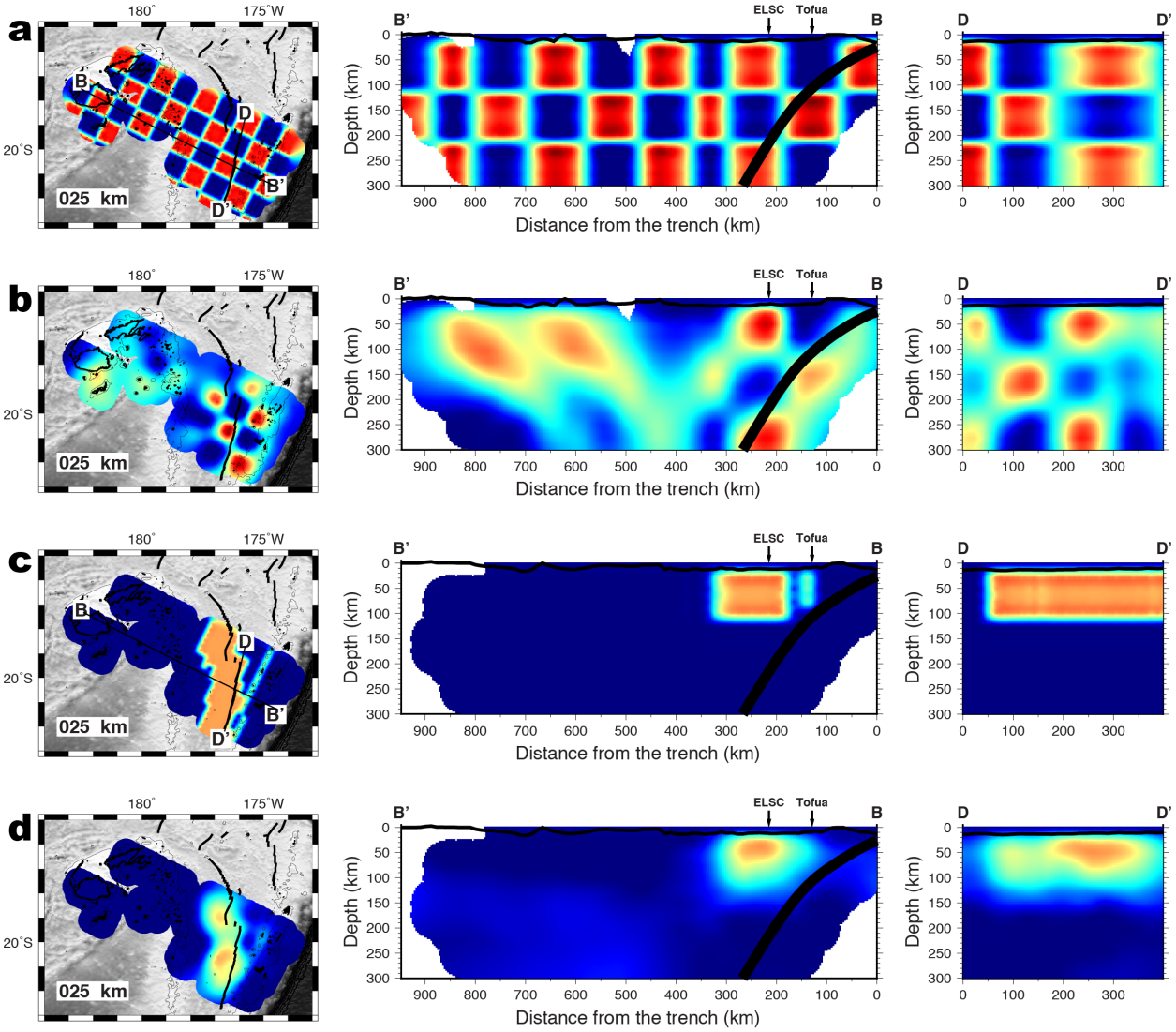

Figure 4.11. Synthetic tests of Q_P-inversion.

(a) Input model of the checkerboard test. Black lines in map view illustrate the locations of the cross-sections. (b) Output model of (a). (c) Input model of a synthetic high-attenuation zone in the back-arc. Black lines in map view illustrate the locations of the cross-sections. (b) Output model of (c).

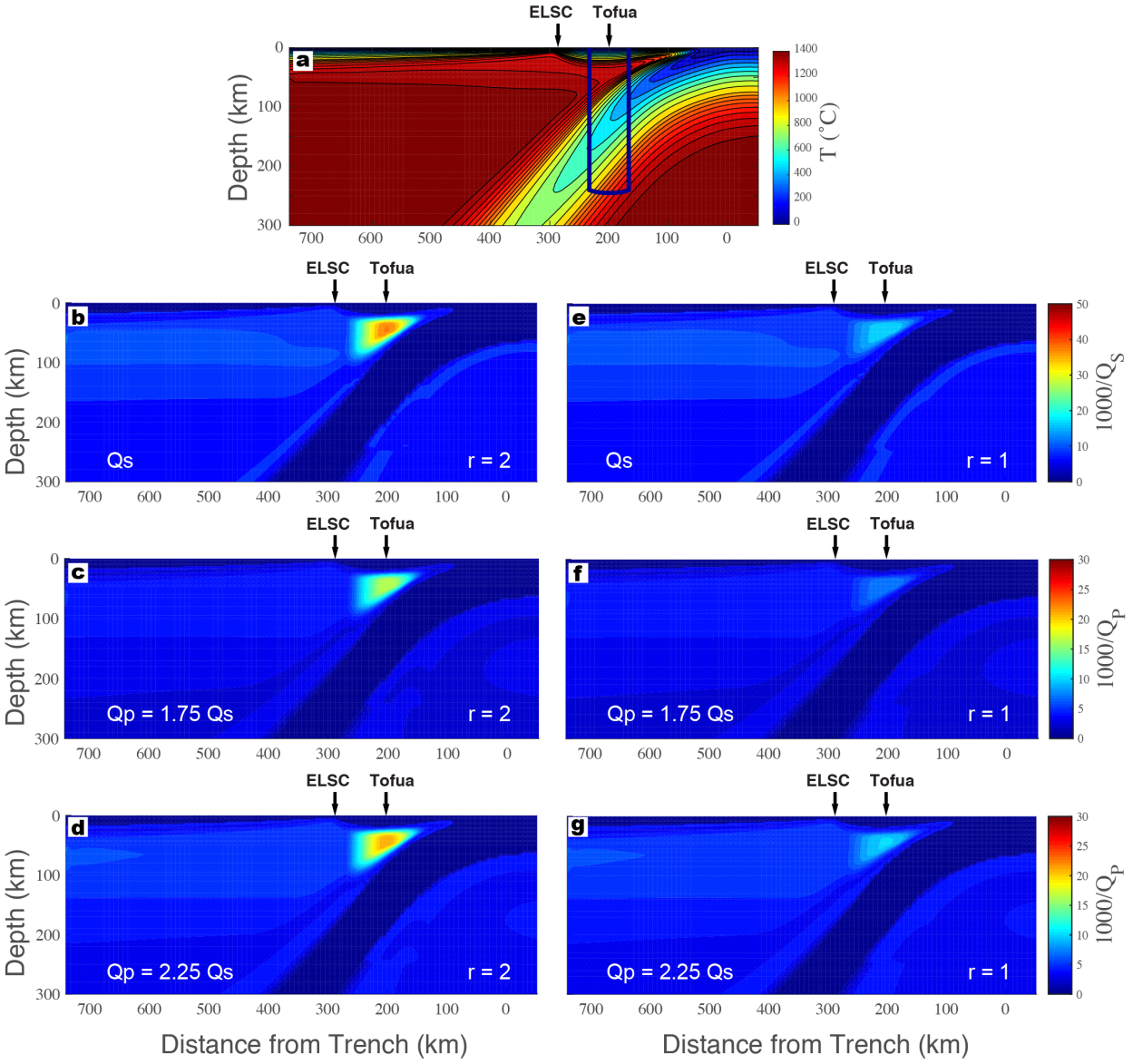

Figure 4.12. Cross-sections of predicted *Q* models for the ELSC.

(a) Thermal model of the ELSC by *Harmon and Blackman* [2010]. The blue column contours 0.1% water content in the input model. (b) Predicted Q_S model. Calculations are based on Fig. 4.12a, extended Burgers model [*Jackson and Faul*, 2010], and effects of water ($r = 2$) [*Karato*, 2012]. (c) Q_P model converted from (b) assuming $Q_P/Q_S = 1.75$ [*Roth et al.*, 1999]. (d) Q_P model converted from (b) assuming $Q_P/Q_S = 2.25$ (no bulk attenuation). (e-g) Same as (b-d) except $r = 1$. Notice the color scale is the same in Figs. 4.7 and 4.8.

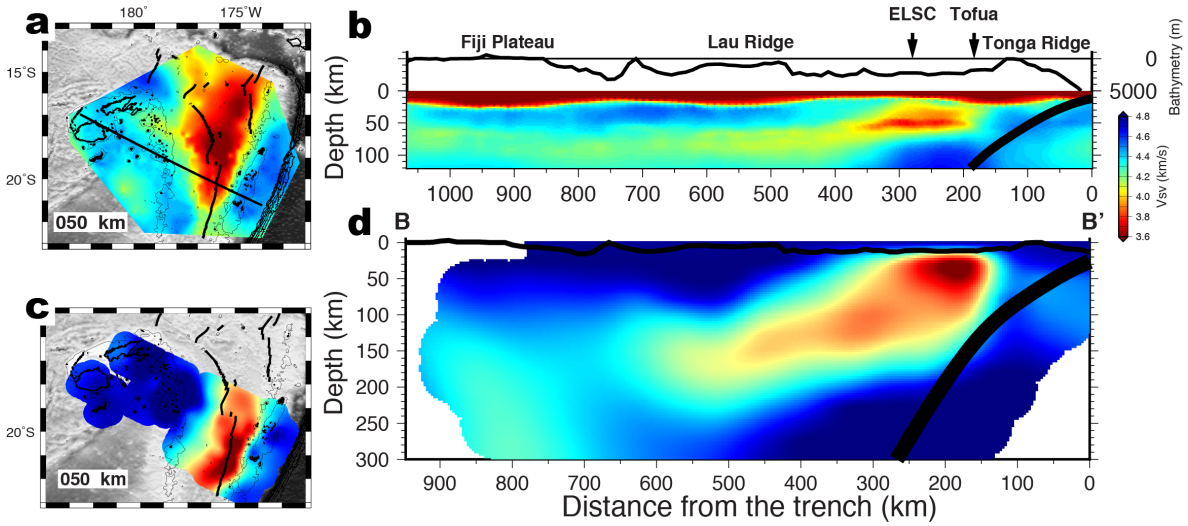

Figure 4.13. Comparisons between *SV*-velocity structure from Rayleigh wave tomography (Chapter 3) and *P*-wave attenuation.

(a) Map view at the depth of 50 km plotted in the same manner as Fig. 4.7a. (b) Cross-section along the black line in (a) plotted in the same manner as Fig. 4.7e. *P*-wave attenuation images (c-d) are from Fig. 4.7. The depth of 120 km is shown by a dashed black line.

Table 4.1. Cases for *Q* inversion.

The last column indicates the type of final results for further discussions.

Case	Input	Data amount	Equation	Inversion algorithm	Model parameter	Output	**Final**
1	$t^*_{(P)}$	18660	4.9	Biconjugate-gradient with iterations	Q_P^{-1}	Q_P	$\boldsymbol{Q_P}$
2	$t^*_{(S)}$	1363	4.9	Non-negative least square	Q_S^{-1}	Q_S	
3	Q_P^{-1} from Case 1 and $t^*_{(S)}$	1363	4.10	Damped SVD	Q_P/Q_S	Q_P/Q_S and Q_S	$\boldsymbol{Q_S}$
4	$t^*_{(P)}$ and $t^*_{(S)}$ of same event-station pair	973	4.9	Non-negative least square	Q_P^{-1} and Q_S^{-1}	Q_P/Q_S	$\boldsymbol{Q_P/Q_S}$

Chapter 5

Intermediate-depth double seismic zone in Tonga and relationships to slab thermal and stress states

Abstract

Intermediate-depth earthquakes in the Tonga subduction zone are precisely relocated using data from a local ocean bottom seismograph array as well as regional and global seismic stations. Results reveal a double seismic zone in the northern part of the slab within a depth range of 70-300 km. Focal mechanisms show a downdip compressional upper plane and a downdip tensional lower plane with a separation of about 30 km. The seismogenic zone becomes shallower and thinner and forms a single plane dominated by downdip compression south of 21°S. The lower end of the double seismic zone in Tonga is significantly deeper than that in Japan and in other slabs worldwide. As the Tonga slab is inferred to be the coldest in the world due to its high convergence rate, this suggests that the thermal structure of the slab controls the maximum depth of the double seismic zone. Additionally, an inclined stripe of high seismicity is observed at depths of 200-300 km, with many earthquakes in this region occurring on between the two seismicity planes. The depth of this seismicity decreases linearly from north to south, in good correlation with the convergence rate. Numerical thermal models reveal that these events

occurred at various pressures but a nearly constant temperature. We propose that this stripe is caused by dehydration of the uppermost slab mantle when it reaches the temperature of about 550 ˚C. However, the disappearance of the double seismic zone to the south coincides with the change in slab curvature, suggesting that the slab stress states rather than dehydration reactions control the activity of the lower plane.

5.1. Introduction

Intermediate-depth earthquakes, occurring at depths of 70-300 km, are observed at most subduction zones though their mechanism remains controversial, as the pressure (*P*) and temperature (*T*) should be too high to allow brittle failure. Various mechanisms have been proposed to explain these earthquakes: (1) dehydration embrittlement in which rocks undergo sudden weakening and embrittlement during their dehydration [e.g. *Kirby*, 1995; *Kirby et al.*, 1996; *Jung et al.*, 2004], (2) plastic shear instability in which rapid generation of heat triggers melting and allows runaway shear failure [e.g. *Hobbs and Ord*, 1988; *Kelemen and Hirth*, 2007], and (3) transformational faulting where phase transformations lead to elastic failures [e.g. *Kao and Liu*, 1995]. After decades of study, it is clear that the distribution of intermediate-earthquakes coincides well with locations where dehydration of one or more minerals are expected to occur [e.g. *Peacock*, 2001; *Hacker et al.*, 2003; *Yamasaki and Seno*, 2003; *Brudzinski et al.*, 2007]. These observations suggest that intermediate-depth earthquakes may be triggered by dehydration of crustal and mantle rocks, increasing the pore fluid pressure and hence reducing the confining pressure.

It is worthwhile to note that 'dehydration embrittlement' *sensu stricto* refers to brittle failure that occurs *in situ* and simultaneous with the dehydration, which has been only observed in few experiments [*Lee and Kirby*, 1984] and is challenged by recent experimental results [*Proctor and Hirth*, 2015]. *van Keken et al.* [2012] state that the presence of fluids, possibly due to dehydration, is more important than dehydration embrittlement itself. We thus use 'fluid-related embrittlement' to describe the mechanism by which the increase of pore fluid pressure within the subducting slab triggers earthquakes, and assume that the dehydration of several kinds of hydrous minerals are the most likely sources of the free fluids. This mechanism therefore has

important implications for mantle water budget and the global water cycle [*Hacker*, 2008; *van Keken et al.*, 2011]. However, the detailed processes of intermediate-depth earthquake nucleation, such as whether the increase in pore fluid pressure will result in reactivation of outer rise faults or generating new faults, remains controversial [*Jung et al.*, 2004; *Billen et al.*, 2007; *Warren et al.*, 2007].

More intriguingly, double seismic zones (DSZ), in which intermediate-depth earthquakes occur along two layers parallel to the dip of the subducting slab and separated by 20-40 km, have been observed in some subduction zones [e.g. *Umino and Hasegawa*, 1975; *Engdahl and Scholz*, 1977; *Hasegawa et al.*, 1978; *Kawakatsu*, 1985; *McGuire and Wiens*, 1995]. The upper plane is usually confined in the slab crust and uppermost mantle with downdip compressional stresses, whereas the lower plane is about 20-40 km deep from the slab surface with downdip tensional events. These phenomena can be generally explained by unbending and fluid-related embrittlement, so that the upper plane is attributed to the phase transitions from basalt to eclogite as well as other dehydration reactions in the crust [e.g. *Peacock*, 2001; *Wang*, 2002; *Hacker et al.*, 2003; *Yamasaki and Seno*, 2003; *Brudzinski et al.*, 2007].

The lower zone seismicity is more difficult to explain, and has been attributed to dehydration of antigorite in the slab mantle, although many studies doubt the presence of hydrated minerals at the appropriate depth in the mantle [e.g. *Kelemen and Hirth*, 2007]. Additionally, numerical modeling suggest that negative pressure gradients due to unbending can drive the water from dehydration reactions into the core of the slab [*Faccenda and Mancktelow*, 2010; *Faccenda et al.*, 2012]. More detailed studies in northeastern Japan and Alaska suggest that the upper plane of the DSZ may also extend into the uppermost mantle, corresponding to the breakdown of antigorite or chlorite [*Kita et al.*, 2010b; *Abers et al.*, 2013]. Since these dehydration reactions

occur under certain *p-T* conditions, the distribution of intermediate-depth earthquakes and the DSZ are generally controlled by the thermal structure of the slab, which is function of the convergence rate and the slab age [e.g. *Peacock*, 2001; *Abers et al.*, 2013].

The Tonga subduction zone, with fastest convergence rate among all subduction zones and a relatively old incoming-plate age, has an abundance of intermediate-depth earthquakes. The convergence rate varies from 240 mm/yr in the north to about 160 mm/yr at 22°S [*Bevis et al.*, 1995] while the slab age and dip angle roughly remain constant (Fig. 5.1), so the slab thermal structure changes systematically along strike. Thus it is an exemplary region to isolate the influence of the slab temperature structure on the intermediate-depth earthquakes from other factors.

The DSZ in Tonga was initially discovered by *Kawakatsu* [1985] with a depth range from 60 to 200 km. Although overall the slab is dominated by downdip compressional stress [*Isacks and Molnar*, 1971], a few earthquakes in the lower plane of the DSZ are characterized by downdip tensional stresses [*Kawakatsu*, 1985; 1986]. However, due to the lack of local seismic data, the Tonga DSZ has not been precisely delineated, and its implications for intermediate-depth seismicity and slab processes such as dehydration reactions remain unclear. Here we present the precise hypocenters of intermediate-depth earthquakes in the Tonga subduction zone using a combination of local and global data and derive a more detailed image of the Tonga DSZ. We then interpret the results in terms of thermal models, the *p-T* conditions, and the stress state of the slab.

5.2. Data and Methods

Most of the data used in this study was collected from 49 ocean bottom seismographs (OBSs) deployed in the Tonga-Lau-Fiji region from November 2009 to October 2010, and 17 island-based seismic stations operated from October 2009 to December 2010 (red symbols in Fig. 5.1). Each of 29 OBSs from Woods Hole Oceanographic Institution (WHOI) contains a Guralp CMG3T seismometer and a Quanterra Q330 datalogger, while other 20 OBSs from Lamont-Doherty Earth Observatory (LDEO) use Sercel L-4C seismometers and LDEO-designed dataloggers. All of these OBSs were operating well during the deployment. The land stations were deployed over islands of Tonga and Fiji. Each of them contains a broadband three-component seismometer (Guralp CMG3T, Streckeisen STS-2, or Nanometrics Trillium 240PA) and a Reftek 130-01 recorder.

5.2.1 Locating/relocating Earthquakes

We first manually examined 764 earthquakes from the Reviewed International Seismological Centre (ISC) Bulletin [*ISC*, 2013] that occurred between December 2009 and December 2010 with epicenters confined in latitudes of 16.5˚S-24˚S and longitudes of 177˚E-171˚W using the data from the local seismic array. *P* and *S* arrivals of these 764 events were manually picked, and then relocated using the Antelope software package [*Harvey*, 2003] using the generalized earthquake-location package [*Pavlis et al.*, 2004] with the ISAP91 velocity model [*Kennett and Engdahl*, 1991]. We additionally picked the arrivals of 399 previously unlocated earthquakes, which were automatically detected by Antelope, in the same region and time period but confined in a depth range of 50-450 km. This results in 94851 *P* arrivals and 14772 *S* arrivals for 1163 earthquakes in total. We also combined the arrival data of more than 2000 events from the 1994

Lau Basin Ocean Bottom Seismograph Survey (LABATTS) and the 1993-1995 Southwest Pacific Seismic Experiment (SPASE) [*Wiens et al.*, 1997; *Koper et al.*, 1998] (yellow symbols in Fig. 5.1). In order to investigate the slab stress state, we also relocated earthquakes from the Global Centroid Moment Tensor (CMT) catalog [*Dziewoński et al.*, 1981; *Ekström et al.*, 2012] in the same region over 1977-2013 using the *P*, *S*, and *pP* arrivals recorded by global stations in the ISC catalog [*ISC*, 2013]. *S* arrivals for epicentral distances larger than 10˚ were omitted due to generally large arrival time uncertainties.

Since the focus of this study is the intermediate-depth earthquakes, we used the hypocentroidal decomposition relative relocation algorithm [*Jordan and Sverdrup*, 1981; *Bergman and Solomon*, 1990] to relocate only the events that were initially located within the depth range of 50-450 km. Including earthquakes at depths of 300-450 is essential to constrain the slab geometry. The advantage of combining the local data with the ISC teleseismic data in the same relative relocation is significant, because the arrivals recorded by the local stations can help to constrain the CMT events without local records through the overlapping global stations.

After the initial inversion, the most poorly located events eliminated and the remaining dataset was again relocated. This procedure was repeated several times in order to include only earthquakes with the smallest uncertainties. We initially divided the events into 3 subsets in 3 subregions from north to south, and relocated each subset. Such strategy of reducing data amount is necessary because the hypocentroidal decomposition algorithm is designed for clustered events so that raypaths to the same station sample similar lateral heterogeneity. As some events with large uncertainties were discarded after iterations, the final round of relocation included only two subsets in the northern and southern subregions divided along 20.1˚S. No significant discrepancies among hypocenters near 20.1˚S are found because of this dividing. The final result

consists of 374 events recorded by both local and global stations during 1993-1995 and 2009-2010, of which 27 have the CMT solutions, and 297 events with CMT solutions with constrained by only global stations.

We further projected these earthquakes into 6 cross-sections perpendicular to the Tonga trench, each with a width of 133 km (Fig. 5.3), and determined the slab geometry for each cross-section based on these events. The slab surface is fit using the smoothing spline algorithm in MATLAB, such that the resulting surface lies above 85% of all hypocenters at depths 50-400 km.

5.2.2 Modeling Slab Thermal Structures

In order to investigate the *p-T* conditions of these earthquakes, we develop 2-D thermal models for each cross-section with varying slab geometry defined in the last section. The modeling generally follows that of *van Keken et al.* [2002] and *Syracuse et al.* [2010], benchmarked by *van Keken et al.* [2008], in which a dynamic corner flow in the mantle wedge is driven exclusively by the kinematic motion of the slab under a fixed overriding plate. The models are calculated using a finite element approach based on the SEPRAN modeling package (http://ta.twi.tudelft.nl/sepran/sepran.html), following the methods described in *Cuvelier et al.* [1986].

By ignoring the thermal buoyancy in the wedge, secondary convection, and compressible effects of mantle, the governing equations are simplified as the conservation of mass

$$\nabla \cdot \vec{v} = 0 \tag{5.1}$$

and the conservation of momentum

$$\nabla \cdot \overline{\overline{\tau}} - \nabla P = 0 \tag{5.2}$$

where $\vec{v}$ is the velocity, P is the dynamic pressure, $\overline{\overline{\tau}}$ is the deviatoric stress tensor given by

$$\overline{\overline{\tau}} = 2\eta\dot{\varepsilon} \tag{5.3}$$

where η is the effective dynamic viscosity, and $\dot{\varepsilon}$ is the strain rate tensor given by

$$\dot{\varepsilon}_{ij} = \frac{1}{2}\left(\frac{\partial v_i}{\partial x_j} + \frac{\partial v_j}{\partial x_i}\right) \tag{5.4}$$

The mantle viscosity is defined by a non-Newtonian, temperature- and stress-dependent rheology based on a dislocation creep flow law for dry olivine as

$$\eta(T,\dot{\varepsilon}) = A^{-1/n}\mu\exp\left(\frac{E}{nRT}\right)\dot{\varepsilon}^{(1-n)/n} \tag{5.5}$$

where R = 8.3145 J/mol/K is the gas constant, A, E, μ, and n are listed in Table 1 [*Karato and Wu*, 1993]. The temperature is calculated based on the heat advection-diffusion equation

$$\rho c_p\left[\frac{\partial T}{\partial t} + (\vec{v}\cdot\nabla)T\right] = \nabla\cdot(\kappa\nabla T) + H \tag{5.6}$$

where T is the temperature, t is the time, H is the volumetric heat production, ρ, c_p, and $\varkappa$ are listed in Table 1. The overriding plate is modeled as a young oceanic lithosphere (half space cooling profile) with an initial age of 10 Myr. The modeling thus is time-dependent, although the kinematic descriptions and boundary conditions are fixed. We take models after evolution of 20 Myr, which is (more than) sufficient to reach a quasi-steady-state thermal structure.

The mantle potential temperature is assumed to be constant as 1500 ˚C over all cross-sections according to the estimation from major element chemistry at the Central Lau Spreading Center [*Wei et al.*, 2015], though this value is about 25 ˚C higher than that for the southern cross-sections. The condition of plate coupling between the slab and the mantle wedge is crucial for modeling the shallow part of the subduction zone. We adopt the assumption of *Syracuse et al.* [2010] that the plates partially couple above the depth of 80 km and become fully coupled below

this depth, hereinafter 'D80' assumption. This assumption is valid in this study as our focus is the intermediate-depth earthquakes and the slab surface shallower than 50 km is poorly constrained due to the lack of precisely relocated seismicity.

The kinematic information of the slab for each cross-section is shown in Table 1, according to previous geodetic studies and modeling [*Zellmer and Taylor*, 2001; *Syracuse and Abers*, 2006; *Syracuse et al.*, 2010]. The convergence rates are corrected normal to the trench, and the back-arc spreading rates are also taken into account so that V_C describes motion of the incoming plate with respect to the arc. The other parameters, including the plates' age and sediment thickness, are set constant for all cross-sections as shown in Table 1. Therefore, the differences between individual 2-D thermal models come solely because of the varying slab geometry and the convergence rate V_C.

5.3. Results

5.3.1 Earthquake locations

A total of 671 intermediate-depth earthquakes with 95% relative location uncertainties smaller than 8 km in all directions were relocated (Fig. 5.2 and Table 5.3). Figs. 5.3 and 5.4 show systematic along-strike variations of the intermediate-depth earthquakes in the Tonga subduction zone. It is likely that fewer earthquakes are relocated along cross-section F-F' due to poorer local station coverage. Nevertheless, the seismogenic zone is thicker in the north than in the south. Two linear features of seismicity are observed in the map views: Stripe I at the depths of 100-150 km only in the north and Stripe II at the depths of 200-300 km through out the whole study region. Stripe I is located right beneath the volcanic arc, whereas the Stripe II appears to become shallower and closer to the arc towards south. A clear DSZ can be identified along the

cross-section C-C' and D-D', although the hypocenter distributions along A-A' and B-B' possibly have similar patterns.

At depths greater than 300 km, the epicenters curve and form a shallower dip in the north, suggesting a flattened slab in that region [*Hamburger and Isacks*, 1987]. The slab surfaces fit by the relocated hypocenters (red curves in Fig. 5.4) generally agree well with the Slab 1.0 model [*Hayes et al.*, 2012] (black dashed curves in Fig. 5.4) at depths shallower than 300 km but deviate below. The slab rebends upwards at a depth slightly greater than the depth of stripe II.

5.3.2 Thermal models

As expected, the cold core of the Tonga slab extends deeper compared to that in northeastern Japan [*van Keken et al.*, 2012] due to its high convergence rate. This is true even for the southern sections where the 400 ˚C isotherm extends to 200 km. But the northern cross-sections, with higher convergence rates, show a cold core with temperature lower than 400 ˚C extending as deep as 300 km. For comparison, the lower end of the isotherm of 400 ˚C in Tohoku is only 170-km deep [*van Keken et al.*, 2012].

The relocated hypocenters, along with their principle axes if associated with a Global CMT solution [*Dziewoński et al.*, 1981; *Ekström et al.*, 2012], are superposed onto the thermal structures in Fig. 5.5. We further sorted the events into three categories: downdip compressional events of which T axes are within 30˚ of the slab dip vector, downdip tensional of which P axes within 30˚ of the slab dip vector, and null events which do not fall into either of the previous groupings, in many cases because the principal exes are oriented along strike. The double-plane structure of downdip compressional focal mechanisms overlying downdip tensional mechanisms then can be easily identified along northern cross-sections.

According to the thermal models, the *p-T* conditions of the slab surface and earthquakes along each cross-section were extracted to plot Fig. 5.6. We also assumed a crustal thickness of 5.5 km based on a previous active source seismic refraction study of the incoming Pacific plate [*Crawford et al.*, 2003], and then determined the *p-T* conditions of the Moho. The largest source of uncertainty in the earthquake pressure and temperature are possible systematic errors introduced by fitting the slab surface with hypocenters, as intermediate-depths earthquakes are generally believed to be within the subducting plate. Studies of converted seismic waves in Alaska, Central Cascadia, and northeastern Japan suggest that the hypocenters at depths greater than 100 km may take place close to or below the slab Moho instead of the surface, whereas at shallower depths the upper zone earthquakes occur in the subducting oceanic crust [e.g. *Abers et al.*, 2013; *Shiina et al.*, 2013]. We thus estimated the uncertainties of the slab location to be about 5 km normal to the slab, and further calculated the corresponding uncertainties of temperature and pressure for the earthquakes. The estimated errors of pressure are negligible but the thermal uncertainties can be as large as 300 ˚C for earthquakes near the slab surface (Fig. 5.6). However, the *p-T* conditions of the slab surface and the Moho are more reliable since their thermal histories are mainly determined by the slab thermal parameters and crustal thickness.

5.4. Discussion

5.4.1 Double seismic zone

Fig. 5.7 plots the seismicity as a function of the depth normal to the slab surface along each cross-section, showing thick seismogenic zones along the northern cross-sections. In the northernmost region (A-A’), the overall seismicity does not show a double-planed structure, but

the focal mechanisms of large events appear to be separated so that the downdip compressional events are closer to the slab surface and the downdip tensional ones are deeper within the slab. This is in agreement with *Kawakatsu* [1985; 1986], suggesting the existence a DSZ based largely on focal mechanisms, with a much less active lower downdip-tensional plane.

Based on the distribution of the depths below the slab surface, we identify the lower plane of the DSZ along the cross-sections B-B', C-C', and D-D' as labeled in Fig. 5.7. These events in the lower plane and the downdip tensional ones are highlighted in Fig. 5.6 by blue and magenta dots, respectively. The lower plane events are observed at various pressures but confined in a relatively narrow range of temperature from about 500 to 700 ˚C, consistent with the lower planes in other subduction zones that cut across isotherms at a shallow angle [*Peacock*, 2001]. In contrast, the downdip tensional events are not restricted to a certain thermal range or fixed slab-normal depths, especially along the cross-section A-A'. *Kita et al.* [2010b] observed similar phenomena in East Hokkaido that a few downdip tensional events occurred between the two planes of the DSZ, and attributed these interplane earthquakes to the rise of the slab neutral plane due to the regional stress field.

The DSZ in Tonga extends to the depth of about 300 km, obviously deeper than those in northeastern Japan and other subduction zones which are limited to 180-km deep [*Yamasaki and Seno*, 2003]. This contrast of DSZ depths coincides with the difference of the lowest extent of the 400-˚C isotherms between Tonga and Tohoku (Fig. 5.5 in this study versus Fig. 4 in *van Keken et al.* [2012]). It is difficult to compare the absolute temperatures corresponding to the lower limit of the DSZ in other subduction zones [e.g. *Yamasaki and Seno*, 2003], since different numerical models are based on slightly different assumptions and parameters. However, the strong correlation between the depths of the lower limit of the DSZ and the convergence rates is

convincing. Since the most obvious consequence of varying convergence rate is thermal structure, we conclude that the termination of the DSZs among all subduction zones are predominantly controlled by slab temperature, further implying the importance of any thermal-controlled mechanisms for triggering seismicity.

The breakdown of hydrous minerals, such as serpentine, has been proposed to explain the intermediate-depth earthquakes and the DSZ [e.g. *Peacock*, 2001; *Hacker et al.*, 2003; *Yamasaki and Seno*, 2003; *Brudzinski et al.*, 2007]. Since absolute locations of the slab surface and Moho cannot be well mapped without seismic converted waves, it is difficult to distinguish earthquakes in the crust from those in the mantle. Therefore, we assume that most events deeper than 7 km from the fitted surface are mantle seismicity, and compare their *p-T* conditions with the dehydration reactions predicted for a composition of hydrous depleted mid-ocean-ridge-basalt mantle (DMM) [*Workman and Hart*, 2005]. Three major dehydration reactions of mantle minerals are shown as gray curves in Fig. 5.6: (1) breakdown of antigorite to enstatite and forsterite at low pressures or to enstatite and phase A at high pressures, (2) breakdown of phase A to forsterite, and (3) breakdown of chlorite to garnet [*Schmidt and Poli*, 2003; *Komabayashi et al.*, 2005]. Under the consideration of thermal uncertainties, almost all earthquakes fall on the left side of the gray curves in Fig. 5.6. This agrees well with the hypothesis of fluid-related embrittlement that intermediate-depth earthquakes are induced by dehydrations of antigorite, phase A, and chlorite. However, the mineral transitions at high pressures are poorly constrained by experiments, prohibiting us from investigating the mechanisms in detail.

5.4.2 Seismicity Stripe I

The Stripe I of seismicity appears as clusters of earthquakes at depths of 100-150 km along

the cross-sections A-A' and B-B'. Focal mechanisms include both downdip compression and tension, suggesting both of the two planes of the DSZ are included in the Stripe I. Despite a few events near the slab surface along the cross-section B-B', most of the Stripe I occurs within the slab mantle, with various temperatures but nearly constant pressures (Figs. 5.6 and 5.8). Given the lateral location of the Stripe I coinciding with the Tofua volcanic arc on the surface, these earthquakes may imply the dehydration of antigorite that releases water melting the overriding mantle wedge to form the volcanic arc [*Wilson et al.*, 2014]. It is mysterious that Stripe I seems to fade away in the south which seismicity becomes more diffusive. One possible explanation is that this seismicity becomes less prominent, and perhaps shallower, as the slab turns to be warmer in the south.

5.4.3 Seismicity Stripe II

Seismicity Stripe II at depths of 200-300 km lies between the two planes of the DSZ. In contrast to the Stripe I, this stripe of earthquakes shows a more consistent relationship to the *p-T* diagram. The average pressure of Stripe II earthquakes decreases southwards from 8.5 GPa in along the cross-section A-A' to 4.5 GPa along E-E' (Fig. 5.8), although the average temperature stays almost constant between 325 to 425 ˚C (Fig. 5.9).

Given the large thermal uncertainties, it is difficult to estimate the absolute values or even the trend of the temperature of the Stripe II along various cross-sections. However, the thermal structures of the slab Moho are more robust as they primarily depend on the crustal thickness, which is well resolved as 5.5 km based on previous studies of seismic refraction [*Crawford et al.*, 2003]. If the earthquakes of stripe II result from a reaction in the uppermost mantle, the Moho temperature will be the controlling variable. We therefore projected the temperatures of all

events to the Moho path in the *p-T* diagrams while keeping the pressures unchanged, thus estimating the temperature of the Moho adjacent to the earthquake locations. A few events with relatively high temperatures are excluded for this projection since the Stripe II apparently lies in the cold core of the slab. This strategy is based on the fact that the thermal gradient is much larger than the pressure gradient. The resulting statistics of the projected earthquake temperatures (Fig. 5.10) show more obvious peaks along all cross-sections within an even narrower thermal range of 475-525 ˚C. This strongly suggests that a mechanism corresponding to the Stripe II happens nearly isothermally under the pressures of 4.5-8.5 GPa.

Fig. 5.11a shows the original *p-T* conditions of the Stripe II earthquakes and their *p-T* conditions projected to the slab Moho along all cross-sections, both displaying nearly isothermal trends that cut across the *p-T* trajectory of antigorite dehydration [*Schmidt and Poli*, 2003; *Komabayashi et al.*, 2005]. Because phase relationships at low temperatures (< 500 ˚C) and high pressures (> 6 GPa) are poorly constrained by experiments, it is difficult to relate these trends to any specific reaction. Additionally, since numerical modeling tests suggest that free fluids may not percolate into the mantle wedge but transport in distance along the slab or even into the slab core [*Faccenda and Mancktelow*, 2010; *Faccenda et al.*, 2012; *Wilson et al.*, 2014], these nearly isothermal trends are more likely to reflect a combination of stress states and pore pressures, instead of any *in situ* dehydration reaction.

My proposed model is that the stripe II seismicity results from the dehydration of antigorite and/or phase A in the uppermost subducting mantle just below the Moho. Hydrous minerals in the subducting mantle are thought to consist largely of serpentine minerals formed by the reaction of seawater with mantle peridotite in the plate bending region just seaward of the trench [e.g. *Ranero et al.*, 2003; *Faccenda et al.*, 2009]. These minerals will form a layer of thickness 5-

15 km thick as suggested by seismic profiles [*Contreras-Reyes et al.*, 2007; *van Avendonk et al.*, 2011], presumably governed by the maximum depth of extensional faulting [e.g. *Lefeldt et al.*, 2009; *Emry and Wiens*, 2015]. The slab mantle starts dehydrating when the uppermost mantle reaches the temperature of about 550 ˚C, releasing abundance of free water. Driven by the negative pressure gradients, the water percolates upward and also towards the cold core of the slab to trigger the extensive seismicity (Fig. 5.11b).

5.4.4 Activity of the DSZ

DSZs have been so far observed in several subduction zones, including the Aleutians [*Engdahl and Scholz*, 1977], northeast Japan [e.g. *Hasegawa et al.*, 1978; *Kita et al.*, 2010a], the Kuriles [*Kao and Liu*, 1995], New Britain [*McGuire and Wiens*, 1995], Tonga [*Kawakatsu*, 1985; 1986]. The cause of the DSZ however still remains controversial, as its appearance shows no obvious correlation with the slab age, the age of subduction zone, the convergence rate, or the slab geometry. Even though [*Brudzinski et al.*, 2007] propose a global prevalence of the DSZs, their level of earthquake activity, particularly in the lower plane, varies dramatically. In contrast to northeastern Japan where the two planes of the DSZ are both highly active [e.g. *Kita et al.*, 2010b], the lower plane in Tonga appears to be significantly less active than the upper plane.

Since intermediate-depth earthquakes occur through out the whole region, the corresponding petrological changes discussed above should happen universally. However, Fig. 5.7 unambiguously shows that the seismogenic zone becomes thinner towards south while the lower plane of the DSZ becomes inactive. This transition coincides with the change in the slab curvature from north to south. In the north, the Tonga slab rebends upwards at depths greater than 300 km and then lies horizontally in the mantle transition zone, possibly resulting from the

rapid opening of the Lau back-arc basin since 4 Ma [*Hamburger and Isacks*, 1987]. But in the south, the slab unbends at depths of 150-200 km, and then keeps straight down to at least 600-km deep [*Zhao et al.*, 1997].

Slab unbending has been long proposed as a mechanism to provide the stress that drives water from the upper part of the slab towards the center [*Faccenda and Mancktelow*, 2010; *Faccenda et al.*, 2012] and facilitates intermediate depth earthquakes [*Wang*, 2002]. Similarly, the slab rebending at greater depths in the north introduces the same stress field to the slab, of which downdip compression near the top and downdip tension at the bottom. In the light of the fact that the background stress field in this region is downdip compressional [*Isacks and Molnar*, 1971], we propose that the stress field rather than petrological reactions is the dominant mechanism controlling the seismic activity of the lower plane. In the north where the Tonga slab undergoes unbending and rebending, the compressional stress in the upper part of the slab is strengthened by the overall stress field, whereas the tensional stress in the lower part of the slab is weakened, resulting in a DSZ with an active upper plane and a weak lower plane. In the south, the overall stress field is much more compressive since the slab extends continuously to the bottom of the mantle transition zone (MTZ) [*Zhao et al.*, 1997], in contrast to the northern region where the slab lays flat on the top of the MTZ [*van der Hilst*, 1995]. Without the contribution of the rebending, the tensional stress in the deeper part of the slab is overprinted by the overwhelming compression, leading to the cease of the lower plane, or even few downdip tensional events. This can also explain the downdip tensional events lying between the two planes of the DSZ along the cross-section A-A', as the slab rebending is most intense in the north that raises the neutral plane closer to the slab surface. Similar phenomena have been observed in East Hokkaido at shallower depths [*Kita et al.*, 2010b].

An alternative explanation for the weak activities of the lower plane is the influence of the Louisville Ridge. The subduction of this ridge, a chain of seamounts, is characterized as aseismic near the trench. Because of a few large earthquakes occurring near the location where the Louisville Ridge subducts in 1970s and 1980s, *Christensen and Lay* [1988] suggested the ridge keeps the same direction after subduction (blue region in Fig. 5.13). The aseismic ridge may mute the lower plane of the DSZ at intermediate depths, although the mechanism remains unclear [e.g. *Wang and Bilek*, 2011]. However, *Giardini and Woodhouse* [1986] proposed that the subducted Louisville Ridge was responsible to the seismic gap at depths greater than 400 km between the latitudes of 22.2˚S and 23.2˚S, implying a southwards shear deformation. If the Louisville Ridge was indeed shear-deformed southwards (green region in Fig. 5.13), it should have no influence to our study region.

In sum, our result suggest the stress states of unbending and rebending, which result from the overall dynamics of the Tonga slab and its interaction with the MTZ, play an important role in controlling the activity of the Tonga DSZ, though the possible effects from the subducted Louisville Ridge cannot be verified.

5.5. Conclusions

We used data from OBSs and island-based stations deployed in the Tonga-Fiji area from 1993 to 1995 and 2009 to 2010 to investigate the intermediate-depth seismicity of the Tonga subducting slab. The events were relocated with both local and teleseismic *P*, *pP*, and *S* arrivals using a hypocentroidal decomposition relative location algorithm [*Jordan and Sverdrup*, 1981; *Bergman and Solomon*, 1990]. The results show a double seismic zone with a separation of about

30 km along the northern part of the Tonga slab within a depth range of about 70-300 km. The upper plane is more seismically active and characterized by downdip compressional events whereas the lower plane is characterized by downdip tensional stresses, consistent with the slab unbending model.

The lower limit of the DSZ beneath Tonga is significantly deeper than that in Japan and Mariana (about 200 km [e.g. *Yamasaki and Seno*, 2003; *Kita et al.*, 2006; *Kita et al.*, 2010a; *Shiobara et al.*, 2010]), implying the importance of thermal variations in controlling the DSZ. Since the Tonga slab is the coldest slab due to its fastest subduction rate and old lithospheric age, thermally controlled processes such as serpentine dehydration can occur at greater depths, resulting in greater depths of fluid-related embrittlement and thus the intermediate-depth seismicity. Two stripes of earthquakes are identified: the shallower stripe is confined in the north exactly beneath the Tofua volcanic arc, resulting from the serpentine dehydration that supplies water to the arc. The deeper stripe of seismicity may imply dehydration reactions of antigorite and phase A in the uppermost slab mantle under pressures of 4.5-8.5 GPa. Driven by slab unbending, the water released from dehydration percolates into the cold core of the slab to trigger extensive earthquakes.

The lower plane of the DSZ appears to be absent in the southern Tonga slab, leaving a thinner seismogenic zone. This transition coincides with the change in the slab geometry, suggesting that the slab rebending provides additional stress to unbending in order to counteract the background compressional stress field, causing the downdip tensional earthquakes in the lower plane. In contrast, the southern part of the slab lacks such rebending since the slab penetrates to the bottom of the MTZ. Therefore the background compressional stress field overwhelms the effects of slab unbending to cease the lower plane.

References

Abers, G. A., J. Nakajima, P. E. van Keken, S. Kita, and B. R. Hacker (2013), Thermal–petrological controls on the location of earthquakes within subducting plates, *Earth Planet. Sci. Lett.*, *369–370*, 178-187, doi: 10.1016/j.epsl.2013.03.022.

Bergman, E. A., and S. C. Solomon (1990), Earthquake swarms on the Mid-Atlantic Ridge: Products of magmatism or extensional tectonics?, *J. Geophys. Res.*, *95*(B4), 4943-4965, doi: 10.1029/JB095iB04p04943.

Bevis, M., F. W. Taylor, B. E. Schutz, J. Recy, B. L. Isacks, S. Helu, R. Singh, E. Kendrick, J. Stowell, B. Taylor, and S. Calmantli (1995), Geodetic observations of very rapid convergence and back-arc extension at the Tonga arc, *Nature*, *374*(6519), 249-251.

Billen, M., E. Cowgill, and E. Buer (2007), Determination of fault friction from reactivation of abyssal-hill faults in subduction zones, *Geology*, *35*(9), 819-822, doi: 10.1130/g23847a.1.

Brudzinski, M. R., C. H. Thurber, B. R. Hacker, and E. R. Engdahl (2007), Global Prevalence of Double Benioff Zones, *Science*, *316*(5830), 1472-1474, doi: 10.1126/science.1139204.

Christensen, D. H., and T. Lay (1988), LARGE EARTHQUAKES IN THE TONGA REGION ASSOCIATED WITH SUBDUCTION OF THE LOUISVILLE RIDGE, *J. Geophys. Res.*, *93*(B11), 13367-13389, doi: 10.1029/JB093iB11p13367.

Contreras-Reyes, E., I. Grevemeyer, E. R. Flueh, M. Scherwath, and M. Heesemann (2007), Alteration of the subducting oceanic lithosphere at the southern central Chile trench–outer rise, *Geochem. Geophys. Geosyst.*, *8*(7), Q07003, doi: 10.1029/2007GC001632.

Crawford, W. C., J. A. Hildebrand, L. M. Dorman, S. C. Webb, and D. A. Wiens (2003), Tonga Ridge and Lau Basin crustal structure from seismic refraction data, *J. Geophys. Res.*, *108*(B4), 2195, doi: 10.1029/2001jb001435.

Cuvelier, C., A. Segal, and A. A. Van Steenhoven (1986), *Finite element methods and Navier-Stokes equations*, D. Reidel Publishing Company, Norwell, MA.

Dziewoński, A. M., T. A. Chou, and J. H. Woodhouse (1981), Determination of earthquake source parameters from waveform data for studies of global and regional seismicity, *J. Geophys. Res.*, *86*(B4), 2825-2852, doi: 10.1029/JB086iB04p02825.

Ekström, G., M. Nettles, and A. M. Dziewoński (2012), The global CMT project 2004–2010: Centroid-moment tensors for 13,017 earthquakes, *Phys. Earth Planet. In.*, *200–201*, 1-9, doi: 10.1016/j.pepi.2012.04.002.

Emry, E. L., and D. A. Wiens (2015), Incoming plate faulting in the Northern and Western Pacific and implications for subduction zone water budgets, *Earth Planet. Sci. Lett.*, *414*, 176-186, doi: 10.1016/j.epsl.2014.12.042.

Engdahl, E. R., and C. H. Scholz (1977), A double Benioff Zone beneath the central Aleutians: An unbending of the lithosphere, *Geophys. Res. Lett.*, *4*(10), 473-476, doi: 10.1029/GL004i010p00473.

Faccenda, M., T. V. Gerya, and L. Burlini (2009), Deep slab hydration induced by bending-related variations in tectonic pressure, *Nature Geosci.*, *2*(11), 790-793, doi: 10.1038/ngeo656.

Faccenda, M., and N. S. Mancktelow (2010), Fluid flow during unbending: Implications for slab hydration, intermediate-depth earthquakes and deep fluid subduction, *Tectonophysics*, *494*(1–2), 149-154, doi: 10.1016/j.tecto.2010.08.002.

Faccenda, M., T. V. Gerya, N. S. Mancktelow, and L. Moresi (2012), Fluid flow during slab unbending and dehydration: Implications for intermediate-depth seismicity, slab weakening and deep water recycling, *Geochem. Geophys. Geosyst.*, *13*(1), Q01010, doi: 10.1029/2011GC003860.

Giardini, D., and J. H. Woodhouse (1986), Horizontal shear flow in the mantle beneath the Tonga arc, *Nature*, *319*(6054), 551-555.

Hacker, B. R., S. M. Peacock, G. A. Abers, and S. D. Holloway (2003), Subduction factory 2. Are intermediate-depth earthquakes in subducting slabs linked to metamorphic dehydration reactions?, *J. Geophys. Res.*, *108*(B1), 2030, doi: 10.1029/2001JB001129.

Hacker, B. R. (2008), H_2O subduction beyond arcs, *Geochem. Geophys. Geosyst.*, *9*(3), Q03001, doi: 10.1029/2007GC001707.

Hamburger, M. W., and B. L. Isacks (1987), Deep earthquakes in the southwest Pacific: A tectonic interpretation, *J. Geophys. Res.*, *92*(B13), 13841-13854, doi: 10.1029/JB092iB13p13841.

Harvey, D. (2003), Antelope: A Software Infrastructure for the Support of Virtual Observatories, abstract presented at AGU 2003 Fall Meeting, American Geophysical Union, San Francisco, CA.

Hasegawa, A., N. Umino, and A. Takagi (1978), Double-planed structure of the deep seismic zone in the northeastern Japan arc, *Tectonophysics*, *47*(1–2), 43-58, doi: 10.1016/0040-1951(78)90150-6.

Hayes, G. P., D. J. Wald, and R. L. Johnson (2012), Slab1.0: A three-dimensional model of global subduction zone geometries, *J. Geophys. Res.*, *117*(B1), B01302, doi: 10.1029/2011jb008524.

Hobbs, B. E., and A. Ord (1988), Plastic instabilities: Implications for the origin of intermediate and deep focus earthquakes, *J. Geophys. Res.*, *93*(B9), 10521-10540, doi: 10.1029/JB093iB09p10521.

Isacks, B., and P. Molnar (1971), Distribution of stresses in the descending lithosphere from a global survey of focal-mechanism solutions of mantle earthquakes, *Rev. Geophys.*, *9*(1), 103-174, doi: 10.1029/RG009i001p00103.

International Seismological Centre (2013), Reviewed ISC Bulletin, http://www.isc.ac.uk, Internatl. Seis. Cent., Thatcham, United Kingdom.

Jordan, T. H., and K. A. Sverdrup (1981), Teleseismic location techniques and their application to earthquake clusters in the South-Central Pacific, *Bull. Seism. Soc. Amer.*, *71*(4), 1105-1130.

Jung, H., H. W. Green Ii, and L. F. Dobrzhinetskaya (2004), Intermediate-depth earthquake faulting by dehydration embrittlement with negative volume change, *Nature*, *428*(6982), 545-549.

Kao, H., and L.-G. Liu (1995), A hypothesis for the seismogenesis of a double seismic zone, *Geophys. J. Int.*, *123*(1), 71-84, doi: 10.1111/j.1365-246X.1995.tb06662.x.

Karato, S.-i., and P. Wu (1993), Rheology of the Upper Mantle: A Synthesis, *Science*, *260*(5109), 771-778, doi: 10.1126/science.260.5109.771.

Kawakatsu, H. (1985), Double seismic zone in Tonga, *Nature*, *316*(6023), 53-55.

Kawakatsu, H. (1986), Downdip tensional earthquakes beneath the Tonga Arc: A double seismic zone?, *J. Geophys. Res.*, *91*(B6), 6432-6440, doi: 10.1029/JB091iB06p06432.
Kelemen, P. B., and G. Hirth (2007), A periodic shear-heating mechanism for intermediate-depth earthquakes in the mantle, *Nature*, *446*(7137), 787-790, doi: 10.1038/nature05717.
Kennett, B. L. N., and E. R. Engdahl (1991), Traveltimes for global earthquake location and phase identification, *Geophys. J. Int.*, *105*(2), 429-465, doi: 10.1111/j.1365-246X.1991.tb06724.x.
Kirby, S. (1995), Interslab earthquakes and phase changes in subducting lithosphere, *Rev. Geophys.*, *33*(S1), 287-297, doi: 10.1029/95RG00353.
Kirby, S., R. E. Engdahl, and R. Denlinger (1996), Intermediate-Depth Intraslab Earthquakes and Arc Volcanism as Physical Expressions of Crustal and Uppermost Mantle Metamorphism in Subducting Slabs, in *Subduction Top to Bottom*, edited, pp. 195-214, American Geophysical Union.
Kita, S., T. Okada, J. Nakajima, T. Matsuzawa, and A. Hasegawa (2006), Existence of a seismic belt in the upper plane of the double seismic zone extending in the along-arc direction at depths of 70–100 km beneath NE Japan, *Geophys. Res. Lett.*, *33*(24), L24310, doi: 10.1029/2006GL028239.
Kita, S., T. Okada, A. Hasegawa, J. Nakajima, and T. Matsuzawa (2010a), Existence of interplane earthquakes and neutral stress boundary between the upper and lower planes of the double seismic zone beneath Tohoku and Hokkaido, northeastern Japan, *Tectonophysics*, *496*(1–4), 68-82, doi: 10.1016/j.tecto.2010.10.010.
Kita, S., T. Okada, A. Hasegawa, J. Nakajima, and T. Matsuzawa (2010b), Anomalous deepening of a seismic belt in the upper-plane of the double seismic zone in the Pacific slab beneath the Hokkaido corner: Possible evidence for thermal shielding caused by subducted forearc crust materials, *Earth Planet. Sci. Lett.*, *290*(3–4), 415-426, doi: 10.1016/j.epsl.2009.12.038.
Komabayashi, T., K. Hirose, K.-i. Funakoshi, and N. Takafuji (2005), Stability of phase A in antigorite (serpentine) composition determined by in situ X-ray pressure observations, *Phys. Earth Planet. In.*, *151*(3–4), 276-289, doi: 10.1016/j.pepi.2005.04.002.
Koper, K. D., D. A. Wiens, L. M. Dorman, J. A. Hildebrand, and S. C. Webb (1998), Modeling the Tonga slab: Can travel time data resolve a metastable olivine wedge?, *J. Geophys. Res.*, *103*(B12), 30079-30100, doi: 10.1029/98JB01517.
Lee, R. W., and S. H. Kirby (1984), Experimental deformation of topaz crystals: Possible embrittlement by intracrystalline water, *J. Geophys. Res.*, *89*(B6), 4161-4166, doi: 10.1029/JB089iB06p04161.
Lefeldt, M., I. Grevemeyer, J. Goßler, and J. Bialas (2009), Intraplate seismicity and related mantle hydration at the Nicaraguan trench outer rise, *Geophys. J. Int.*, *178*(2), 742-752, doi: 10.1111/j.1365-246X.2009.04167.x.
McGuire, J. J., and D. A. Wiens (1995), A double seismic zone in New Britain and the morphology of the Solomon Plate at intermediate depths, *Geophys. Res. Lett.*, *22*(15), 1965-1968, doi: 10.1029/95GL01806.
Pavlis, G. L., F. Vernon, D. Harvey, and D. Quinlan (2004), The generalized earthquake-location (GENLOC) package: an earthquake-location library, *Computers & Geosciences*, *30*(9–10), 1079-1091, doi: 10.1016/j.cageo.2004.06.010.

Peacock, S. M. (2001), Are the lower planes of double seismic zones caused by serpentine dehydration in subducting oceanic mantle?, *Geology*, *29*(4), 299-302, doi: 10.1130/0091-7613(2001)029<0299:atlpod>2.0.co;2.
Proctor, B., and G. Hirth (2015), Role of pore fluid pressure on transient strength changes and fabric development during serpentine dehydration at mantle conditions: Implications for subduction-zone seismicity, *Earth Planet. Sci. Lett.*, *421*, 1-12, doi: 10.1016/j.epsl.2015.03.040.
Ranero, C. R., J. Phipps Morgan, K. McIntosh, and C. Reichert (2003), Bending-related faulting and mantle serpentinization at the Middle America trench, *Nature*, *425*(6956), 367-373.
Schmidt, M. W., and S. Poli (2003), Generation of Mobile Components during Subduction of Oceanic Crust, in *Treatise on Geochemistry*, edited by H. D. H. K. Turekian, pp. 567-591, Pergamon, Oxford.
Shiina, T., J. Nakajima, and T. Matsuzawa (2013), Seismic evidence for high pore pressures in the oceanic crust: Implications for fluid-related embrittlement, *Geophys. Res. Lett.*, *40*(10), 2006-2010, doi: 10.1002/grl.50468.
Shiobara, H., H. Sugioka, K. Mochizuki, S. Oki, T. Kanazawa, Y. Fukao, and K. Suyehiro (2010), Double seismic zone in the North Mariana region revealed by long-term ocean bottom array observation, *Geophys. J. Int.*, *183*(3), 1455-1469, doi: 10.1111/j.1365-246X.2010.04799.x.
Syracuse, E. M., and G. A. Abers (2006), Global compilation of variations in slab depth beneath arc volcanoes and implications, *Geochem. Geophys. Geosyst.*, *7*(5), Q05017, doi: 10.1029/2005GC001045.
Syracuse, E. M., P. E. van Keken, and G. A. Abers (2010), The global range of subduction zone thermal models, *Phys. Earth Planet. In.*, *183*(1–2), 73-90, doi: 10.1016/j.pepi.2010.02.004.
Umino, N., and A. Hasegawa (1975), On the two-layered structure of deep seismic plane in northeastern Japan arc, *J. Seismol. Soc. Japan*, (in Japanese), *27*, 125-139.
van Avendonk, H. J. A., W. S. Holbrook, D. Lizarralde, and P. Denyer (2011), Structure and serpentinization of the subducting Cocos plate offshore Nicaragua and Costa Rica, *Geochem. Geophys. Geosyst.*, *12*(6), Q06009, doi: 10.1029/2011GC003592.
van der Hilst, R. (1995), Complex morphology of subducted lithosphere in the mantle beneath the Tonga trench, *Nature*, *374*(6518), 154-157.
van Keken, P. E., B. Kiefer, and S. M. Peacock (2002), High-resolution models of subduction zones: Implications for mineral dehydration reactions and the transport of water into the deep mantle, *Geochem. Geophys. Geosyst.*, *3*(10), 1056, doi: 10.1029/2001GC000256.
van Keken, P. E., C. Currie, S. D. King, M. D. Behn, A. Cagnioncle, J. He, R. F. Katz, S.-C. Lin, E. M. Parmentier, M. Spiegelman, and K. Wang (2008), A community benchmark for subduction zone modeling, *Phys. Earth Planet. In.*, *171*(1–4), 187-197, doi: 10.1016/j.pepi.2008.04.015.
van Keken, P. E., B. R. Hacker, E. M. Syracuse, and G. A. Abers (2011), Subduction factory: 4. Depth-dependent flux of H_2O from subducting slabs worldwide, *J. Geophys. Res.*, *116*(B1), B01401, doi: 10.1029/2010JB007922.
van Keken, P. E., S. Kita, and J. Nakajima (2012), Thermal structure and intermediate-depth seismicity in the Tohoku-Hokkaido subduction zones, *Solid Earth*, *3*(2), 355-364, doi: 10.5194/se-3-355-2012.
Wang, K. (2002), Unbending combined with dehydration embrittlement as a cause for double and triple seismic zones, *Geophys. Res. Lett.*, *29*(18), 1889, doi: 10.1029/2002GL015441.

Wang, K., and S. L. Bilek (2011), Do subducting seamounts generate or stop large earthquakes?, *Geology*, *39*(9), 819-822, doi: 10.1130/g31856.1.
Warren, L. M., A. N. Hughes, and P. G. Silver (2007), Earthquake mechanics and deformation in the Tonga-Kermadec subduction zone from fault plane orientations of intermediate- and deep-focus earthquakes, *J. Geophys. Res.*, *112*(B5), B05314, doi: 10.1029/2006JB004677.
Wei, S. S., D. A. Wiens, Y. Zha, T. Plank, S. C. Webb, D. K. Blackman, R. A. Dunn, and J. A. Conder (2015), Seismic evidence of effects of water on melt transport in the Lau back-arc mantle, *Nature*, *518*(7539), 395-398, doi: 10.1038/nature14113.
Wiens, D. A., H. J. Gilbert, B. Hicks, M. E. Wysession, and P. J. Shore (1997), Aftershock sequences of moderate-sized intermediate and deep earthquakes in the Tonga Subduction Zone, *Geophys. Res. Lett.*, *24*(16), 2059-2062, doi: 10.1029/97GL01957.
Wilson, C. R., M. Spiegelman, P. E. van Keken, and B. R. Hacker (2014), Fluid flow in subduction zones: The role of solid rheology and compaction pressure, *Earth Planet. Sci. Lett.*, *401*, 261-274, doi: 10.1016/j.epsl.2014.05.052.
Workman, R. K., and S. R. Hart (2005), Major and trace element composition of the depleted MORB mantle (DMM), *Earth Planet. Sci. Lett.*, *231*(1–2), 53-72, doi: 10.1016/j.epsl.2004.12.005.
Yamasaki, T., and T. Seno (2003), Double seismic zone and dehydration embrittlement of the subducting slab, *J. Geophys. Res.*, *108*(B4), 2212, doi: 10.1029/2002JB001918.
Zellmer, K. E., and B. Taylor (2001), A three-plate kinematic model for Lau Basin opening, *Geochem. Geophys. Geosyst.*, *2*(5), doi: 10.1029/2000gc000106.
Zhao, D., Y. Xu, D. A. Wiens, L. Dorman, J. Hildebrand, and S. Webb (1997), Depth Extent of the Lau Back-Arc Spreading Center and Its Relation to Subduction Processes, *Science*, *278*(5336), 254-257, doi: 10.1126/science.278.5336.254.

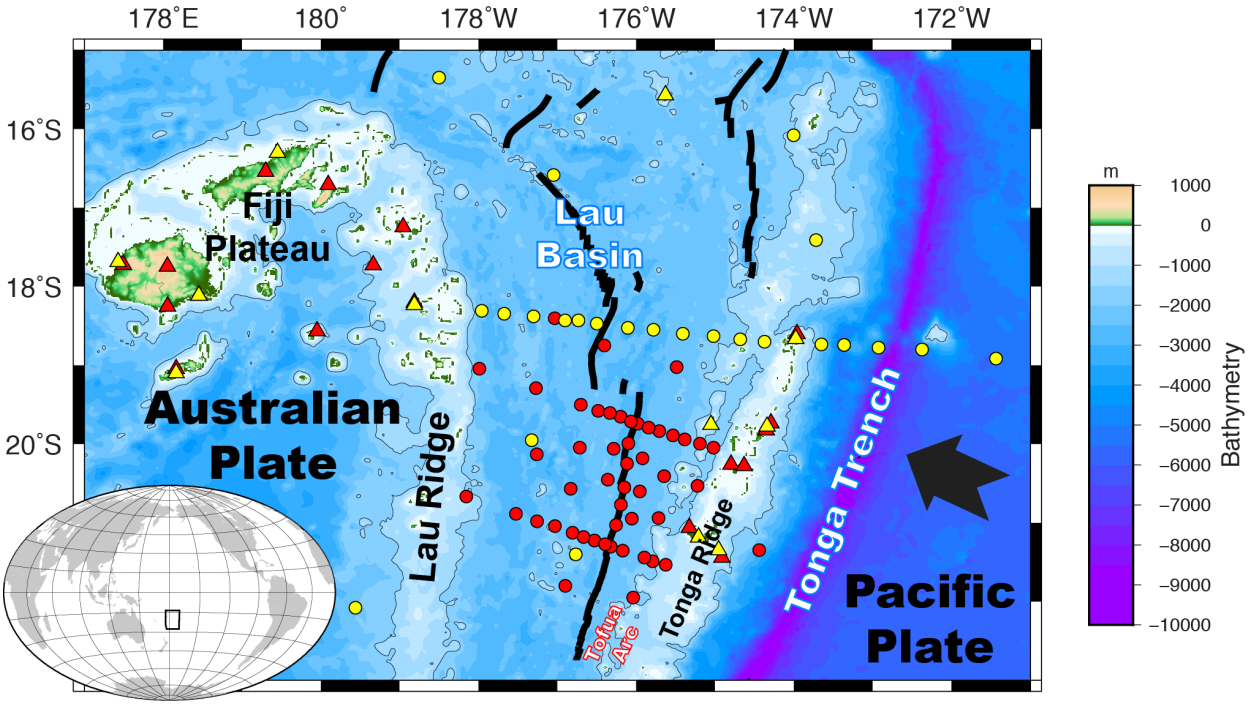

Figure 5.1. Tectonic map and seismic station locations.

The Pacific plate subducts beneath the Tonga trench from the southeast (bold arrow). Spreading centers are denoted by black lines, and the 1500 m bathymetric contour is shown. Red triangles represent island-based stations operated from Oct. 2009 to Dec. 2010, and red dots are OBSs deployed from Nov. 2009 to Nov. 2010. Yellow dots and triangles indicate OBSs of the 1994 LABATTS project and island-based stations of the 1993-1995 SPASE project, respectively. Inset displays the study region in a global map.

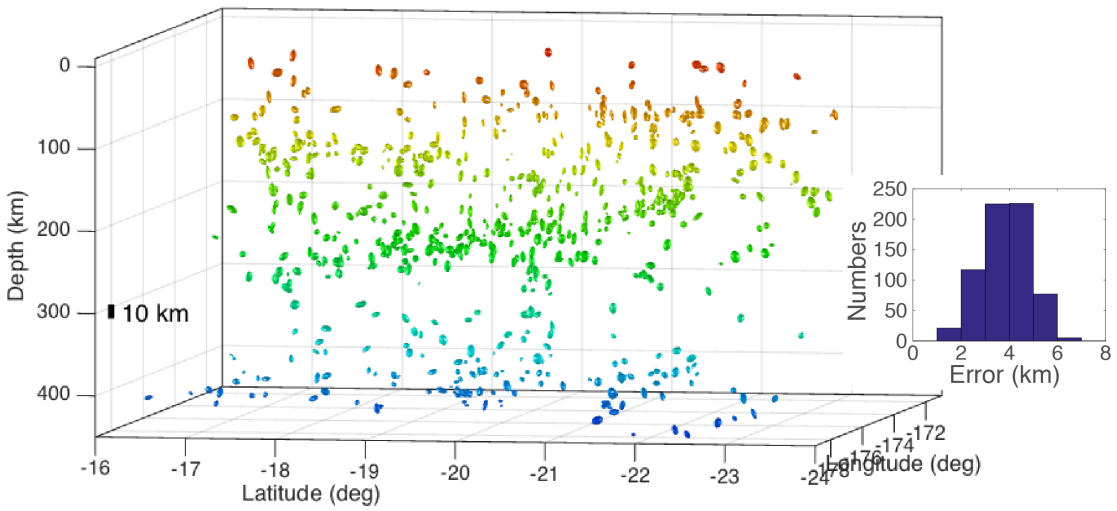

Figure 5.2. Three-dimensional view of 95% uncertainty ellipsoids for all events.

Ellipse colors indicate depths. The black bar illustrates the scale of 10 km. Inset shows the statistical distribution of the 3D-averaged location errors.

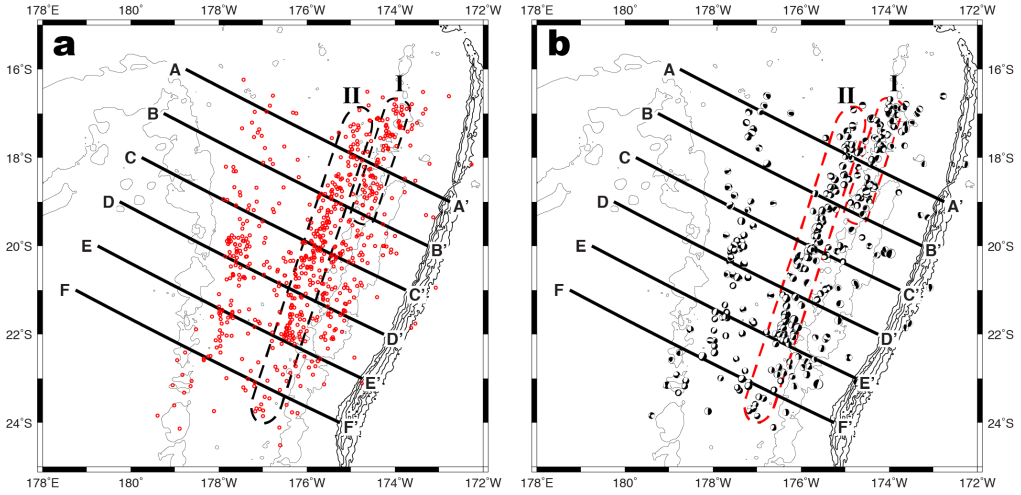

Figure 5.3. Map view of the relocated earthquakes.

(a) Map view of all relocated intermediate-depth earthquakes. b) Map view of relocated Global CMT events, with moment tensor solutions shown as lower hemisphere projections. 1 km bathymetric contours are shown to outline the Tonga Ridge, Tofua arc, Lau Ridge, and Fiji Plateau, and 7, 8, 9, and 10 km contours are also shown to delineate the Tonga trench.

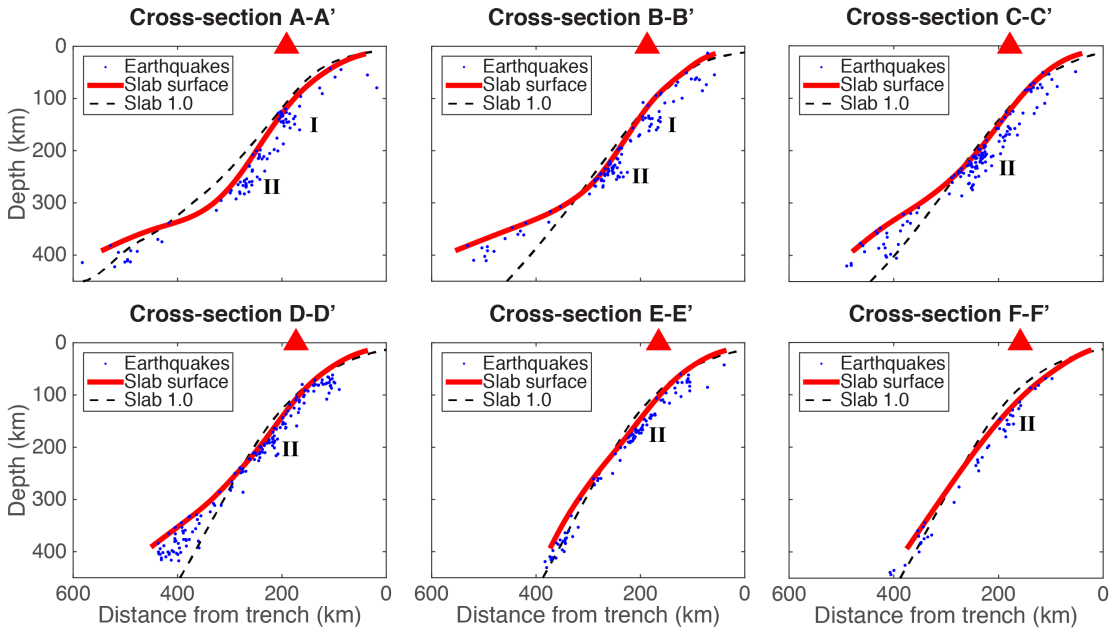

Figure 5.4. Cross-sections of seismicity and slab surface fits.

Earthquakes are shown as blue dots, and the slab surface fit by the seismicity in this study (red curves) and the Slab 1.0 model [*Hayes et al.*, 2012] (black dashed curves) are plotted for comparison. The red triangle on the top represents the Tofua volcanic arc.

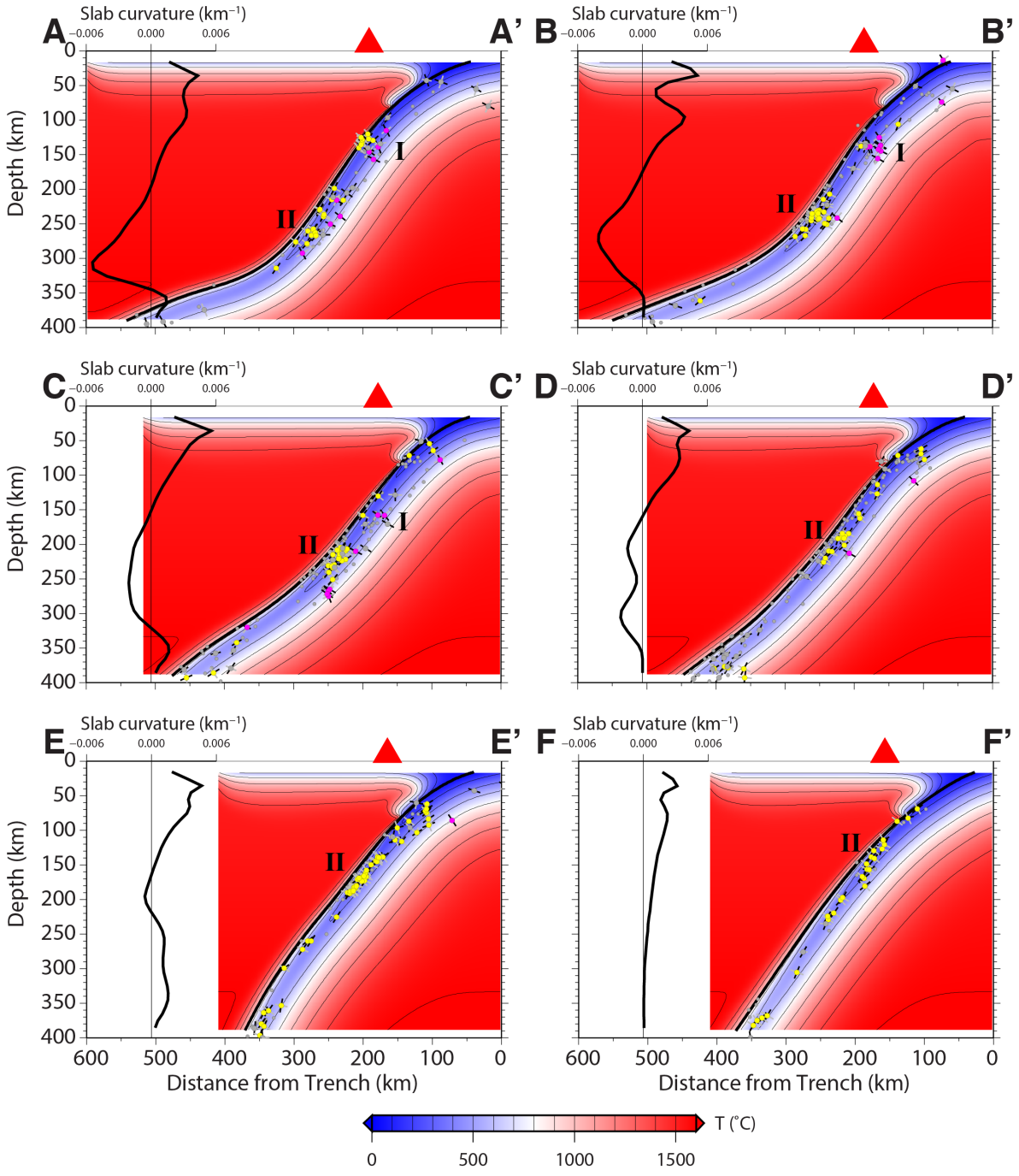

Figure 5.5. Cross-sections of the modeled thermal structure, observed seismicity, and principal axes of events from CMT solutions.

The temperature contour interval is 200 ˚C, and the bold black curve represents the slab surface.

Circles with black and gray bars show the P (gray) and T (black) axes of focal mechanisms projected to the cross-sections. These events are sorted into the categories of downdip compression (yellow circles), downdip tension (magenta circles), and null (gray circles) based on the directions of the principal axes. The length of each bar reflects the angles between the axis and the section plane. Small gray dots illustrate the events without CMT solutions. Superposed on the left is the slab curvature, defined as the second derivative of the slab surface with distance along the profile, for each cross-section.

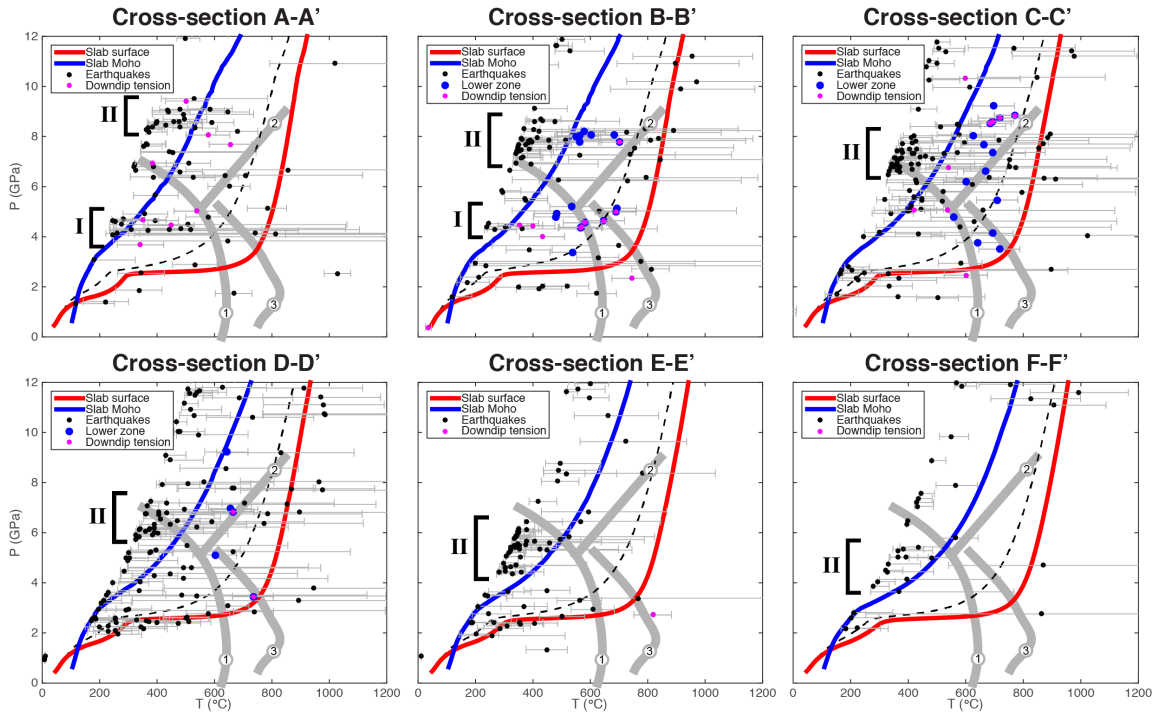

Figure 5.6. Modeled pressures and temperatures (*p-T*) of earthquakes for each cross-section.

Black dots indicate the earthquake *p-T* conditions with temperature uncertainties (gray error bars). Most of the temperature uncertainties result from uncertainty in the positioning of the slab relative to the earthquakes. The downdip tensional events are color-coded with magenta, whereas the events in the lower plane of the DSZ identified in Fig. 5.7 are color-coded with blue. There is some overlap between these two categories. The *p-T* paths of the slab surface and the Moho are illustrated by the red and blue curves, respectively. The black dashed curve represents a *p-T* threshold, of which events falling left are considered as within the slab cold core and are projected to the Moho *p-T* path in Figs. 5.10 and 5.11. Bold gray curves show predicted breakdowns of antigorite (1), phase A and enstatite (2), and chlorite (3) [*Schmidt and Poli*, 2003; *Komabayashi et al.*, 2005].

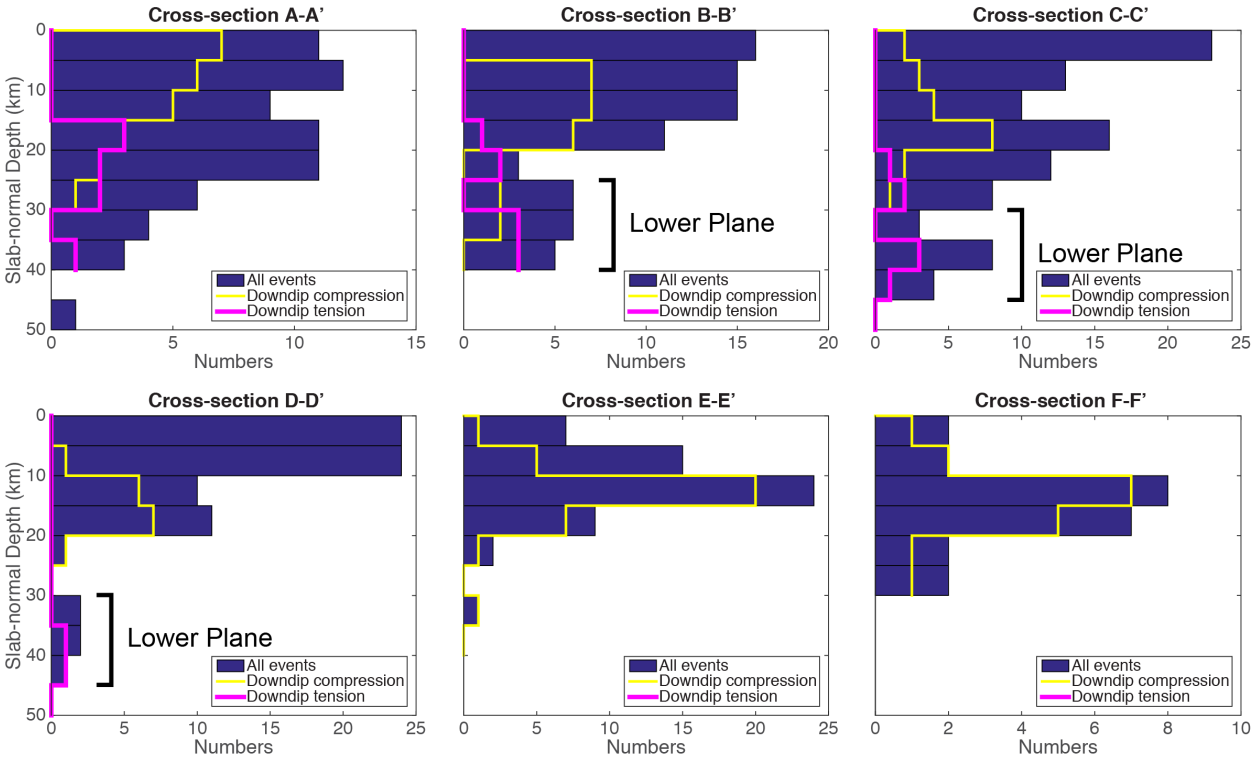

Figure 5.7. Distribution of depths beneath the slab surface for earthquake at vertical depths of 100-300 km along each cross-section.

Downdip compressional and tensional events are color-coded as labeled. The lower plane of the DSZ is identified along cross-sections B-B', C-C', and D-D'.

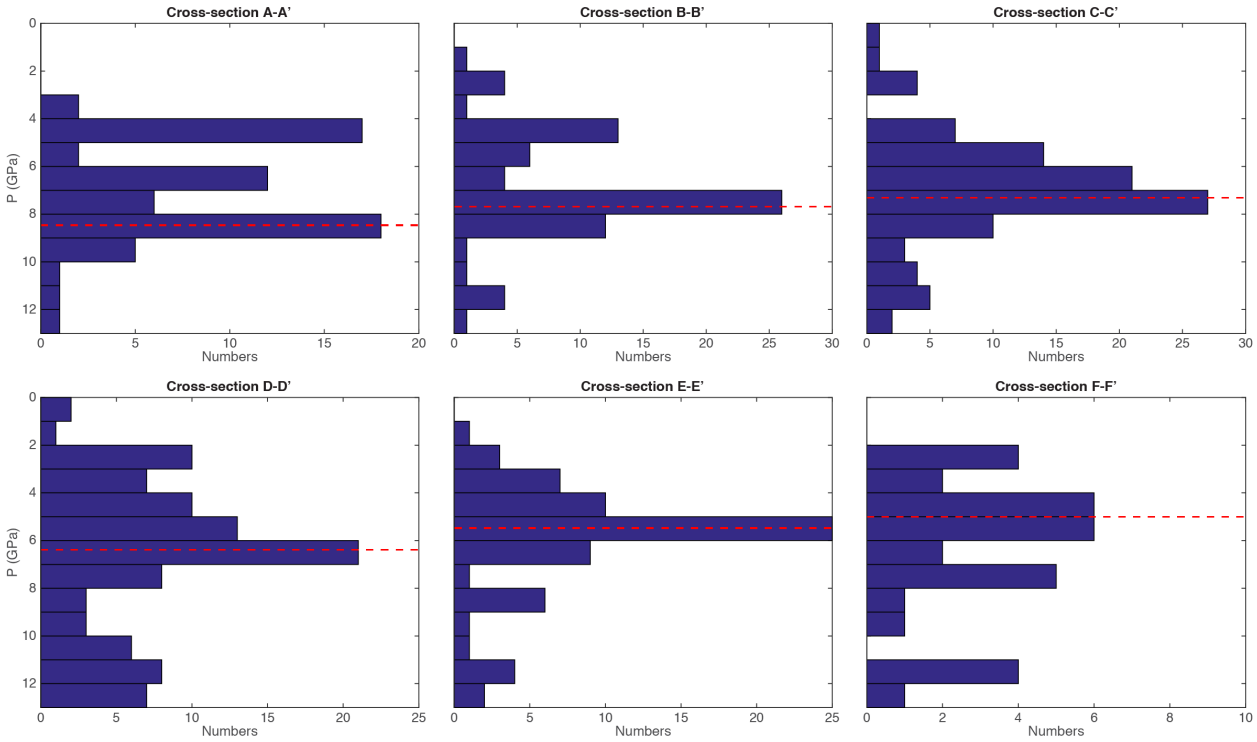

Figure 5.8. Distribution of pressure conditions of earthquakes along each cross-section.

Red lines represent the Stripe II, showing its average pressure and depth decrease from north to south.

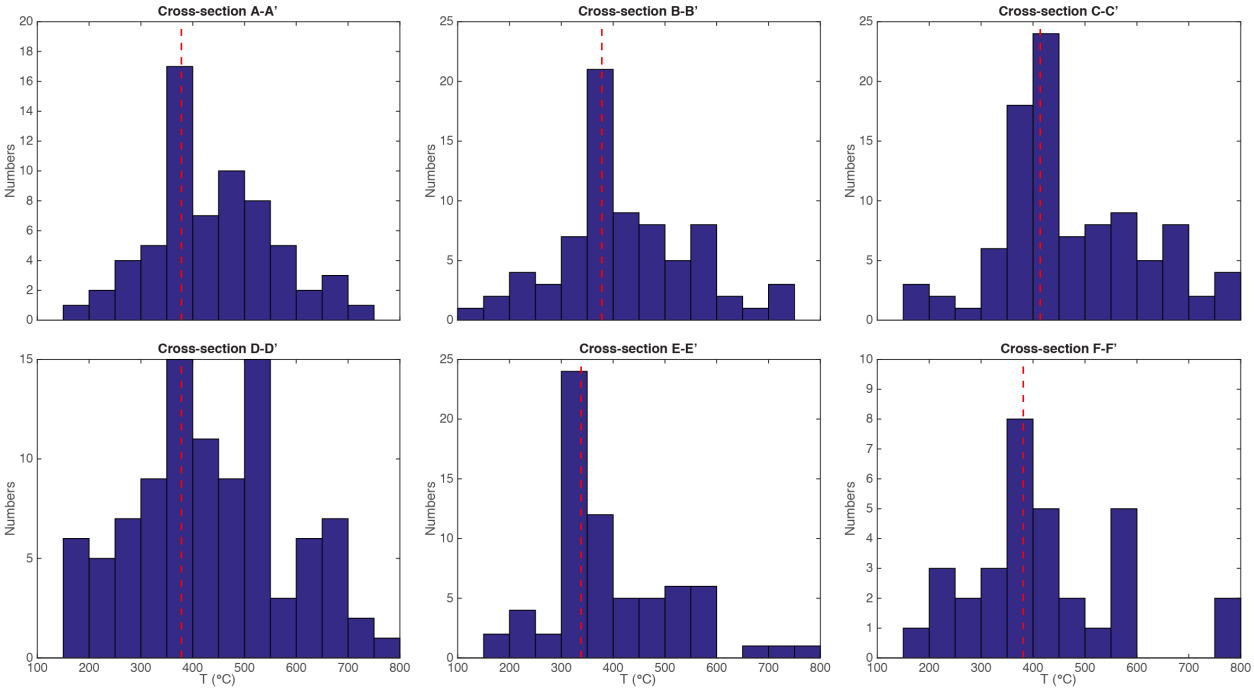

Figure 5.9. Distribution of thermal conditions of earthquakes along each cross-section.

Red dotted lines represent the temperature of the center of Stripe II, showing its average temperature confined in a narrow range of 325-425 ˚C.

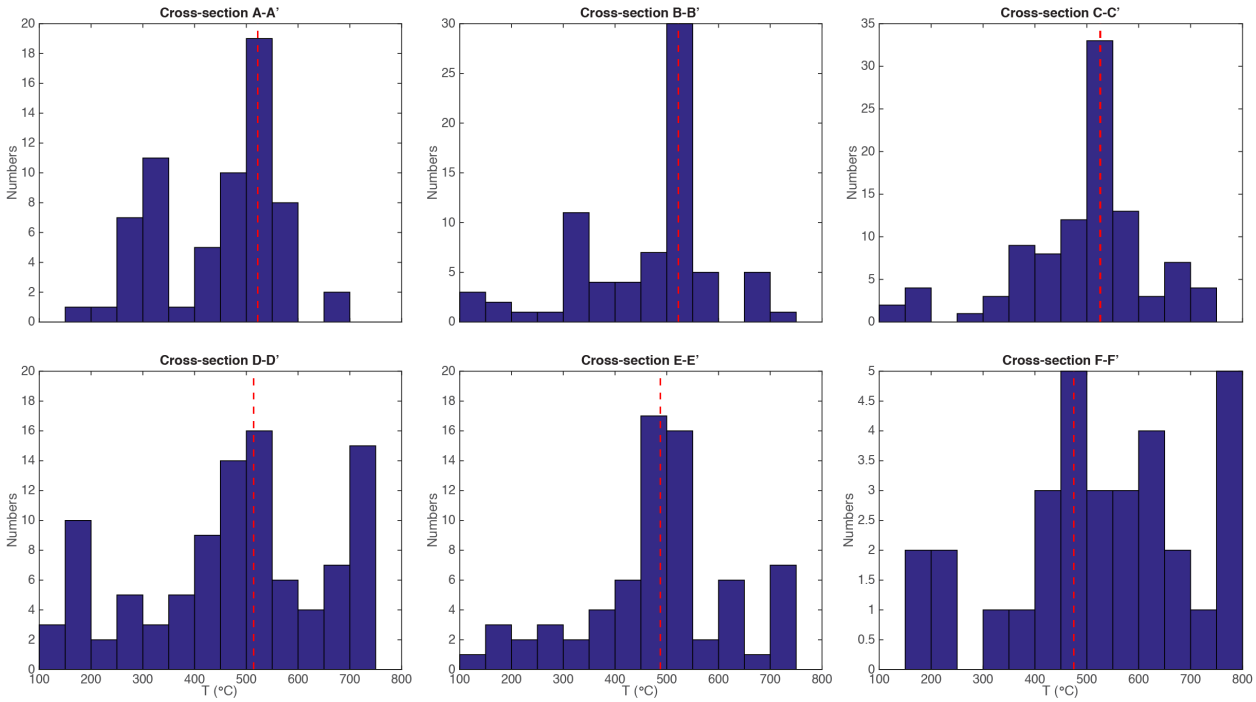

Figure 5.10. Distribution of thermal conditions of earthquakes projected to the Moho *p-T* path along each cross-section.

Red lines represent the temperature of the center of Stripe II, showing its average temperature confined in a narrow range of 475-525 ˚C.

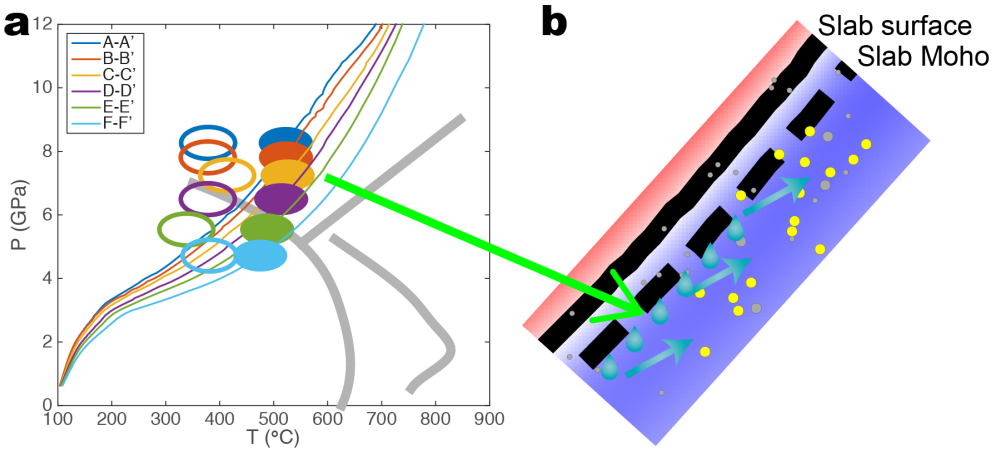

Figure 5.11. Mechanisms for the Stripe II.

(a) Modeled *p-T* paths for the earthquakes in Stripe II and the Moho along the cross-sections. Open ellipses represent the earthquake clusters identified in Figs. 5.7-5.9. Colored lines show the Moho *P-T* paths for each of the cross sections. Solid ellipses indicate these earthquakes clusters shifted to the Moho *p-T* paths. Bold gray curves show dehydration reactions as in Fig. 5.6. (b) The Stripe II zoomed in along cross-section C-C'. The events are labeled in the same manner as Fig. 5.5. The solid and dashed black curves illustrate the slab surface and Moho, respectively. The water drop symbols and arrows represent the dehydration that produces free water percolating into the slab core, and triggering extensive seismicity as the Stripe II.

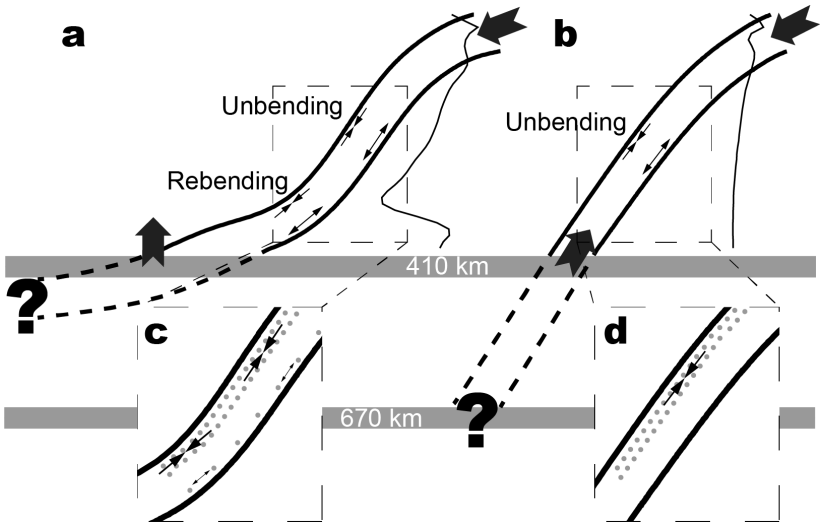

Figure 5.12. Schematic illustrations of the stress states within the Tonga slab.

(a) In northern Tonga the slab rebends upwards at greater depth due to the slab flattening in the MTZ. The slab geometry (bold curves) is adopted from the thermal model of the cross-section A-A'. (b) In central and southern Tonga the slab penetrates into the lower part of the MTZ without further bending at greater depths. The slab geometry (bold curves) is adopted from the thermal model of the cross-section F-F'. Thin curve next to the slab shows the curvature of the slab surface. Bold arrows indicate the overall stress field whereas thin arrows represent local stresses due to unbending or bending. (c) and (d) show stress status resulting from the combination of the overall stress and unbending/rebending. Gray dots represent earthquakes.

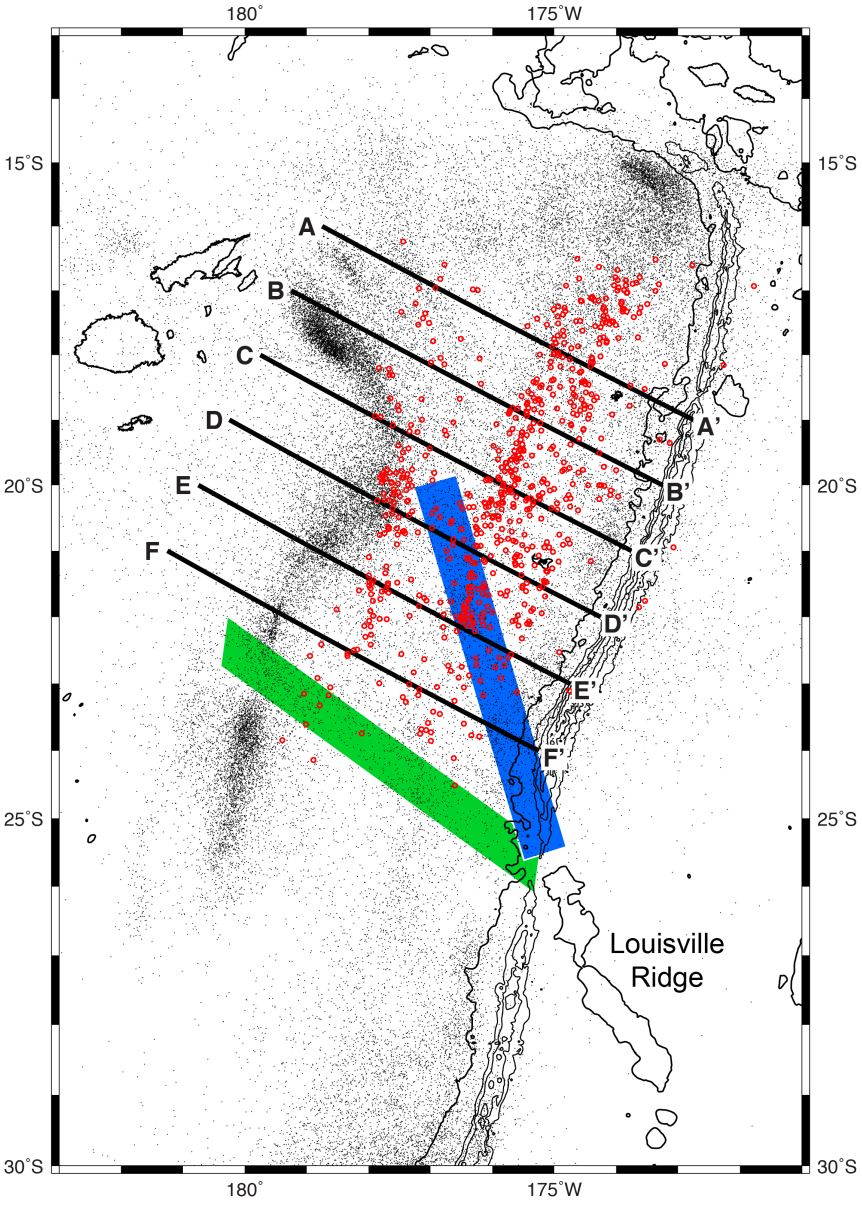

Figure 5.13. Earthquakes since 1980 from the Reviewed ISC Bulletin [*ISC*, 2013] (black dots) superposed by the events relocated in this study (red circles).

The green region represents the subducted Louisville Ridge if it was shear-deformed southwards [*Giardini and Woodhouse*, 1986], whereas the blue region illustrates the ridge without any distortion. Coastlines are contoured, and bathymetry of 4.5, 7, 8, 9, and 10 km are also contoured to delineate the Louisville Ridge and the Tonga trench.

Table 5.1. Thermodynamic parameters used in thermal modeling.

Symbol	Name	Value	Units
A	Scaling factor[a]	3.5×10^{22}	s^{-1}
n	Stress exponent[a]	3.5	
m	Grain-size exponent[a]	0	
E^*	Activation energy[a]	540	kJ/mol
V^*	Activation volume	0	cm^3/mol
μ	Shear modulus[a]	80	GPa
ρ	Density	3300	Kg/m^3
T_p	Mantle potential temperature[b]	1500	˚C
dT/dz	Mantle adiabatic gradient	0.5	˚C/km
c_p	Specific heat	1250	J/kg/K
$\varkappa_{crust}$	Thermal conductivity, crust	2.5	W/m/K
$\varkappa_{mantle}$	Thermal conductivity, mantle	3.1	W/m/K

[a] Parameters used in *Karato and Wu* [1993] dislocation creep regime for dry olivine.

[b] Based on *Wei et al.* [2015].

Table 5.2. Slab parameters for each cross-section.

(based on *Zellmer and Taylor* [2001] and *Syracuse et al.* [2010]).

Cross-section	Slab dip (˚)	V_C (km/Ma)	Age (Ma)	Sediment thickness (km)	Subducted sediment thickness (km)	Upper plate age (Ma)
A-A’	51	192.1	109	0.4	0.2	20
B-B’	54	172.6				
C-C’	54	154.5				
D-D’	48	135.3				
E-E’	52	115.2				
F-F’	54	95.9				

Table 5.3. Statistics of relocated earthquakes.

	Constrained by local arrivals	Constrained by ISC arrivals	Associated with Global CMT	Numbers
	✔	✗	✗	155
	✔	✔	✗	192
	✔	✔	✔	27
	✗	✔	✔	297
Total	**374**	**516**	**324**	**671**